CHARACTERIZING SINGLE-CELL COMPUTATION USING ALL-OPTICAL INTERROGATION OF CORTICAL DENDRITES *IN VIVO*

EVELYN WONG

NEURAL COMPUTATION LAB
WOLFSON INSTITUTE FOR BIOMEDICAL RESEARCH
UNIVERSITY COLLEGE LONDON (UCL)

A THESIS SUBMITTED FOR THE DEGREE OF
MASTER OF PHILOSOPHY (MPHIL)
JULY 2023

Declaration of Authorship

I, Evelyn Wong, confirm that the work presented in this thesis is my own. Where information has been derived from other sources, I confirm that this has been indicated in the thesis.

Evelyn Wong

01 July 2023

Abstract

Pyramidal neurons in the mouse neocortex develop elaborate dendritic compartments that integrate signals to generate stimulus-specific responses. Parameters such as the origin, strength, and location of inputs on the dendritic arbor define computations performed by dendrites to modulate neuronal activity. Although the role of dendrites in synaptic integration has been studied in brain slices *in vitro*, little is known about how their integrative properties functionally relate to dendritic computations *in vivo*. The small size of dendrites and mechanical instability of the brain have precluded the use of direct methods such as *in vivo* patch clamp recording for making functional measurements of dendritic activity during behavior. In this thesis, I have optimized existing optical methods to selectively target and monitor responses in single dendrites in the mouse neocortex, providing a proof-of-principle for all-optical interrogation of dendritic computation. I used an ultra-sparse expression strategy to express the powerful channelrhodopsin ChRmine and the highly sensitive calcium indicator GCaMP8s in Layer 2/3 pyramidal neurons in primary visual cortex (V1) for simultaneous optical stimulation and recording of basal dendrites. Previously, our lab developed a protocol for all-optical interrogation experiments (Russell et al. 2022), using a spatial light modulator (SLM) to activate cellular targets in an awake, head-fixed mouse. We re-configured this approach to optically stimulate single dendritic segments, or combinations of dendritic segments from different dendrites of the same neuron. Challenges included optimizing the relative expression of ChRmine and GCaMP8s in the soma and dendrites to both allow efficient activation and avoid overexpression, as well as calibration of the SLM to reliably target single dendrites (~1-2 µm diameter) while accounting for movement caused by respiration or running. Two-photon imaging of GCaMP8s responses revealed intensity-dependent calcium signals in dendrites with increasing laser power and number of targets. Analysis of somatic activation driven by dendritic optogenetic stimulation revealed supra- or sub-linear summation of multiple dendritic targets depending on the spatial pattern of stimulation. Applying this technique to probe dendritic integration during sensory stimulus processing or animal behavior could provide us with one of the tools needed to understand the role of single-neuron processing in neural computations in the brain.

Impact Statement

How neurons compute — how they process, transmit, or suppress information they receive from other cells — is a fundamental question in neuroscience. Despite decades of progress in characterizing signal integration using computational models and electrophysiological techniques *in vitro*, our understanding of the link between dendritic computation and behavior remains incomplete. The availability of tools to probe neuronal processing at finer scales gates our ability to investigate brain function and develop therapeutic strategies for neurological and psychiatric disorders. With current state-of-the-art optical and electrophysiological techniques, it is extremely difficult to causally manipulate neural activity with subcellular precision in awake, behaving animals — an important task in establishing how the activity of dendrites contributes to functional connectivity in the mammalian brain. This thesis aims to expand the range of capabilities offered by the existing "all-optical" toolbox (i.e., light-based techniques used to stimulate and record neural activity) by allowing us to noninvasively record and manipulate neuronal networks at the dendritic level in awake mice.

Further development of this tool would enable far-reaching applications in basic neuroscience research and neurotechnology. Within and beyond academia, this tool would confer scientists the ability to probe both healthy and diseased brain states to understand how dendritic integration is impacted during neuropsychiatric disorders. Many medications for diseases such as depression and anxiety act at the synaptic level by enhancing the effect or hindering the reuptake of neurotransmitters. Therefore, the need to ensure that current and future pharmacological agents maximize therapeutic function and minimize harmful long-term effects warrants a mechanistic understanding of how synapses — and, by extension, dendrites — synergize with neural circuits to drive brain function. Moreover, being able to causally interrupt single-cell computations *in vivo* would facilitate experiments that investigate how signal integration is altered during various behavioral states, such as attention or learning. For example, cortical feedback from higher- to primary areas is thought to guide cognition and behavior and theorized to be modulated by attention or goal direction. By directly disrupting these feedback circuits at the subcellular level or by altering the input-output functions of cortical dendrites, future experiments could consolidate a better framework for understanding how dendritic arbors modulate higher-order feedback and contribute to functional networks *in vivo.*

Lastly, translational applications of “dendritic optogenetics” range from biologically inspired artificial intelligence and machine learning models (Boahen, 2022) to next-generation read/write neural interfaces. These advancements would be driven by more precise knowledge of how motor and cognitive functions may be guided by information processing at the dendritic level. Existing neural prosthetics such as brain-computer interfaces (BCIs) function by reading the activity of entire neural populations — thus requiring the simplification of single neurons or entire circuits as “point neurons.” Future interfaces that require the ability to manipulate higher-order or subcortical networks may require more nuanced strategies for neuromodulation, which would benefit from similar tools involving the optical interrogation of dendritic arbors.

Table of Contents

List of Abbreviations

1P	Single-photon (imaging/photostimulation)
2P	Two-photon (imaging/photostimulation)
AAV	Adeno-associated virus
AP	Action potential
ANOVA	Analysis of variance
BAC	Backpropagating action potential activated Ca^{2+} spike firing
bAP	Backpropagating action potential
BCI	Brain-computer interface
ChR2	Channelrhodopsin 2
D1-D3	Dendritic targets 1, 2, and/or 3
DOI	Dendrite of interest
ETL	Electrically tunable lens
EPSP	Excitatory post-synaptic potential
FOV	Field of view
GECI	Genetically-encoded calcium indicator
GEPI	Genetically-encoded pH indicator
GETI	Genetically-encoded transmitter indicator
GEVI	Genetically-encoded voltage indicator
GUI	Graphical user interface
IVE	*In vivo* external
L2/3	Cortical Layer 2/3
NMDA	*N*-methyl-D-aspartate
ROI	Region of interest
SEM	Standard error of the mean
SLM	Spatial light modulator
SNR	Signal-to-noise ratio
V1	Primary visual cortex

Introduction

Understanding the mechanisms underlying neural computation is a fundamental pursuit within the field of neuroscience. Over the past century, progress toward this goal has relied on improved technologies for measuring, mapping, and perturbing the electrical activities of neurons within functioning brains (Marblestone et al., 2013; Stevenson & Kording, 2011). Many seminal discoveries shaping our knowledge of neural function have relied on direct electrophysiological measurements of neuron excitability (Hodgkin & Huxley, 1939; Hubel & Wiesel, 1959; Schuetze, 1983), including recordings of dendritic membrane potential via patch-clamp techniques (Davie et al., 2006; Larkum et al., 1999; Stuart & Häusser, 2001; Stuart & Sakmann, 1994). In recent decades, recording and stimulation techniques have become increasingly high-throughput, precise, and non-invasive—both doubling the number of recorded neurons every 7 years since the 1950s (Stevenson & Kording, 2011) and facilitating the observation or perturbation of single neurons to whole populations with sub-millisecond precision and minimal brain damage (Chen et al., 2021; Norman et al., 2021; Whalley, 2020). A key advancement to this end has been the detection of activity-dependent optical signals by endowing neurons with fluorescent indicators (Grienberger & Konnerth, 2012) and parallel light-dependent techniques for spatiotemporally precise control of cellular signaling (Boyden et al., 2005; Deisseroth, 2015)—issuing in a new generation of "all-optical" strategies for causally probing neural activity. In this section, I introduce significant methodological advances in all-optical interrogation, as well as remaining gaps in the quest to better understand neural function—especially dendritic computation—using these modalities.

The all-optical toolbox: Strategies for mapping brain activity

Optical readout of neural activity. Experimentally linking single-cell or microcircuit function to emergent properties of the brain requires precise measurements of neural activity with minimal damage to the local environment. Advances in microscopy and surgical techniques have allowed optical access to deep structures, enabling the recording of local circuits at single-cell resolution (Packer et al., 2015; Rickgauer et al., 2014). Optical methods for monitoring brain activity rely on activity-dependent light emissions from neurons, usually generated by fluorescent indicators in the presence of target molecules crucial to neuronal signaling. While the mechanism of action of fluorescent indicators depends on properties such as excitation and emission wavelengths and target, one underlying principle of action involves a change in fluorescence properties upon interacting with the target molecule (i.e., calcium ions or neurotransmitter molecules) or undergoing a specific cellular event (i.e., environmental changes in electric field or pH). The change in fluorescence is often detected by a photodetector, allowing one to monitor the activity or presence of the target molecule or process.

As the most common imaging method for monitoring neural activity *in vivo,* calcium indicators function by undergoing changes in fluorescence intensity upon binding to intracellular calcium ions ([Ca^{2+}]), which enter the cell through voltage-gated calcium channels or other receptors when an action potential is initiated (Baker et al., 1971; Chen et al., 2013; Grienberger & Konnerth, 2012; Russell, 2011). Early studies harnessed bioluminescent calcium-binding photoproteins, such as aequorin (Ashley & Ridgway, 1968; Shimomura et al., 1962), to monitor dynamics of cellular signaling. In the late 20th century, more highly sensitive and versatile calcium indicators (e.g., quin-2, fura-2, indo-1, fluo-3) were developed by combining fluorescent chromophores with highly calcium-selective chelators (Grynkiewicz et al., 1985; Tsien, 1980), prompting the first biological experiments reading out neural activity. In later developments, calcium dyes underwent a diversification in excitation spectra and increased signal-to-noise ratio, including the Oregon Green BAPTA and fluo-4 constructs (Paredes et al., 2008).

Another significant breakthrough in calcium indicator developments occurred with the advent of protein-based, genetically encoded calcium indicators (GECIs), which dramatically expanded the range of possible experiments monitoring calcium dynamics *in vivo* (Miyawaki et al., 1997). Genetically encoded calcium indicators function by undergoing conformational changes in response to calcium binding, leading to a change in fluorescence intensity or wavelength with fluctuations in calcium concentrations (Tsien, 1980). Compared to synthetic calcium dyes, GECIs offer improved targeting capabilities, allowing expression in specific cell types (Ahrens et al., 2013; Stirman et al., 2016) or subcellular compartments (Broussard et al., 2018; Mao et al., 2008; Shemesh et al., 2020) using transgenic or targeted viral expression techniques. While several GECIs have been developed for *in vivo* calcium imaging, the GCaMP family has been the most widely used and extensively enhanced through protein engineering methods

(Chen et al., 2013). Recent improvements to GCaMP have greatly increased its signal-to-noise ratio, dynamic range, and response kinetics for tracking the activity of subcellular compartments to defined populations. These developments have culminated in the GCaMP8 sensors, which enable the detection of single action potentials with ultra-fast kinetics and unmatched sensitivity (Zhang et al., 2021). To allow efficient pairing of calcium imaging with optogenetic manipulations with minimal spectral overlap, GECIs have been expressed with red-shifted opsins for simultaneous all-optical interrogation (Marshel et al., 2019; Packer et al., 2015; Rickgauer et al., 2014). Additionally, the range of excitation and emission wavelengths has expanded to allow the simultaneous recording of different neural populations in the same brain region, among other advantages such as improved scattering and absorption in tissue and reduced toxicity. For example, red GECIs such as jRCaMP1a and jRGECO1a have facilitated deep-tissue imaging and dual-color imaging with GCaMP (Dana et al., 2016) without spectral cross-talk.

However, minimally invasive optical recordings using calcium indicators come with the trade-off of temporal precision compared to electrophysiological recordings (Marblestone et al., 2013). As an indirect measurement of electrical activity in neurons, calcium imaging speeds are limited by the timescale of intracellular calcium rises and drops, which occur on the order of 1 ms and 10-100 ms, respectively (Higley & Sabatini, 2008). Current GECIs do not have sufficient sensitivity to detect subthreshold changes in membrane potential, which involve very little to no change in calcium concentration. To combat these drawbacks, genetically-encoded voltage indicators (GEVIs) have been developed as an emerging technology for directly monitoring electrical dynamics in neurons (Yang & St-Pierre, 2016). Voltage indicators consist of a fluorescent dye attached to a membrane-targeting molecule; when membrane potential changes, it alters the electric field across the dye molecule, leading to changes in its fluorescent properties such as intensity or wavelength (Chemla & Chavane, 2010). As changes in fluorescence can be directly correlated with changes in membrane potential, voltage-sensitive indicators represent a more temporally precise modality for recording neural activity in real time, enabling the detection of subthreshold membrane potential changes (Gong et al., 2015; St-Pierre et al., 2014). Recent developments in chemigenetic voltage indicators, namely Voltron2 and JEDI-2P, have vastly enhanced their ability to resolve both hyperpolarization and subthreshold depolarization while retaining photostability in brain tissue

(Abdelfattah et al., 2023; Liu et al., 2022). Nevertheless, major challenges associated with GEVI protein engineering remain. Firstly, while GECIs operate within the cytoplasmic volume of the cell, voltage indicators must be localized across the cell membrane in order to detect changes in membrane potential. As a result, their sensitivity to voltage changes (ΔF/F per mW depolarization) must compensate for the limited availability of molecules and thus low baseline fluorescence levels (Lin & Schnitzer, 2016). Another challenge is the need for fast sampling rates (> 300 Hz)—10-20 times higher than typically used for calcium imaging—and high excitation intensities to match the temporal resolution of the indicators themselves (Lin & Schnitzer, 2016). High illumination intensities required in tissue (~12 W/mm^2) for GEVI performance may induce thermal or photochemical damage in living animals (Hochbaum et al., 2014), as well as fast photobleaching of GEVI chromophores (Kralj et al., 2011). Therefore, this places an upper limit on experiment duration, making it difficult to monitor changes in synaptic plasticity or behavior—which requires neural recordings of 30 minutes or longer—without irreversibly damaging biological tissue (Huber et al., 2012; Liu et al., 2022). The need for fast sampling rates also precludes the use of two-photon (2P) microscopy, which is essential for imaging deeper layers of brain tissue due to light scattering but does not allow for kHz sampling rates (Brinks et al., 2015). Therefore, due to the distinctive advantages and drawbacks of calcium and voltage imaging, GEVIs continue to be optimized in parallel with GECIs rather than supplanting their use in biological studies.

Lastly, optical reporters have also been constructed for changes in synaptic vesicle release or neurotransmitter concentrations, providing synapse-specific information about signal transmission. Synaptic vesicle tracking has been performed using localized genetically encoded pH indicators (GEPIs), which rely on pHluorins—a molecule that exhibits increased fluorescence at higher pH and decreased fluorescence at lower pH (more acidic) conditions (Reifenrath & Boles, 2018; Sankaranarayanan et al., 2000). These pH-sensitive proteins are laced with a targeting sequence that directs them to synaptic vesicles, whose lumen have a resting pH of ~5.5 (Kavalali, 2015). During synaptic transmission, the contents of the vesicle are released into the extracellular environment, which has a pH of 7.0-7.5—thus driving fluorescence changes in the GEPI proteins (Lin & Schnitzer, 2016). A more targeted class of reporters for the specific contents of synaptic vesicles are genetically-encoded transmitter indicators (GETIs), which allow visualization of neurotransmitter activity either at the presynaptic terminal or postsynaptic cell (Liang et al., 2015). Powerful GETIs have recently been developed to monitor excitatory neurotransmitters such as serotonin (iSeroSnFR, (Unger et al., 2020)), acetylcholine (iAChSnFR, (Borden et al., 2020)), dopamine (RdLight1 (Patriarchi et al., 2020), $\mathrm{GRAB}_{\mathrm{DA}}$ (Sun et al., 2018)), and glutamate (iGluSnFR, (Marvin et al., 2013, 2018)) during neuronal signaling. Such sensors have capitalized on the high concentrations and fast kinetics of neurotransmitters (high µmol – low mmol range) in synaptic clefts (Diamond, 2005; von Gersdorff et al., 1998), enabling the powerful detection of glutamate release at single dendritic spines with 50% fluorescence rises (Marvin et al., 2018). Genetically-encoded indicators have also been developed for inhibitory transmitters such as GABA (iGABASnFR, (Marvin et al., 2019)) and glycine (GlyFS, (W. H. Zhang et al., 2018)). However, while iGABASnFR has been useful for mapping the global distribution of GABAergic transmission, it has not been validated in single-synapse settings (Marvin et al., 2019).

By enabling non-invasive and high-resolution optical monitoring of neuronal activity, fluorescent indicators have transformed our understanding of brain function *in vivo.* While each class of indicator presents its own strengths and drawbacks, advances in genetically-encoded indicator protein engineering continue to address existing limitations by improving sensitivity, specificity, and signal-to-noise ratios—as well as explore the synergies between different indicators by harnessing their complementary strengths and spectral properties.

Manipulating neural activity. In order to draw mechanistic and causal links between neural activity and brain function, the experimenter must be able to perturb or manipulate the compartment, cell, or network of the environment they are studying. The earliest examples of perturbing neural circuits involve direct electrical stimulation—from twitching the leg muscles of flayed frogs to prove "biological electricity" (Piccolino, 2006) in 1791 to direct, open-skull stimulation of dog motor cortex to contract contralateral muscles in 1870 (Hagner, 2012). As new modalities for direct brain stimulation evolved, less invasive techniques such as pharmacology and chemogenetics were developed to remotely control neural function using genetically engineered receptors that interact with small molecules (Sternson & Roth, 2014). However, while they enable sustained and precise modulation of signaling in genetically defined neurons, glia, and other cell types

(Armbruster et al., 2007; Campbell & Marchant, 2018), chemogenetic approaches suffer from low temporal precision, including irreversibility of effects and long onset and decay times (Vlasov et al., 2018).

Optogenetics has revolutionized the field of neuroscience by allowing spatiotemporally precise control of neural activity *in vivo* (Häusser, 2021; Scanziani & Häusser, 2009). It involves the use of opsins, which are genetically encoded light-sensitive proteins that respond to specific wavelengths of light by allowing the passage of ions across the cell membrane (Boyden et al., 2005). Excitatory opsins such as Channelrhodopsin2 (ChR2) have been used to depolarize neurons by allowing Na^+ ions to enter the cell (Boyden et al., 2005), while inhibitory opsins such as halorhodopsin or Jaws cause Cl^- ions to be pumped into the cell, inducing hyperpolarization (Chuong et al., 2014; F. Zhang et al., 2007). Similar to chemogenetic actuators, opsins can be expressed selectively in defined cell types through driver lines or transgenic animals, allowing experimenters to interrogate the function of specific populations within neuronal networks *in vivo* (Sridharan et al., 2022; Zeng & Madisen, 2012).

Optogenetic activation of neurons was first demonstrated using blue light to depolarize cultured hippocampal neurons expressing Channelrhodopsin-2 (ChR2), allowing action potentials to be triggered with millisecond precision (Boyden et al., 2005). (In the same year, photoactivation of optically-gated ion channels was also demonstrated using genetically-encoded “phototriggers” of action potentials in *Drosophila* (Lima & Miesenböck, 2005)). Later studies led to the development of red-shifted excitatory opsins such as the C1V1 family (Packer et al., 2012, 2015; Prakash et al., 2012; Rickgauer et al., 2014), including opsins with heightened light-sensitivity, larger photocurrents, and greater temporal fidelity—such as Chronos (Ronzitti et al., 2017) and ChRmine (Marshel et al., 2019). Most studies have employed red-shifted opsins in parallel with green calcium indicators (i.e. GCaMP) to minimize spectral cross-talk and thus avoid unintentional excitation of the opsin by the imaging laser (Russell et al., 2022). The most potent advances in ChRmine have even facilitated transcranial photoactivation of defined neural circuits at up to 7-mm brain depths (Chen et al., 2021), as well as millisecond-level activation of cardiomyocytes through intact skin (Hsueh et al., 2023). However, a number of groups have also continued to optimize red indicators (i.e. jRCaMP (Forli et al., 2018), jRGECO (Dana et al., 2016), or XCaMP (Inoue et al., 2019)) with blue-light sensitive opsins such as ChR2 or ChroME (Mardinly et al., 2018), which benefit from minimal spectral overlap in deeper brain regions (Russell et al., 2022).

Inactivation of neurons via inhibitory opsins has also been achieved, most notably through the light-gated chloride pump, halorhodopsin (NpHR) (Matsuno-Yagi & Mukohata, 1977) — which has been optimized for robust expression at neuronal membranes and sensitivity to a broad wavelength range (520-620 nm) (Gradinaru et al., 2010). Optical inhibition has also been accomplished through the development of outward proton pumps, including Arch (Chow et al., 2010). Currently, however, only eArch3.0 has been successfully recruited by two-photon illumination to block action potentials *in vitro* (Gradinaru et al., 2010; Prakash et al., 2012). The use of eArch3.0 has not been reliably demonstrated *in vivo,* however, due to its large spectral overlap GCaMP (Mattis et al., 2011). To overcome this limitation, red-shifted inhibitory actuators have been developed to further separate the activation spectra of indicator and opsin. These include eNpHR3.0 (Gradinaru et al., 2010) and Jaws (Chuong et al., 2014), the latter of which has enabled robust inhibition of sensory-evoked neural activity in mouse cortex, including efficient transcranial inhibition in motor, somatosensory, insular and piriform cortices (Chuong et al., 2014).

Simultaneous readout (“read”) and manipulation (“write”). In conjunction with evolving optogenetic actuators, novel methods for targeted photostimulation approaches have also been developed in a move toward single-cell optogenetics *in vivo* (Papaioannou & Medini, 2022). Early experiments demonstrating the possibility of optogenetic control of neural activity relied on single-photon, wide-field activation (Boyden et al., 2005; F. Zhang et al., 2007) — which lacks cellular resolution. Recent developments have not only demonstrated the potential for multiphoton strategies to target individual neurons *in vivo* (Rickgauer et al., 2014; Rickgauer & Tank, 2009), but also have paved the way for simultaneous, targeted photostimulation of multiple neurons in 3D (Packer et al., 2015). Furthermore, parallel advances in imaging technologies have enabled simultaneous photostimulation (manipulation) and readout of user-defined neural circuits with single-cell resolution (Adesnik & Abdeladim, 2021; Emiliani et al., 2015). This “all-optical” interrogation strategy involves the co-expression of calcium indicators (i.e., GCaMP) with spectrally shifted opsin (i.e., C1V1 or ChRmine) to allow read-write capabilities with minimal optical cross-talk (Packer et al., 2015; Rickgauer et al., 2014; Sridharan et al., 2022). To stimulate arbitrary clusters of genetically or functionally defined neurons, patterned illumination strategies using spatial light modulators (SLMs) have been used to alter beam wavefronts and spatially redistribute focused beamlets to target neurons in 3D (Packer et al., 2013; Russell et al., 2022). In comparison to parallel illumination of target regions within the brain, serial scanning methods have been shown to require smaller excitation volumes and 20 times less power (Peron & Svoboda, 2011; Yang et al., 2018), albeit at the cost of temporal precision due to longer scanning times (Russell et al., 2022).

Over the past decade, researchers have extensively relied on both single-cell and holographic photostimulation methods to manipulate cortical circuits while simultaneously recording their responses *in vivo* (Carrillo-Reid et al., 2016; Chettih & Harvey, 2019; Papagiakoumou et al., 2018; Ronzitti et al., 2017; Russell et al., 2019). Despite the immense utility of the all-optical toolkit, few studies have explored the potential for *in vivo* optogenetic control of subcellular compartments, specifically dendrites. Existing research has predominantly focused on somatic stimulation or synaptic manipulation, often overlooking the critical role that dendritic integration plays in informational processing. In the next section, I will discuss major recent advances related to dendritic physiology and interrogation, as well as the potential for all-optical interrogation strategies to uncover critical links between dendritic computation and behavior.

Dendritic Physiology: Insights into Neural Computation

Principles of cortical dendrite function. As the primary site of signal transfer in the mammalian central nervous system, dendrites play a central role in cortical computation (Grienberger et al., 2015). In the mammalian neocortex, dendrites form intricate branching processes that make up most of the surface area of pyramidal cells, receiving both excitatory and inhibitory inputs from presynaptic neurons (Iascone et al., 2020). The complex dendritic architecture of pyramidal neurons, along with input patterning and active integration, determines the transformation of synaptic inputs into output action potentials (APs) (Major et al., 2013).

One emblematic feature of pyramidal neurons is dendritic spines—small, protruding structures along dendrites that serve as the sites of excitatory input transfer. Dendritic spines are crucial to the processing and integration of inputs, as they provide a local, compartmentalized environment for synaptic transmission (Spruston, 2008). While the morphology of dendritic spines is highly diverse across neuronal populations and brain regions, one common role shared across dendrites is their dynamic role in synaptic plasticity. Excitatory synapses exhibit both structural (Holler et al., 2021) and Hebbian (strengthening or weakening of synaptic weights) plasticity depending on experience, playing a critical role in memory encoding and retention (Häusser et al., 2000; Holtmaat et al., 2005; Yang et al., 2009). Synapse-specific plasticity has also been demonstrated in basal dendrites of Layer 2/3 pyramidal neurons, mediated by their role as Ca^{2+} compartments within spines (Nevian & Sakmann, 2006). On the other hand, inhibitory GABAergic inputs to dendrites are mostly made onto dendritic shafts, though some also target spines (Somogyi et al., 1981). The highly compartmentalized nature of dendritic arbors within pyramidal neurons enables different subcortical layers to be differently regulated by inhibition (Bloss et al., 2016; Fishell & Rudy, 2011).

Dendritic compartments receiving input from different presynaptic populations also drive distinct synaptic plasticity and integration rules across cortical maturation. In the hippocampus and neocortex, pyramidal neurons share a stereotypical morphology characterized by subdivided basal (proximal) and apical (distal) dendritic trees. Thin basal dendrites generally branch from the base of the cell body and receive the majority of inputs from local pyramidal neurons and interneurons (Larkman, 1991). Moreover, basal dendrites support the initiation of NMDA spikes, which are associated with large local calcium influx (Schiller et al., 2000) and can trigger long-term synaptic plasticity (Sjöström & Nelson, 2002). Apical tufts, on the other hand, branch off from a single apical dendrite emerging from the apex of the pyramidal soma; they are most distal along the ascending trunk, residing in Layer 1. Due to their ability to span distinct cortical layers, apical and basal dendrites are targeted by axons originating in different cortical regions, and thus act as separate functional dendritic compartments (Larkum et al., 1999; Yuste & Denk, 1995). In contrast to basal dendrites, which receive feedforward sensory inputs from nearby neurons or subcortical structures like the primary thalamic nuclei (Larkum, 2013), apical dendrites receive primarily feedback signals from higher cortical areas, associative areas, and motor regions (Gillon et al., 2023). In addition to their different input types, anatomical and physiological differences between apical and basal dendrites may allow them to serve distinct

— yet complementary — computational roles in learning and inference (Guerguiev et al., 2017; Payeur et al., 2021; Sacramento et al., 2018).

Studies of* in vitro *dendritic computation. Previously regarded to play a passive role in information transfer between neurons, increasing evidence has shown that dendrites contribute heavily to the active integration of synaptic inputs—and therefore single-cell computation (Major et al., 2013). Key findings have leveraged a combination of electrophysiological recordings and calcium imaging to elucidate major aspects of dendritic computation, specifically their ability to perform nonlinear integration of synaptic signals (Branco & Häusser, 2010; Major et al., 2013; Poirazi et al., 2003; Polsky et al., 2004). This capability for nonlinear processing is due in part to the mechanism underlying synaptic activation: inputs to a dendritic spine alter the membrane conductance to other ions—driving parallel activation due to multiple colocalized inputs and thus nonlinear summation (London & Häusser, 2005). One of the earliest pioneers in dissecting dendritic processing, Wilfrid Rall, first introduced computational models to predict the nature of nonlinear synaptic integration, hypothesizing that the spatial direction of input sequences influences their overall summation (Rall, 1964). This theory was later experimentally validated using optical recordings in conjunction with sensory stimulation in retinal dendrites (Euler et al., 2002) and with two-photon glutamate uncaging in cortical pyramidal neurons (Branco et al., 2010) — showing that dendrites are sensitive to both direction and velocity of synaptic inputs, and thus can distinguish spatiotemporal input sequences.

The presence of active conductances within dendritic subunits also gives rise to their unique ability to shape neuronal output and plasticity. The law of dynamic polarization, originally formulated by Santiago Ramon y Cajal (1911), postulates that information flow is unidirectional from dendrites to soma and axon of neurons. However, it has been shown that the reverse is also possible: previous studies have found that action potentials in the soma can propagate back toward the dendritic tree (Stuart & Sakmann, 1994). These signals—termed “backpropagation” or “backpropagating action potentials (bAPs)” — serve as a mechanism for feedback within the neuron and play an integral role in triggering synaptic plasticity (London & Häusser, 2005; Magee & Johnston, 1997; Sjöström & Häusser, 2006). In pyramidal neurons, single bAPs (when paired with strong distal synaptic input) are sufficient to activate dendritic voltage-gated ion channels, lowering the threshold for triggering dendritic spikes that in turn flow back toward the axon initiation zone to generate additional action potentials (Larkum et al., 1999; Williams & Stuart, 2000b).

Subsequent experiments conducted in brain slices have further illuminated the electrogenic capabilities of dendrites. *In vitro* electrophysiological recordings and computational modeling studies have found three major types of dendritic spikes, including Na^+, Ca^{2+}, and *N*-methyl-D-aspartate (NMDA) spikes (Ariav et al., 2003; Häusser et al., 2000; London & Häusser, 2005; Polsky et al., 2004; Schiller et al., 1997). Due to their differences in electrical properties, channel types, and densities, these spikes exhibit major differences in rise times and duration during regenerative events (Amitai et al., 1993; Major et al., 2013; Wong et al., 1979). Computational models relating dendritic morphology and voltage-gated channel distributions have compared the features of somatodendritic coupling to a two-layer neural network (Poirazi et al., 2003), which has been experimentally validated in Layer 5 pyramidal neurons (Polsky et al., 2004). This coupling has also been observed via calcium imaging in the soma and apical dendrites of Layer 5 pyramidal neurons of mouse visual cortex, indicating the highly correlated activity between different tuft branches when the soma is simultaneously active (Beaulieu-Laroche et al., 2018; Francioni et al., 2019). Functionally, the interaction between somatic activity and dendritic spiking within pyramidal neurons may enable complex integrative computations such as sensory feature selectivity (Goetz et al., 2021; Lavzin et al., 2012; Oswald et al., 2004; Smith et al., 2013), sensory perception (Manita et al., 2015; Takahashi et al., 2016; Xu et al., 2012), learning and memory (Doron et al., 2020; Schoenfeld et al., 2021).

Regenerative mechanisms in dendrites also enable them to serve as coincidence detectors at both local (spine) and global (neuron) levels. At the local level, synaptic inputs arriving synchronously at the same dendritic branch in Layer 5 neurons generate a positive feedback loop mediated by NMDA spikes (Polsky et al., 2004; Schiller et al., 2000); in hippocampal CA1 pyramidal neurons, a similar mechanism for local coincidence detection occurs through Na^+ currents (Ariav et al., 2003). Another mechanism for global coincidence detection occurs through the activity of Ca^{2+} currents, which have been observed in brain slices (Schiller et al., 1997) and via calcium imaging *in vivo* (Svoboda et al., 1999). Dendritic calcium spikes, which follow local NMDA or Na^+ spikes and occur in the distal apical tuft (Schiller et al., 1997), are largely facilitated by backpropagating action potentials from the soma (Larkum et al., 1999). By “detecting” co-activation of inputs to apical and basal compartments of pyramidal neurons, these recruited calcium spikes—also termed “backpropagating action potential activated Ca^{2+} spike firing” (BAC)—serve as a fundamental associative mechanism within single cells (Larkum, 2013; Larkum et al., 1999).

***Studying dendritic function* in vivo.** While pioneering studies delineating properties of dendritic computation have been conducted in brain slices, the functional role of dendritic activity and perception or behavior can only be validated within intact and functioning brains. Doing so using electrophysiological manipulations (i.e., direct current injection into *in vivo* dendrites) is extremely difficult due to several factors: **(1)** the small size of dendrites, **(2)** the mechanical instability of the brain due to respiration, heartbeat, or animal behavior, and **(3)** the relatively invasive nature of patch-clamp techniques precludes their reliable implementation in linking dendritic activity to behavior. In recent decades, studies mapping dendritic spine activity and function have shifted from *in vitro* electrophysiology to *in vivo* methods, including two-photon calcium and voltage imaging. Initial studies focused on mapping sensory-evoked dendritic Ca^{2+} in visual (Jia et al., 2010, 2011), auditory (Chen et al., 2011), and barrel cortex (Varga et al., 2011). These studies paired dendritic calcium imaging with whole-cell electrophysiological recordings to hyperpolarize recorded neurons, effectively blocking APs to allow accurate sensory mapping of sensory inputs. While studies in the visual cortex have found that the tuning of Layer 2/3 pyramidal neurons could be predicted by averaging the responsivity of their individual spines (Jia et al., 2010), studies conducted in other sensory cortices have found a more heterogeneous distribution of synaptic inputs without any discernible patterns of functional clustering on individual dendrites (Chen et al., 2011; Varga et al., 2011).

Further experimental studies have not only confirmed the presence of nonlinear dendritic integration discovered *in vitro,* but have indicated that dendritic processing *in vivo* is more complex than originally predicted (Grienberger et al., 2015). Studies in intact, functioning brains enable the functional mapping of dendritic integration in the context of wider neuronal networks. For example, synaptic amplification in dendrites of Layer 4 spiny stellate neurons of barrel cortex have been shown to generate NMDA spikes, which in turn contribute to the neurons’ angular tuning (Lavzin et al., 2012). This finding indicated the ability of a single neuron to perform both linear and supralinear summation of thalamocortical and corticocortical inputs based on the nature of informational inputs. Moreover, combined somatic electrophysiological recordings and two-photon calcium imaging in anesthetized animals have dissected the contribution of dendritic non-linearities on neuronal output *in vivo* (Grienberger et al., 2014; Hill et al., 2013).

A substantial number of studies have recorded active dendritic properties or mapped synaptic input *in vivo;* however, few studies have directly interrogated dendritic computation *in vivo,* either through dendritic perturbation or in behavioral, non-anesthetized contexts. To directly probe the role of local NMDA conductances in sensory processing, for example, Palmer et al. (2014) harnessed two-photon uncaging of an intracellular NMDA receptor antagonist (tc-MK801) in tuft dendrites of Layer 2/3 pyramidal neurons. Their study demonstrated that sensory stimulation significantly increases NMDA spike probability, which in turn enhances neuronal output. Direct patch-clamp recordings have also been performed in pyramidal neuron dendrites of lightly anesthetized and awake mice, showing that sodium spikes originating in distal dendritic tufts enhance orientation selectivity in visual cortex (Smith et al., 2013). One method for optical *in vivo* dendritic interrogation, recently pioneered by Fişek, Herrmann et al., utilizes long-range all-optical connectivity mapping and sensory stimuli to drive local dendritic calcium signals (2023). This method enables the investigation of cortico-cortical (circuit-level) feedback mechanisms by innervating Layer 1 dendrites through the activation of presynaptic neurons residing in higher cortical areas. Another recent study by Wong-Campos et al. utilized patterned channelrhodopsin activation with dual-plane voltage imaging to simultaneously manipulate and record dendritic signal processing *in vivo.* Probing the voltage dynamics between soma and dendrites, this study found that backpropagation into distal dendrites was influenced by spike rate acceleration at the soma—suggesting that dendritic filtering of bAPs may contribute to activity-dependent plasticity (Wong-Campos et al., 2023).

In a landmark paper linking active dendritic properties to neuronal processing in awake, behaving organisms, local calcium spikes were found to encode the threshold of perception (Takahashi et al., 2016). Furthering the goal of recording from dendrites in a behavioral context, Moore et al. developed a unique method to record subthreshold potentials in distal dendrites of freely behaving rats for up to four days (Moore et al., 2017). This chronic quasi-intracellular recording used tetrodes to elicit an immune response by glial cells, trapping dendrites between tetrode tips before glial encapsulation occurred and enabling direct observations into dendritic electrical activity. However, this method yielded a low success rate, highlighting the need for more reliable methods to investigate how dendrites transform input signals into output responses *in vivo.*

Due to their relative ease of access to cortical circuits and minimal invasiveness compared to electrophysiological recordings, all-optical methods have been increasingly used to draw insights into the link between cortical activity and behavior (Emiliani et al., 2015). In this thesis, I describe an adaptation of these optical technologies to directly stimulate and record basal dendrites of Layer 2/3 pyramidal neurons in the awake, head-fixed mouse. By adapting an existing all-optical toolbox to study *in vivo* dendritic activation in primary visual cortex, we aim to provide a platform for future studies to probe dendritic information processing in conjunction with behavior.

Materials and Methods

Animals and virus injections

All experimental procedures were carried out under license from the UK Home Office in accordance with the UK Animals (Scientific Procedures) Act of 1986. Male and female *C57BL/6* mice (*Mus musculus*) approximately aged seven to nine weeks were used without randomization. Two to four hours before surgery, mice were injected with dexamethasone (Dexadreson, 5 mg per kg body weight at 2 mg/mL) (Goldey et al., 2014). Five minutes before incision, mice were given a subcutaneous injection of buprenorphine hydrochloride (Vetergesic, 1 mg per kg body weight at 0.3 mg/mL) and 0.5% lidocaine hydrochloride (Hameln Pharma, 6 mg per kg body weight) beneath the planned incision line in the scalp. Mice were shaved and anesthetized with isoflurane (5% induction, <1.5% maintenance). To prevent drying of the cornea during operation, 5% dexpanthenol (Bepanthen) was applied to the surfaces of both eyes. The scalp was removed, and the skull was cleaned with *in vivo* external (IVE) buffer solution (20 mM Tris, 140 mM NaCl, 0.001% Pluronic F-68, pH 8.0), and an aluminum or titanium headplate with an 11 mm circular imaging well was fixed to the skull overlying visual cortex with dental cement (Super-Bond C&B, Sun-Medical). A 4-mm craniotomy was performed over the left primary visual cortex, and the dura was removed carefully. For viral injections, calibrated pipettes (Drummond Scientific Company, Wiretrol II, 5-000-2005) were beveled to a sharp point, with an inner diameter of about 10-15 µm. A mixture of pGP-AAV-CAG-FLEX-jGCaMP8s-WPRE (Addgene, genomic titer: 2.6 x 10^{13}), ssAAV-9/2-hEF1a-dlox-ChRmine_MTS_mScarlet_ERES(rev)-dlox-WPRE-hGHp(A) (ETH Zurich Viral Vector Facility, genomic titer: 6.4 x 10^{12}), and pENN.AAV.CamKII 0.4.Cre.SV40 - AAV1 (Addgene, genomic titer: 1 x 10^{13}) was created using the dilution factors in **Table 1.** Using a hydraulic injection system (Narishige MO-1), titrated mixtures of Cre, GCaMP, and opsin were injected into layer 2/3 (~200-300 µm deep) at 6-8 sites spaced about 300 µm apart, at a rate of 100 nL per minute. Injection sites were guided by blood vessel patterns to minimize bleeding. A 5 min dwell time followed each injection to allow the virus to settle before retracting the pipette. For chronic imaging, cranial "windows" were constructed by using a single 4 mm glass coverslip with small pieces of coverslip optically glued to the top side to provide additional support for the dental cement. After injections, the window was placed above the cortex and a small amount of cyanoacrylate glue (Vetbond, 3M) was used to seal the craniotomies. Windows and head plates were fixed in place with dental cement. Postoperative analgesic treatment was administered for 3 days while the mice recovered. Imaging experiments were performed 2-3 weeks after surgery to allow for viral expression.

Table 1. Calcium activity indicators and red-shifted opsin dilutions. *Cre virus, Cre-dependent calcium activity indicator, and opsin used in expression optimization experiments and their dilutions with sterile buffer. Bolded dilution levels indicate final working titers for experiments.*

Cre	Imaging		Photostimulation	
Virus & Dilution	**Indicator**	**Dilution**	**Opsin**	**Dilution**
pENN.AAV.CamKII 0.4.Cre.SV40 - AAV1 (1x10^{13} vg/mL): 1:10, 1:1000, 1:50k, 1:80k, **1:90k,** 1:100k	pGP-AAV-CAG-FLEX-jGCaMP8s-WPRE (2.6x10^{13} GC/mL)	1:10, **1:15,** 1:20, 1:30	ssAAV-9/2-hEF1a-dlox-ChRmine-MTS-mScarlet-ERES(rev)-dlox-WPRE-hGHp(A) (6.4 x 10^{12} vg/mL)	1:1, 1:2, 1:10, 1:15, 1:20, 1:30, **1:35,** 1:40

Two-photon imaging

Ultrasparse expression of *Cre,* calcium indicator (GCaMP8s), and opsin (ChRmine) was achieved by the following mixture: pENN.AAV.CamKII 0.4.Cre.SV40 - AAV1 (Addgene) diluted 1:90,000 from a stock concentration of 1 x 10^{13} genome copies (g.c.) per mL, pGP-AAV-CAG-FLEX-jGCaMP8s-WPRE (Addgene) diluted 1:15 from a stock concentration of 2.6 x 10^{13} g.c. per mL, and ssAAV-9/2-hEF1a-dlox-ChRmine_MTS_mScarlet_ERES(rev)-dlox-WPRE-hGHp(A) (ETH Zurich Viral Vector Facility), diluted 1:35 from a stock concentration of 6.4 x 10^{12} g.c. per mL. Two-photon imaging was performed with a resonant scanning microscope (Ultima 2P plus, Bruker) bearing a tunable laser (InSight X3, Spectra-Physics) driven by PrairieView. A 16x/0.8 NA objective (Nikon) was used for all experiments. GCaMP8s was imaged at an excitation wavelength of 920 nm, and mScarlet (conjugated to the ChRmine opsin) was imaged at 765 nm. Full z-stacks of GCaMP and opsin expression were obtained for each neuron before each experiment. To obtain volumetric stacks, the imaging path was coupled with an electrically tunable lens (ETL, Optotune) to allow high-speed volumetric imaging, spanning a 200 μm z-range with 2 μm spacing between planes. Images (512 x 512 pixels, 192 x 192 μm FOV for 10x zoom, 385x385 μm FOV for 5x zoom) were acquired at 30 Hz at a single plane. An orbital nose piece was used to maximize imaging quality by manually identifying the tilt of the sample relative to the microscope and rotating the objective to be perpendicular to the imaging window.

Two-photon optogenetics

Simultaneous two-photon optogenetic excitation was achieved using 1,030 nm light delivered from a fixed wavelength fiber laser (Satsuma HP2, Amplitude Systems) at a 1 MHz repetition rate. Concentrations of opsin were diluted as described previously (see **Two-photon imaging**). The laser beam was split using a programmable reflective spatial light modulator (SLM) (OverDrive Plus SLM, Meadowlark Optics/Boulder Nonlinear Systems) installed in line with the photostimulation path (Carrillo-Reid et al., 2016; Packer et al., 2015). This SLM contained 512 x 512 pixels and spanned a 7.68 x 7.68 mm active area. To program the SLM to target selected dendrites, phase masks were computed using the weighted Gerchberg-Saxton algorithm and loaded using Blink (Meadowlark) software to generate focused beamlet patterns in the sample. The targets were weighted according to their location relative to the SLM's FOV center to compensate for the decrease in diffraction efficiency when aiming beamlets at peripheral targets. For experiments involving randomized stimulation of a single dendritic branch per trial, the uncaging galvanometers were used to generate 20 µm spirals centered at the dendritic target. For experiments involving simultaneous targeting of multiple dendritic branches, the SLM was used after calibrating power delivered per target at 5x zoom (385 x 385 µm FOV). Calibrations were performed using custom software written in MATLAB (Russell et al., 2019) (https://github.com/llerussell/SLMTransformMaker3D) and adapted for dendritic photostimulation. During calibration, arbitrary patterns were generated and burnt into a fluorescent slide by the photostimulation laser. Burnt spots were manually located and the corresponding affine transform from SLM space to imaging space was computed. For multi-target experiments, to maximize stimulation efficiency, the center of the SLM space was offset by moving the galvanometers close to the centroid of the stimulation targets for each trial. Stimulation patterns consisted of multiple beamlets targeting between 1 and 3 dendrites. Spiral photostimulation patterns (5 revolutions, 20 µm diameter, 10 ms spiral scans at 20 Hz) were generated by moving all beamlets simultaneously with a pair of galvanometer mirrors conjugate to the SLM plane (Carrillo-Reid et al., 2016; Packer et al., 2015; Zhang et al., 2018). Power on the sample for photostimulation was kept between 1-40 mW per target and evenly distributed across beamlets generated by the SLM. Stimulation targets were selected by identifying neurons that were both GCaMP-and ChRmine-positive and with healthy viral expression (fluctuating GCaMP signal, no overexpression or unhealthy saturation). Of the 18 mice injected with the final titer, 3 mice were used for recordings, 2 of which are included in this thesis.

Online target selection

A graphical user interface (GUI, ROISelect) was created using MATLAB to load z-stacks taken using 2-photon imaging, allow user-selected targets, and interface with the SLM to perform two-photon optogenetic stimulation (see **Fig. 1d**). Volumetric stacks were loaded onto the GUI, and dendritic targets were identified by manually drawing regions of interest (ROI). The centroid of each ROI was computed and loaded into a phase mask generator and used for SLM-driven targeting of individual dendrites.

Single- and multi-target experiments

Before each experiment, a z-stack and expression recordings (810 nm, GCaMP; 765 nm, ChRmine-mScarlet) were taken for each neuron. Using the ROISelect tool, individual dendritic branches were identified for selection based on the following criteria: a) healthy expression of GCaMP, b) visible ChRmine expression at 765 nm, and c) target dendrite does not overlap with any ChRmine- or GCaMP-expressing dendrite from another cell. For each neuron, three dendrites were selected for stimulation and 3-4 dendrites, serving as “control” targets, were not stimulated over the course of the experiment. Single- and multi-target experiments were divided into blocks containing increasing sets of varying laser powers directed to each target. For single-target experiments, the blocks were as follows: Block 1: 1, 2, 4, 8, 10 mW; Block 2: 10, 14, 18, 22, 26 mW; Block 3: 24, 28, 32, 36, 40 mW. Each block contained 150 trials which randomized the dendritic target being stimulated and the power directed to the selected target. Following each 10 ms stimulation period was a 4 s post-stimulation gap allowing the target to return to baseline activity levels and the uncaging galvanometers to move to the next location. For multi-spiral experiments, the blocks included the following powers per dendritic target: Block 1: 4, 8, 12 mW; Block 2: 10, 20, 30 mW; Block 3: 12, 24, 36 mW. Each block contained 210 trials, each of which randomized the power per target as well as the combination of dendrites being stimulated simultaneously (1, 2, or 3 dendrites). For conditions in which two dendrites were simultaneously stimulated, to control for the power delivered to each target, a third “pseudo-target” was defined at the zero-order block of the SLM. Voltage signals containing two-photon imaging frame pulses, galvanometer command signals, and the SLM phase mask updates were recorded at 20 kHz with custom software (PackIO) (Watson et al., 2016), enabling precise post hoc synchronization of stimulation delivery times and individual imaging frame times.

Image pre-processing

Raw imaging data was pre-processed using Suite2P (https://github.com/cortex-lab/Suite2P). For each neuron, recordings from all blocks were all spatially registered together to allow for synchronization of ROI signal extraction. ROIs were manually selected using the ROISelect tool (see **Online target selection**), which generated masks to extract average pixel intensities for stimulated and nonstimulated dendrites. Change in fluorescence over average baseline fluorescence (ΔF/F) was calculated for each ROI using a 2 s sliding window and dividing each intensity value by the 10th percentile fluorescence (“F_0”) for each window. **Note:** Due to high variability in background fluorescence, when ΔF/F was computed with the above parameters, the baseline was generally positive. Future analyses will be informed by a sense of how the signal-to-noise ratio fluctuates across a wider dataset and an assessment of which percentiles are appropriate for computing F_0 in these populations of dendrites (See **Discussion**).

Single-trial response calculation

For all analyses, photostimulation frames were excluded to remove light artifacts. Single-trial responses were calculated by subtracting the mean ΔF/F of five frames post-stimulation from the “baseline” activity, which is the mean ΔF/F of ten frames pre-stimulation:

Norm. Mean Resp. = *(post stim mean) - baseline*

This was computed and averaged over all relevant trials to obtain the mean (trial-averaged) response for each condition.

Time-lapse activation heat maps

Heat maps of photostimulation-triggered activation for each ROI (**Fig. 4a**) were generated as follows: the baseline activity heat map was generated by averaging the 5 frames pre-stimulation, the post-stimulation heat map averaged 5 frames after stimulation occurred, and the late stimulation response map took the average of 5 frames 500 ms (15 frames) post-stimulation. Response maps were averaged over all trials and 2-D median filtered (kernel = 1.125 μm) to remove noise. To compare stimulated versus control trials (or early versus late response), the difference between the post- and pre-stimulation heat maps was computed and then divided by the baseline response (**Fig. 4b**). To obtain the distance-dependent dendritic activation heatmap (**Fig. 4c**), we computed the distance between each pixel coordinate and the photostimulation target centroid. Then, for each frame pre- and post-stimulation, we mapped the baseline-normalized intensity of each pixel value over time.

Radial distance-dependence analysis

For all distance-dependent analyses, distance from the soma was obtained by computing the Euclidean distance between the target coordinates (center of photostimulation spiral) and the centroid of the soma ROI (drawn manually). For each photostimulation target (**Fig. 6a;** red dots), the Euclidean distance (d) between the target centroid and the soma center (s, blue star) was calculated. For each target, an imaginary circle with radius *d* and center *s* was drawn (dotted line), such that the circle intersects with the stimulation point on the target dendrite and all other non-stimulated dendrites. Pairwise statistical comparisons were performed using a Wilcoxon rank sum test. We compared mean response along recorded dendrites, as well as across distance-equalized points on each stimulation radius.

Distribution matching

To isolate the effects of local activation and backpropagation in measured dendritic ROI responses (**Fig. 7**), trials where two different dendrites induced similar somatic response levels were considered. A distribution-matched trial set was generated by considering each bin of matching, non-negative somatic responses. Trials were sampled from the higher-frequency condition to obtain two datasets (one from each stimulated dendrite) with the same number of trials. From these somatic response-matched trial sets, two conditions were compared: the dendritic activation of Target 2 (D2) when Target 1 (D1) was stimulated (bAP only), and the dendritic activation when D2 itself was stimulated (bAP + local activation). A Wilcoxon rank sum test was performed, and an estimated local component and corresponding p-value were obtained. We bootstrapped the bAP + local and bAP response comparison by resampling trials with replacement, 1,000 times. The resulting distribution was used to determine mean p-values and estimate the local component of dendritic activation. We divided the mean local component value by the mean backpropagation-induced dendritic response to obtain the proportion of dendritic activation explained by local, targeted photostimulation.

Power-scaled dendritic activation analysis

To examine how somatodendritic response scales with power (**Fig. 11**), theoretical responses for doubled and tripled powers were compared to empirically measured responses. First, all traces were baseline-subtracted to center the pre-stimulation activity at zero. For each block, a “theoretical,” linear somatic response for the second and third powers was computed by doubling or tripling the activation measured in the “baseline” first power level. This theoretical response was baseline-subtracted and compared with the measured response recorded when the power was doubled or tripled *in vivo.* This analysis was then repeated for each stimulated dendrite response.

Dendritic summation analysis

To examine how simultaneous photostimulation of multiple dendritic targets summates (**Fig. 12**), theoretical responses for multi-target activation were compared to empirically measured responses. All traces were first baseline-subtracted to center pre-stimulation activity at zero. At each power and for each possible combination of dendritic targets, a “theoretical” linear somatic response for their simultaneous activation was computed by adding the respective somatic responses evoked by individual dendritic activation traces. This hypothetical linear response was then compared to the baseline-subtracted somatic response during simultaneous activation of multiple dendritic targets. This analysis was then repeated for individual dendritic ROI recordings.

Statistical analysis & data presentation

The gender of mice and experiments were not randomized, and investigators were not blinded to conditions of stimulated and nonstimulated dendrite selection during experiments. Trials were randomized by power and stimulated dendrite; MATLAB was used to create experimental block structures, generate phase masks, interface with the SLM, and examine photostimulation-induced activation of dendrites and soma in real time during imaging. To extract photostimulation frames and synchronize them with imaging frames, we used MATLAB to read PackIO output files and imported the resulting photostimulation frames into Python. Data analyses and figures were generated using Jupyter Lab (Python), and statistical analyses were performed using the SciPy Stats package. Data are presented as mean +/- standard error of the mean (s.e.m.) unless otherwise indicated. Video processing, including reading TIFF files and spatial smoothing, was handled using the SciPy multidimensional image processing (scipy.ndimage) package. Statistical analyses comparing responses resulting from stimulation of different dendrites used Wilcoxon rank sum tests, and statistical analyses comparing the activity of different ROIs within the same trial used Wilcoxon signed-rank tests unless otherwise indicated.

Results

Part 1. Single-Target Dendritic Optogenetics

All-optical microscope setup and target identification

To explore the dynamics of dendritic computation *in vivo,* our methodological goal was to selectively activate single dendrites or combinations of dendrites and record the local and global neuronal response in an awake animal. Drawing upon previously described methods (Russell et al., 2022), our all-optical system consisted of an SLM incorporated into a two-photon *in vivo* dual-beam path resonant-scanning microscope (**Fig. 1a**), with both beam paths containing laser sources, power attenuators (photostimulation: internal power modulation via acousto-optic modulator, imaging: Pockels cells), telescopes to alter beam diameter, and beam-steering mirrors. The imaging path utilized an electrically tunable lens (ETL) to enable volumetric imaging of target neurons. On the photostimulation side, uncaging galvanometers were used to direct photostimulation light to single dendritic targets. For later, multi-target experiments, a spatial light modulator (SLM) was used as a beam-patterning device to simultaneously activate multiple dendritic targets. Images were acquired at a 30 Hz frame rate, using a resonant galvo scanning system at 920 nm to image GCaMP signals. Two-photon optogenetic stimulation of dendrites was achieved using an independent light path at 1040 nm. Our existing all-optical system (Fişek et al., 2023) was calibrated by co-registering the two light paths over a field of view of 192 x 192 µm; this was achieved by burning spots, spirals, and five-by-five grids into a fluorescent slide to align the precise location of the photostimulation laser target with the imaging field of view (see **Methods**). An SLM power curve was generated by measuring the post-objective output power for one, two, or three dendritic targets while applying their respective phase masks (**Fig. 1b**). These power curves were used as lookup tables to drive targeted photostimulation of dendrites while standardizing the amount of power delivered to each target across trials. For trials in which single dendrites were targeted, we stimulated each target with the zero order, effectively using the SLM as a mirror; for multi-target trials, we used the Meadowlark Blink software to cycle through different phase masks for each trial to perform holographic photostimulation.

To minimize off-target dendritic activation, we drove ultrasparse expression of two Cre-dependent constructs for simultaneous two-photon calcium imaging and two-photon photostimulation in Layer 2/3 (L2/3) of visual cortex in adult mice. We combined the latest and most highly sensitive calcium indicator jGCaMP8s (Zhang et al., 2021) with a powerful, red-shifted cation channelrhodopsin (ChRmine) linked to a red fluorescent protein (mScarlet) for visualization (Kishi et al., 2022; Marshel et al., 2019). We designed our head fixation system using angled head plates and an axially rotating objective, such that the objective would be optimally aligned with the cortical surface (see **Methods**) and thus parallel to the cortical layers. "Optimal" sparsity was evaluated using the following criteria: **(1)** Three or fewer cells per 385 x 385 µm field of view; **(2)** Target dendrites from one cell do not overlap with virus-expressing dendrites of any other cell, as observed by taking z-stacks of each identified neuron; and **(3)** Reliable co-expression of GCaMP8s and ChRmine at healthy, non-saturated levels, yielding fluctuating calcium signals during spontaneous recordings (920 nm) and visible mScarlet expression at 765 nm (**Fig. 1c**). Criteria **(1)** and **(2)** were satisfied with sufficient dilution of Cre virus (see **Methods**); however, during viral optimization, we found that the GCaMP and ChRmine compete for transfection of target cells such that most cells express nearly exclusively one of the two viruses. The difficulty of obtaining a good balance for GCaMP-to-ChRmine expression without compromising the "read" or "write" capabilities of either posed a major challenge in performing *in vivo* dendritic optogenetics at ultrasparse levels of expression (n = 10 cells recorded from 3 animals, n = 3 cells across 2 animals with moderately healthy responses to photoactivation without saturation).

After identifying target neurons with adequate co-expression of opsin and calcium indicator at ultrasparse levels in the network (**Fig. 1c**), we wrote a MATLAB-based graphical user interface (GUI) to convert user-defined dendritic targets to SLM coordinates for targeted photostimulation (**Fig. 1d**). Videos containing 1000 frames of spontaneous activity were acquired at 30 Hz and motion-corrected before target selection. Registered images (either two- or three-dimensional) are read by the GUI, which prompts the user to set the "ETL Zero" at the frame containing the soma before allowing users to manually draw ROIs to be targeted by the SLM. The user is asked to confirm the centroids of these ROIs before saving them as an array of pixel coordinates—subsequently used for phase

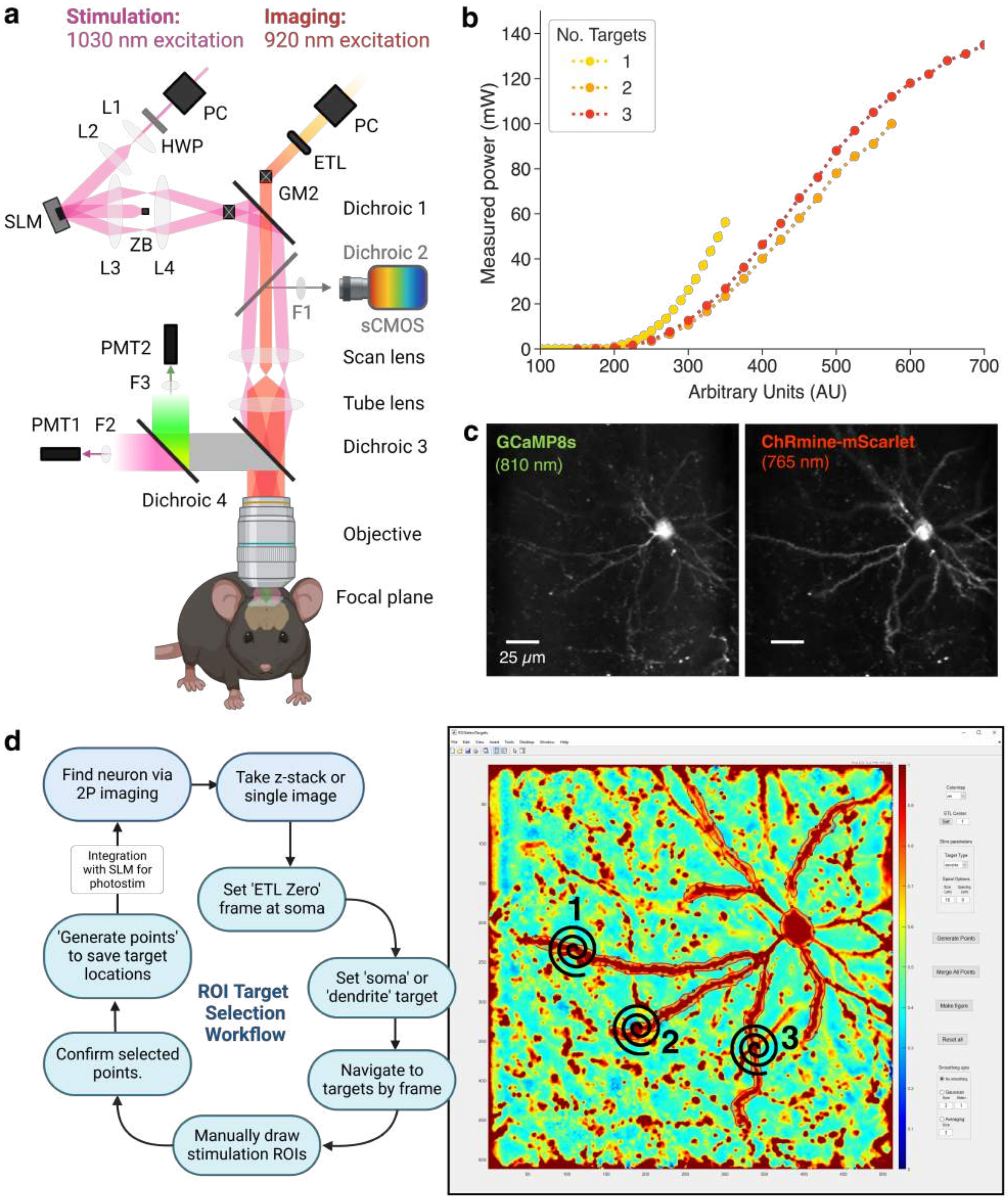

Figure 1. All-optical microscope setup and target identification.

a) Schematic of all-optical setup, including two-photon resonant scanning and two-photon patterned photostimulation via spatial light modulator (SLM). Adapted from Packer et al. (2014). ETL, electrically tunable lens. F1, 675/67 nm bandpass filter. F2: 525/70 nm bandpass filter. F3: 607/45 nm bandpass filter. GM, galvanometer. HWP, half-wave plate. L1-L4, lens. PC, Pockels Cells. PMT1 (pink) and PMT2 (green), photomultiplier tubes. SLM, spatial light modulator. ZB, zero order block.

b) Power curve for 1, 2, or 3 simultaneous targets via SLM-based photostimulation.

c) Example neuron with GCaMP8s (left) and corresponding ChRmine-mScarlet expression (right).

d) Dendritic target identification workflow and graphical user interface (MATLAB).

mask generation and SLM integration. Each pixel coordinate denotes the centroid of a 20 µm diameter spiral centered over the target dendritic axis. The rationale for spiraling over dendritic targets rather than activating a single point was two-fold: **(1)** by spiraling over a larger area rather than focusing the laser at a single point, we sought to minimize the amount of damage on the cell; and **(2)** As the mouse moves or shifts position during the recording, spiraling over a 20 µm diameter ensures that the dendrite will be reliably stimulated in spite of brain movement, rather than shifting out of the point of stimulation. Together with the use of a red-shifted opsin, ultra-sparse co-expression of GCaMP8s and ChRmine, and the target selection GUI, we were able to validate our all-optical workflow for small FOV dendritic photostimulation and imaging.

Single-target dendritic 2P photostimulation and simultaneous 2P imaging

To validate the all-optical approach for *in vivo* dendritic optogenetics, we first characterized the intensity-dependent activation of single dendritic targets with increasing photostimulation laser power. Due to low signal-to-noise ratios of apical dendrites, we restricted our stimulation targets to basal dendrites of Layer 2/3 pyramidal neurons on the same imaging plane as the soma (**Fig. 2a**). Dendritic targets were chosen based on the following criteria: fluctuating GCaMP8s signals at baseline activity levels, adequate ChRmine expression, and no overlap with other dendrites in the region of stimulation (20 µm diameter spiral). When multiple dendrites met these criteria, we sought to vary the distances between the stimulation targets and the soma, as well as the angle at which the dendrites branched from the soma.

To verify co-expression of calcium indicator and opsin, and to identify neuronal morphology, time-averaged expression images, and volumetric z-stacks were obtained for each neuron before experimental recordings (**Fig. 2b**). For each neuron, recordings consisted of three blocks with successively increasing powers (Block 1: 1-10 mW; Block 2: 10-26 mW; Block 3: 24-40 mW). Each block consisted of 150 trials randomizing **(1)** one of three dendritic targets (denoted in this thesis as D1, D2, and/or D3), and **(2)** the power delivered to the selected dendritic target (five possible powers per block). In each trial, a 10 ms photostimulation laser pulse at 1040 nm was delivered to the target dendrite and spiraled using the uncaging galvanometers; a 4 s delay followed each 10 ms stimulation period to allow calcium

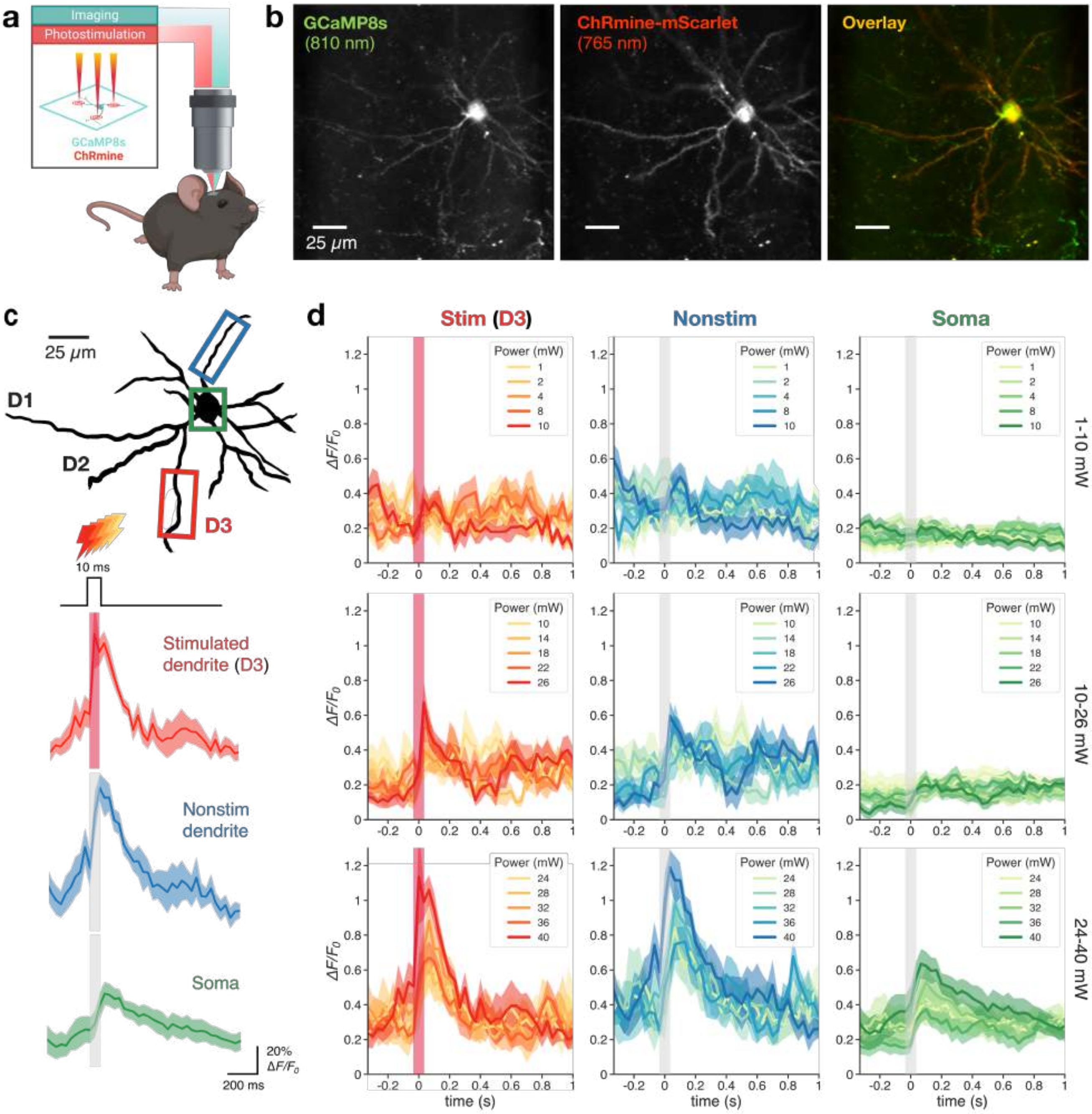

Figure 2. Single-target dendritic 2P photostimulation and simultaneous 2P calcium imaging.
a) Schematic of the technical goal. Ultra-sparse Cre injection drives single-cell expression of a highly sensitive calcium sensor (GCaMP8s), which confers the ability to optically readout neural activity (teal). A non-soma-restricted opsin (ChRmine) enables targeted photostimulation of dendrites (red).
b) Expression of GCaMP8s (left), ChRmine (center), and both (right) in a representative neuron.
c) Trial structure and example spike-triggered average response. Three dendritic targets (D1-D3) were identified using Bruker's PrairieView software. In each trial, a randomized target and power is directed to the cell using uncaging galvanometers for 10 ms, followed by a 4 s delay. Responses were recorded from stimulated dendrites (red) and compared to responses at non-stimulated dendrites (blue) and soma (green). Distance between soma center and stimulation spirals: D1, 95.6 μm; D2, 68.5 μm; D3, 54.6 μm.
d) Average photostimulation-triggered responses at varying power levels (one block per row) for stimulated dendrites, non-stimulated dendrites, and somatic responses (n = 10 trials/power, 1 dendrite).

signals to return to baseline and to allow the uncaging galvo to reposition at the next dendritic target (**Fig. 2c**).

On average, the dendritic targets were about 73 µm from the soma (target distances ranged from 54 - 96 µm from the soma). Figure 2d illustrates the average photostimulation-triggered responses for Dendrite 3 (D3, 10 trials/power), showing calcium signals increasing with higher photostimulation powers (for D1 and D2 responses, see **Supplementary Fig. 1 & 2,** respectively). Two-photon imaging of GCaMP8s responses revealed a positive correlation between the power delivered and calcium response recorded from the stimulated dendrite (**Fig. 3a,** n = 450 trials, 3 dendrites, 1 neuron, r = 0.264, p = 1.24 x 10^{-8}, Pearson correlation), with significant increases in dendritic response between power blocks (**Fig. 3b,** Block 1 vs. Block 2, p = 0.01, Block 2 vs. Block 3, *p* = 1.32 x 10^{-6}, Block 1 vs. Block 3, *p* = 1.44 x 10^{-13}, Wilcoxon rank sum test). While Dendrite 1 (D1) showed no significant correlation between photostimulation power and response (**Fig. 3c, Supplementary Fig. 1,** n = 150 trials, r = 0.00252, p = 0.976, Wilcoxon signed-rank test), Dendrite 2 (D2) and Dendrite 3 (D3) exhibited a significant positive correlation between power and response (**Fig. 3d-e, Supplementary Fig. 2,** D2, r = 0.212, p = 0.0899, D3, r = 0.511, p = 2.35 x 10^{-11}), with D3 displaying the highest activity increase with power. Interestingly, we also observed signals at the soma and in non-stimulated dendrites (**Fig. 3f-g**) as the photostimulation power increased (non-stimulated dendrites, Block 1 vs. Block 2, *p* = 0.00582, Block 2 vs. Block 3, *p* = 7.77 x 10^{-14}, Block 1 vs. Block 3, *p* = 1.90 x 10^{-20}; soma, Block 1 vs. Block 2, *p* = 0.000277, Block 2 vs. Block 3, *p* = 1.38 x 10^{-7}, Block 1 vs. Block 3, *p* = 0.0362, Wilcoxon rank sum tests), indicating an intensity-dependent increase in global as well as stimulated dendrite response. Together, these results provide a basic proof-of-principle demonstration for *in vivo* dendritic photostimulation and simultaneous two-photon calcium imaging of target and off-target regions.

Part 2. Dissecting components of dendritic activation

Dendritic photostimulation reveals action potential backpropagation

To characterize the spatial features of dendritic activation across stimulated targets, we extracted the median filtered averaged intensity values along the

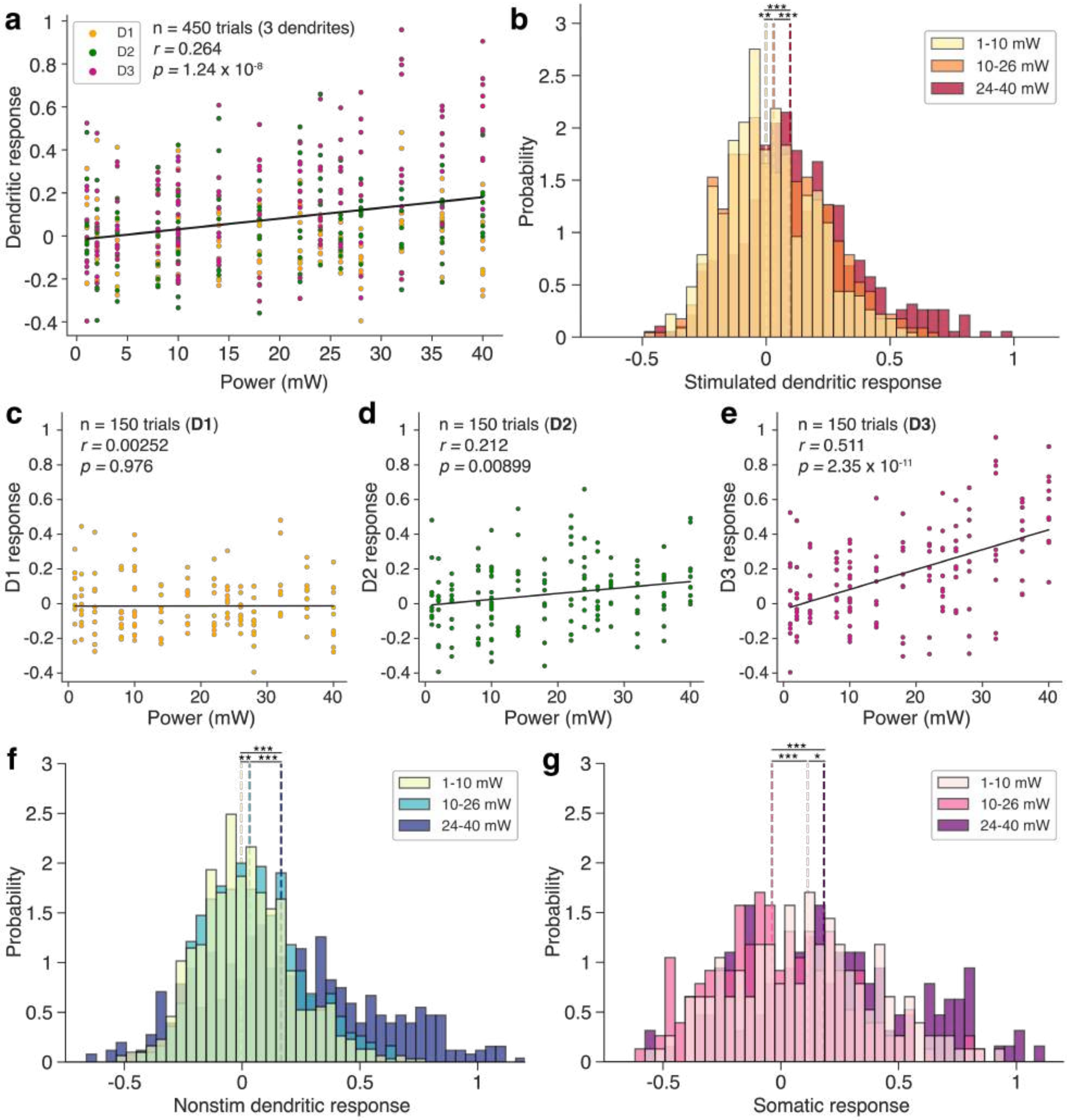

Figure 3. Single-target response dynamics.

a) Correlation between photostimulation power and responses of stimulated dendrites (Pearson correlation: 0.264, $p = 1.24 \times 10^{-8}$, n = 450 trials, 3 dendrites from 1 neuron). Each point denotes a single trial response.

b) Trial responses of stimulated dendrites. Colors indicate binned powers. Mean response for stimulated dendrites significantly increased with increasing powers (Block 1 vs. Block 2, $p = 0.01$, Block 2 vs. Block 3, $p = 1.32 \times 10^{-6}$, Block 1 vs. Block 3, $p = 1.44 \times 10^{-13}$, Wilcoxon rank sum test). Dashed lines indicate median response across all trials in the indicated experimental block.

c-e) Correlation between power and dendritic response for targets D1 (c), D2 (d), and D3 (e).

f) Trial responses of non-stimulated dendrites. Colors indicate binned powers. Mean response for non-stimulated dendrites significantly increased with increasing powers (Block 1 vs. Block 2, $p = 0.00582$, Block 2 vs. Block 3, $p = 7.77 \times 10^{-14}$, Block 1 vs. Block 3, $p = 1.90 \times 10^{-20}$, Pearson correlation).

g) Trial responses of the soma. Colors indicate binned powers. Somatic mean response significantly increased with increasing powers (Block 1 vs. Block 2, $p = 0.000277$, Block 2 vs. Block 3, $p = 1.38 \times 10^{-7}$, Block 1 vs. Block 3, $p = 0.0362$, Wilcoxon rank sum test).

(* $p < 0.05$, ** $p < 0.01$, *** $p < 0.001$; All pairwise t-tests underwent Bonferroni corrections. All response measures are in units of $\Delta F/F_0$; see **Methods**) dendritic ROI before, immediately after, and 0.4 s post-stimulation (**Fig. 4a;** see also **Supplementary Fig. 3a, Supplementary Fig. 4**). Computing the baseline-normalized difference in mean response between the immediate post- and pre-stimulation period revealed a scattering of high-intensity regions across the length of the dendritic ROI (**Fig. 4b,** top panel). By the recovery (late post-stimulation) period, these increased calcium signals returned to baseline levels (**Fig. 4b,** bottom panel). We then averaged the time- and distance-dependent response from the time point of stimulation and distance from the target center, respectively (**Fig. 4c**). Rather than a localized activation near the target center that spreads outward with time, we observed a widespread increase in calcium response that was spatially extended along the dendritic shaft post-stimulation. Moreover, we found regions along the dendritic ROI with increased GCaMP fluorescence signals post-stimulation. We hypothesize that these regions might contain dendritic spines, which have larger volumes and subsequently higher total levels of GCaMP—leading to higher signal-to-noise ratios (SNR) during dendritic activation.

The measured dendritic responses consist of two separate components: a "local," direct effect driven by optogenetic depolarization of the targeted dendrite, and a "global" component due to backpropagating action potentials from the soma. Surprisingly, our results suggest that a sizable proportion of the dendritic response we observe is a result of backpropagating action potentials rather than local activation. If so, one would expect to observe strong correlations between the photostimulation-triggered response in stimulated and non-stimulated targets, including non-stimulated dendrites and soma. Accordingly, across all trials, there was a strong correlation between the response recorded at the stimulated dendrite and the corresponding response at non-stimulated dendrites (**Fig. 5a,** n = 5,400 trials, 1 neuron, r = 0.874, $p = 7.50 \times 10^{-16}$, Pearson correlation). Furthermore, the stimulated dendritic responses and somatic responses were also correlated (**Fig. 5b,** n = 5,400 trials, r = 0.731, $p = 4.06 \times 10^{-41}$, Pearson correlation), as well as between the somatic response and non-stimulated dendritic response (**Fig. 5c,** n = 5,400 trials, r = 0.790, $p = 2.81 \times 10^{-78}$, Pearson correlation). When comparing the distribution of responses per trial, there was no significant difference in the stimulated dendrite, non-stimulated dendrite, or somatic activity evoked by photostimulation (**Supplementary Fig. 3e**). It is likely that the link between the stimulated and non-stimulated dendritic response is mediated through somatic

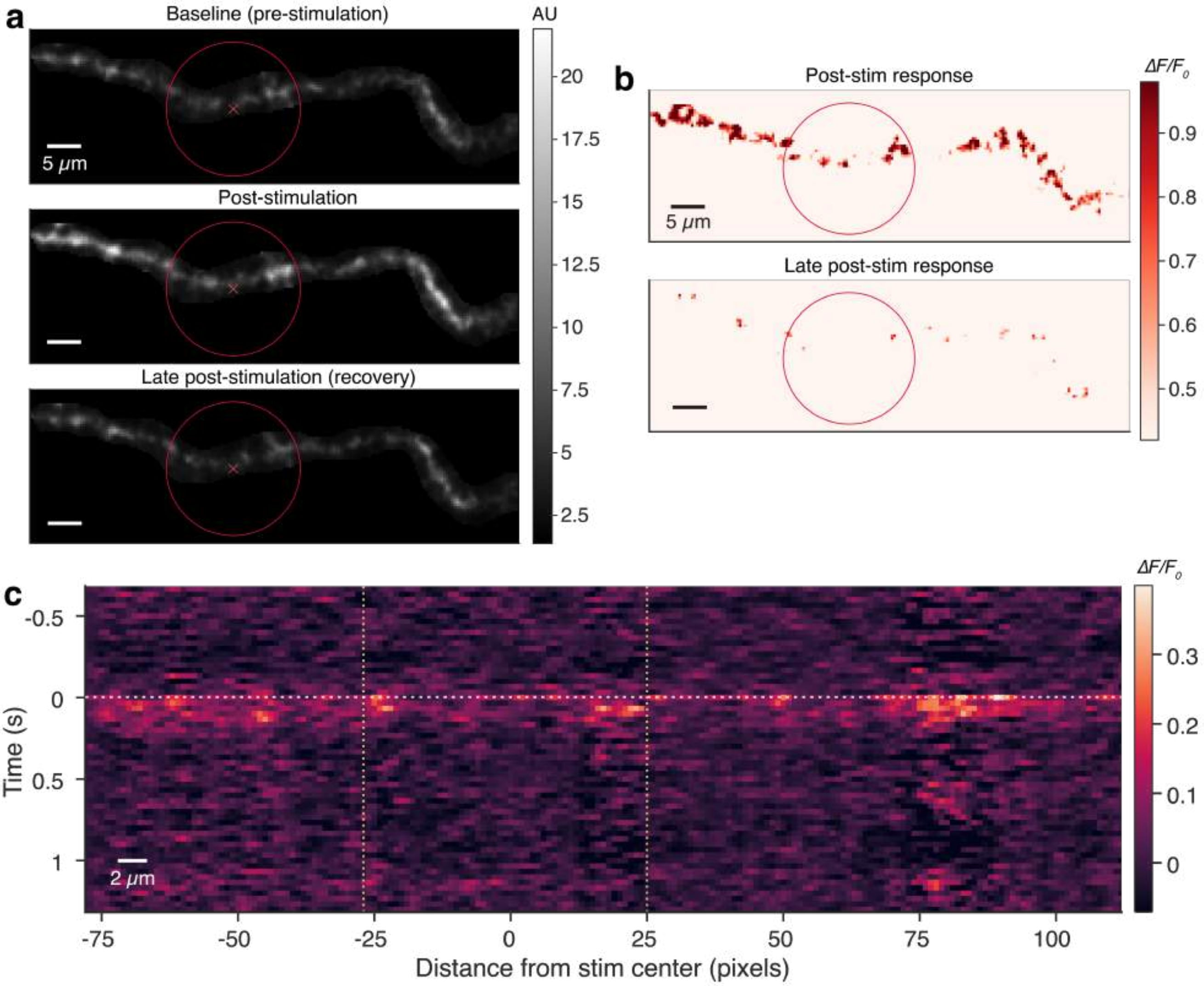

Figure 4. Spatial characteristics of dendritic activation.

a) Example FOV of dendritic (D3) activation averaging five frames pre-stimulation (top), five frames immediately post-stimulation (center), and five frames during the "late" post-stimulation recovery period (0.33-0.5 s post-stim, bottom) at 40 mW. Red x's indicate photostimulation spiral centroid. Red circle indicates spiral extent. Color indicates raw intensity value (AU, arbitrary units). Orientation of dendritic segment (from left to right) for all plots is proximal to distal.

b) Baseline-normalized response of target dendrite during the immediate post-stimulation period (top) and the late post-stimulation period (bottom). Color indicates change in fluorescence relative to baseline.

c) Heat map showing spatial spread of dendritic activation across time (rows) and distance from the photostimulation spiral center (columns). Horizontal dotted line (t = 0) indicates time at which the target dendrite was stimulated. Vertical dotted lines indicate spatial extent of the photostimulation spiral. Intensity values are baseline-subtracted. Color indicates change in fluorescence relative to baseline.

(AP) activation and subsequent backpropagating action potentials, which results in correlated global calcium responses across all dendrites.

If the observed response in stimulated dendrites is largely due to AP backpropagation rather than to local photostimulation, dendritic ROIs that are closer to the soma may exhibit larger calcium signals for any given power than dendritic ROIs further away from the soma (Larkum et al., 2007; Stuart & Sakmann, 1994; Waters et al., 2003). On the other hand, if the observed responses are due to localized dendritic depolarization, there should be no difference in stimulated dendritic responses when controlling for photostimulation power. To test this hypothesis, for each stimulated dendritic target, we computed the mean response at each power used. To determine whether there was a relationship between target-to-soma distance and mean response, we performed pairwise Wilcoxon rank sum tests for all recordings at the soma (**Fig. 5d**) and at the stimulated dendrite (**Fig. 5e**), comparing the responses across different stimulated branches. At lower powers, there was no discernible difference in measured response at the soma (**Supplementary Fig. 3b,** $p > 0.05$ for all pairwise combinations of stimulated dendrites in Blocks 1 and 2, Wilcoxon rank sum test). Similarly, at low powers, we found small but largely indistinguishable activity increases in the stimulated dendritic responses (**Supplementary Fig. 3c,** $p = 0.00865$, D1 to D3; $p > 0.05$ for all other combinations, Wilcoxon rank sum test). At higher powers (Block 3, ≥ 24 mW), however, the measured activity in both somatic and dendritic ROIs increased in a distance-dependent fashion (**Supplementary Fig. 3b-c**). Despite similar increases in somatic and dendritic activity at higher powers, there was no significant difference in the dendrite-to-soma response ratio between stimulated dendrites, suggesting an indiscernible local component of dendritic activation beyond backpropagation (**Fig. 5f,** $p > 0.05$, Wilcoxon rank sum test).

The increase in recorded response at the stimulated dendrite with decreasing distances from the soma lends support to the hypothesis that most of the observed dendritic responses are due to AP backpropagation. One possible mechanism underlying this trend is as follows: at lower stimulation powers (< 24 mW), there is not enough depolarization due to ChRmine activation for a single dendrite to initiate an action potential at the soma. Thus, at these powers, the measured responses at each stimulated dendrite (and somatic) ROI are comparable—either because they drive similar responses, or because the level of local calcium entry into the dendrite at subthreshold depolarization (which does not involve the recruitment of voltage-gated calcium channels) is too low to detect using GCaMP. At higher powers (≥ 24 mW), there may be enough depolarization due to ChRmine activation such that a single dendritic depolarization is sufficient to drive an action potential at the soma. In this regime, for similar powers, the recorded calcium signal at the *soma* is not substantially different across stimulated dendrites ($p = 0.0163$ for D1 to D3, $p > 0.05$ for all other combinations, Wilcoxon rank sum test). However, for dendritic ROIs closer to the soma, there may be less distance for backpropagating action potentials to travel and therefore lower bAP attenuation. Accordingly, at stimulation powers above 24 mW, we found that the dendritic ROIs closer to the soma had substantially higher mean responses (**Fig. 5e,** less attenuation; $p < 0.01$ for all combinations of stimulated dendrites) whereas the ROIs further from the soma had lower mean responses (**Fig. 5e,** further distance traveled, thus higher attenuation and lower response).

Isolating local and backpropagating components of dendritic activation

The strong global component of backpropagation does not exclude that calcium signals measured at the dendrite may also include a local contribution. To distinguish local contributions from global activity, we first performed a radial distance-dependence analysis for powers at or above 24 mW (**Fig. 6a**). For each photostimulation target (red dots), the Euclidean distance (d) between the target centroid and the soma center (s, blue star) was calculated. For each target, an imaginary circle with radius d and center s was drawn (dotted line), such that the circle intersects with the stimulation point on the target dendrite and all other non-stimulated dendrites (**Fig. 6a**). We then made pairwise comparisons of mean response across recorded and stimulated dendrites at equal distances from the soma center (**Fig. 6b-c,** n = 1 neuron, 10 trials per recording site).

First, we compared the responses along the same *recorded dendrite* (**Fig. 6b**, colored boxes aligned with the corresponding ROIs in the image from **Fig. 6a**). Regardless of stimulation target, as we recorded ROIs closer to the soma, there was an increase in dendritic mean response. We then compared the mean responses of dendritic ROIs along the same *radial distance* (**Fig. 6c-d**): for example, stimulating D1 and comparing its mean response to that of D2 and D3 along the same distance from the soma center. When controlling for distance, the

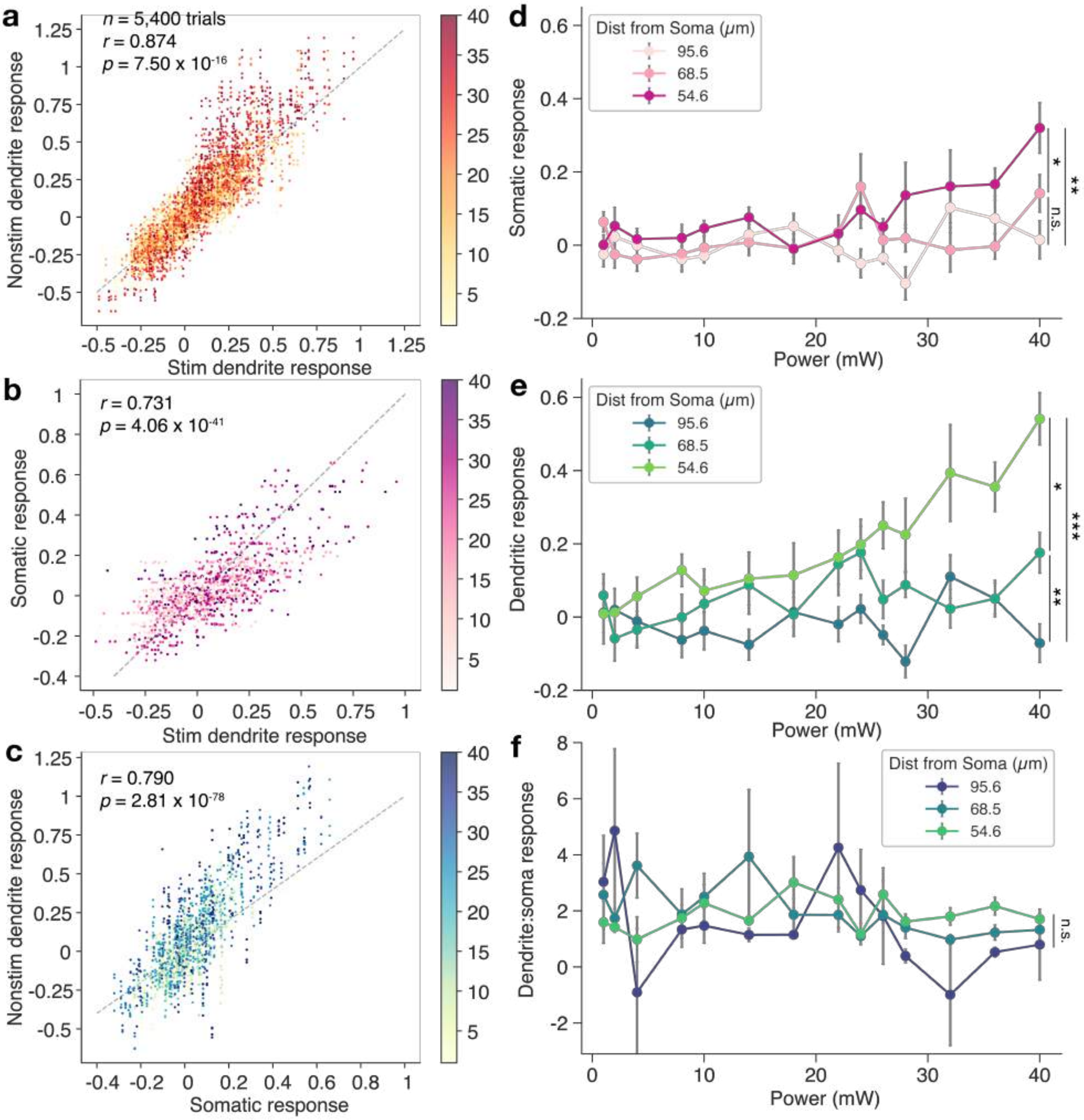

Figure 5. Correlation of photostimulation-evoked activation across dendrites and soma.

a-c) Correlation between photostimulation-triggered response of stimulated dendrites (n = 3) and non-stimulated dendrites (n = 4) (a, $r = 0.874$, $p = 7.50 \times 10^{-16}$, Pearson correlation), stimulated dendrites and soma (b, $r = 0.731$, $p = 4.06 \times 10^{-41}$, Pearson correlation), and soma and non-stimulated dendrites (c, $r = 0.790$, $p = 2.81 \times 10^{-78}$, Pearson correlation). All trials colored by photostimulation power (mW) delivered to target (n = 5,400 trials, 3 dendrites on one neuron). Dashed lines denote unity line.

d) Mean somatic response, averaged across trials, at increasing powers. Colors indicate the distance of the stimulated dendritic target from the soma center: D1, 95.6 μm; D2, 68.5 μm; D3, 54.6 μm. (D1 vs. D2, $p = 0.383$, D2 vs. D3, $p = 0.0149$, D1 vs. D3, $p = 0.00439$, Wilcoxon rank sum test)

e) Mean dendritic response, averaged across trials, at increasing powers. Colors indicate the distance of the stimulated dendritic target from the soma center. (D1 vs. D2, $p = 0.00770$, D2 vs. D3, $p = 0.0101$, D1 vs. D3, $p = 0.000114$, Wilcoxon rank sum test)

f) Ratio of dendritic to somatic response, averaged across trials, at increasing powers. Colors indicate the distance of the stimulated dendritic target from the soma center. (D1 vs. D2, $p = 0.215$, D2 vs. D3, $p = 0.854$, D1 vs. D3, $p = 0.214$, Wilcoxon rank sum test)

(* $p < 0.05$, ** $p < 0.01$, *** $p < 0.001$; All pairwise t-tests underwent Bonferroni corrections. All response measures are in units of $\Delta F/F_0$.)

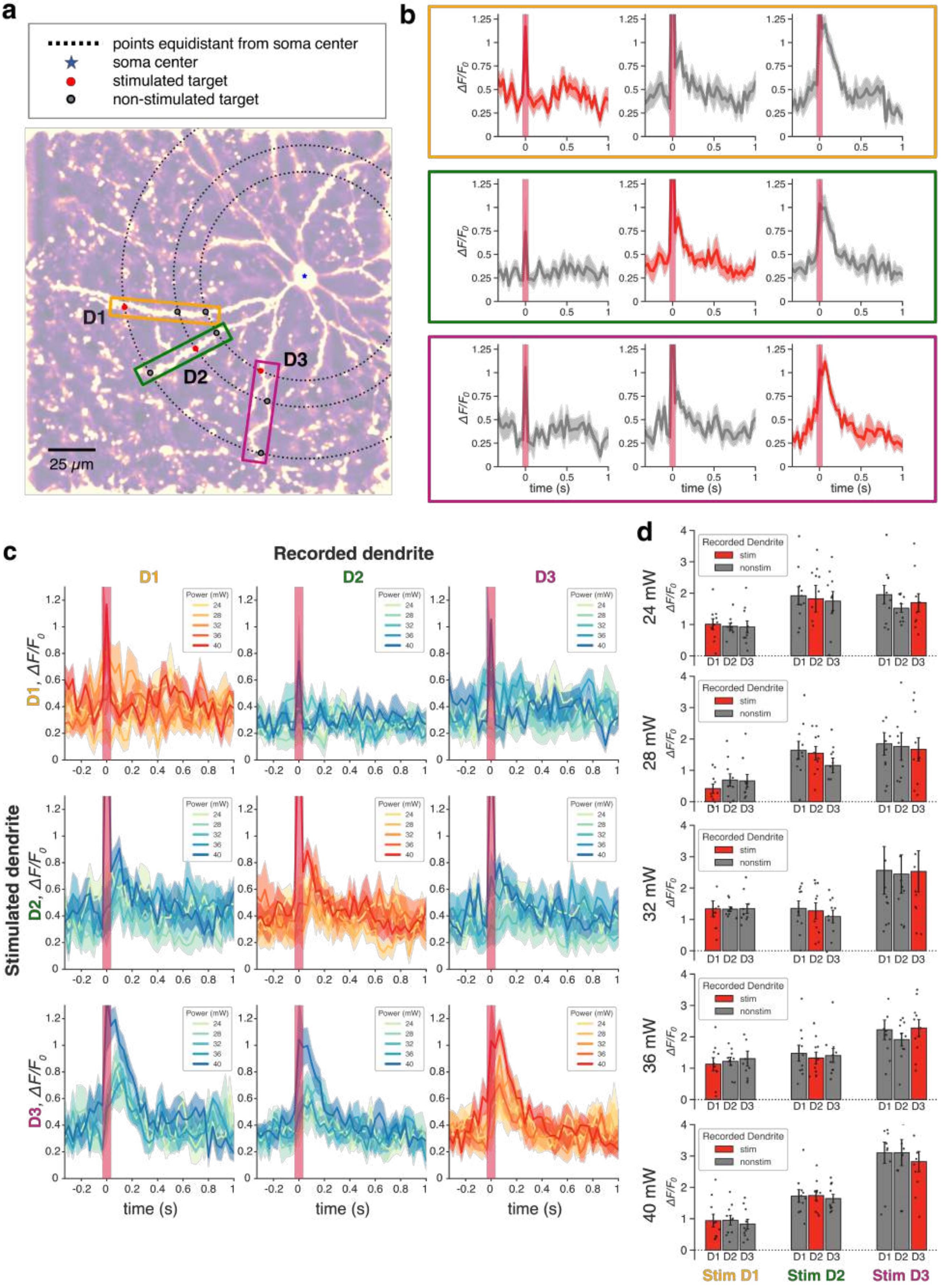
a
points equidistant from soma center
soma center
stimulated target
non-stimulated target
D1
D2
D3
25 μm
b
ΔF/F₀
time (s)
c
Recorded dendrite
D1
D2
D3
Stimulated dendrite
D1, ΔF/F₀
D2, ΔF/F₀
D3, ΔF/F₀
Power (mW)
24
28
32
36
40
time (s)
d
24 mW
28 mW
32 mW
36 mW
40 mW
ΔF/F₀
Recorded Dendrite
stim
nonstim
D1 D2 D3
Stim D1
Stim D2
Stim D3

Figure 6. Radial distance-dependence of dendritic activation.

a) Schematic of analysis. For each photostimulation target (red dots), the Euclidean distance (*d*) between the target centroid and the soma center (*s*, blue star) was calculated. For each target, an imaginary circle with radius *d* and center *s* was drawn (dotted line), such that the circle intersects with the stimulation point on the target dendrite and all other non-stimulated dendrites. We compared mean response along recorded dendrites, as well as across distance-equalized points on each stimulation radius.

b) Traces of dendritic ROIs from the matching colored box in (a), when stimulated at 40 mW. Traces from left to right correspond to the boxed traces from the outermost to innermost circle. Red traces denote stimulation targets. Gray traces denote distance-matched dendritic ROIs. Note that at distances closer to the soma, the dendritic activation increases regardless of stimulation target. (n = 10 trials/site, 1 neuron)

c) Comparison of stimulated dendritic activation with the corresponding response of other dendrites at equal distances from the soma. Rows indicate stimulated dendrite; columns indicate recorded dendrite. Red and blue traces denote stimulation targets and non-stimulated dendrites, respectively.

d) Quantification of mean responses from (c), separated by power. Within each row, clusters indicate stimulated dendrite (Stim D1-D3), and bars within each cluster indicate the dendrite on which the ROI trace was extracted. Note that along distance-matched locations from the stimulated dendrite, there is no significant difference in mean response. All values are non-significant ($p > 0.05$, Wilcoxon rank sum test).

observed differences in dendritic responses were eliminated (**Fig. 6d**) — i.e., at equidistant dendritic ROIs from the soma, there were no significant differences in dendritic activation depending on stimulated/non-stimulated target status. In other words, regardless of the target location, all ROIs along a given radial distance from the soma exhibit similar responses to dendritic photostimulation at powers ≥ 24 mW.

At 24-40 mW, stimulating individual dendrites sometimes drives APs at the soma, which in turn leads to bAP-evoked calcium signals at the dendrites. If we control for somatic activity (i.e., examine trials with similar somatic responses), stimulating D2 should drive a response in D2 that is due to both bAP and local activation (“bAP + local”), whereas stimulating D3 should drive a response in D2 that is solely due to backpropagation only (“bAP only”). Likewise, when recording from D3 while controlling for somatic activity, stimulating D3 should drive “bAP + local” responses, while stimulating at D2 should drive responses due only to bAPs. For both dendrites, comparing the “bAP + local” responses to the “bAP only” responses should allow us to extract the local component of dendritic activation. Therefore, to further distill the contributions of local photostimulation to the observed dendritic responses, we next performed a matched distribution comparison between evoked responses at D2 and D3 (**Fig. 7a, Supplementary Fig. 5;** see **Methods**). We first quantified the distribution of somatic activation evoked by either D2 or D3 (**Fig. 7b**, n = 100 trials, 1 neuron). For bins with matching, non-negative somatic responses, we sampled from the higher-frequency condition to obtain two datasets (one from each stimulated dendrite) with the same number of trials. From these somatic response-matched trial sets, we compared the dendritic activation of D3 when D2 was stimulated (indicating D3 activation due to bAP only) with the dendritic activation when D3 itself was stimulated (bAP + local activation) (**Fig. 7c,** n = 46 samples, *p* = 0.0215, Wilcoxon rank sum test). Bootstrapping (n = 1,000 repetitions) yielded a distribution of D3 responses for each condition (**Fig. 7d**), as well as the distribution of p-values for each Wilcoxon rank sum test between matched datasets (**Fig. 7e;** mean p-value: 0.114). After each sampling repetition, we estimated the local component of dendritic activation by computing the difference between the mean “bAP + local” and “bAP only” evoked responses across all sampled trials. Overall, the mean estimated local contribution to dendritic (D3) activation was 0.179 $\Delta F/F$, or 41.7%, of the mean response measured in D3 (**Fig. 7f**). However, we were unable to reliably isolate the effects of local activation from backpropagation on D2, as the “bAP + local” and “bAP only” response distributions were not significantly different from each other (**Supplementary Fig. 5**). Furthermore, the average “bAP only” response was on average higher than that of “bAP + local” response. Possible reasons for this counterintuitive result include differences in the stimulation efficiency between D2 and D3, or a direct effect of D3 stimulation on D2 calcium signals independent of bAPs due to the spread of stimulation-evoked depolarization between the dendrites. In a similar analysis, we attempted to extract the “local” activation component for each dendrite by computing the response ratio of the target dendrite when itself was stimulated versus when the opposite dendrite was stimulated. Doing so for D2 and D3 yielded no non-linearities between dendritic responses at higher powers (**Fig. 7g-h**).

Together, our results suggest that the responses observed at dendritic ROIs post-stimulation are largely due to backpropagating action potentials but may contain a small local component due to direct dendritic photostimulation. While comparing somatic response-matched distributions may be useful for isolating local and global (bAP) components of dendritic activation, it would require more trials with carefully chosen photostimulation targets such that they are both equidistant to the soma and can reliably evoke somatic responses.

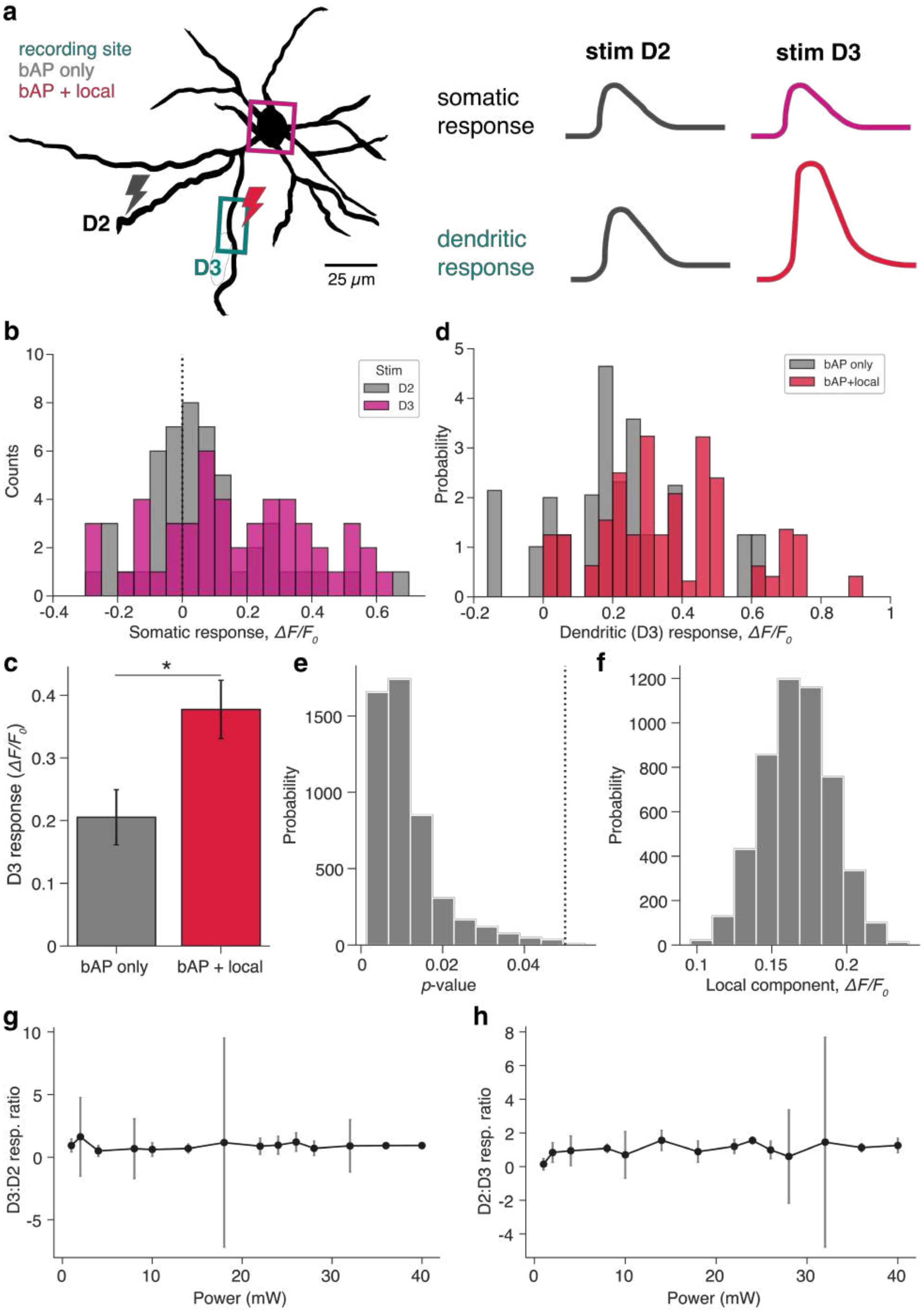
a
recording site
bAP only
bAP + local
D2
D3
25 μm
stim D2
stim D3
somatic response
dendritic response
b
Counts
Stim
D2
D3
Somatic response, $\Delta F/F_0$
-0.4
-0.2
0
0.2
0.4
0.6
0
2
4
6
8
10
d
Probability
bAP only
bAP+local
Dendritic (D3) response, $\Delta F/F_0$
-0.2
0
0.2
0.4
0.6
0.8
1
0
1
2
3
4
5
c
*
D3 response ($\Delta F/F_0$)
0
0.1
0.2
0.3
0.4
bAP only
bAP + local
e
Probability
p-value
0
0.02
0.04
0
500
1000
1500
f
Probability
Local component, $\Delta F/F_0$
0.1
0.15
0.2
0
200
400
600
800
1000
1200
g
D3:D2 resp. ratio
Power (mW)
0
10
20
30
40
-5
0
5
10
h
D2:D3 resp. ratio
Power (mW)
0
10
20
30
40
-4
-2
0
2
4
6
8

Figure 7. Isolation of local and backpropagation (bAP) components.

a) Schematic of experiment and data analysis method for extracting the local component of dendritic activation in dendrite 3 (D3). Trials in which dendrite 2 (D2) or D3 were stimulated were matched for somatic activation (top traces). Of these somatic response-matched trials, those in which D2 was stimulated ("bAP only") were compared to those in which D3 was stimulated ("bAP + local").

b) Histogram of somatic activation induced by stimulating either D2 (grey) or D3 (magenta). Trials in which non-negative somatic responses overlapped were sampled. Bootstrapping was achieved by resampling from shared bins 1,000 times. (n = 100 trials, 1 neuron)

c) Example outcome from a single resample (n = 46 samples, 23 samples per condition). Of the sampled somatic response-matched trials, the "bAP only" condition was compared to the "bAP + local" condition as recorded from D3 activation ($p = 0.0215$, Wilcoxon rank sum test).

d) Histogram of recorded D3 responses due to D2 (grey, bAP only) or D3 (red, bAP + local) stimulation, over 1,000 rounds of resampling from the somatic response-matched trials in (b).

e) Histogram of *p*-values obtained from the 1,000 resamples. *P*-values were computed using the Wilcoxon rank sum test for each comparison of "bAP only" and "bAP + local" conditions. Dotted line, $p = 0.05$

f) Histogram of estimated local component in $\Delta F/F_0$, computed by subtracting "bAP only" activation of D3 from the "bAP + local" activation for each round of resampling.

g) Trial-averaged ratio of D2 responses when D2 was stimulated (bAP + local) versus when D3 was stimulated (bAP only). ($p > 0.05$, one-way analysis of variance (ANOVA)) (n = 10 trials/dendrite,1 neuron)

h) Trial-averaged ratio of D3 responses when D3 was stimulated (bAP + local) versus when D2 was stimulated (bAP only). ($p > 0.05$, one-way ANOVA) (n = 10 trials/dendrite,1 neuron)

Part 3. Simultaneous Multi-Target Dendritic Activation

Multiple-target dendritic activation and simultaneous 2P calcium imaging of responses

After validating our all-optical approach for 2P photostimulation and imaging of single dendritic targets, we extended our approach to investigate the activation of multiple dendritic targets simultaneously (**Fig. 8a**). After generating phase masks for combinations of 1, 2, or 3 dendritic targets, we executed trials (separated into three blocks with increasing power sets) that randomized the power delivered per target and the target combination. For each dendritic target and photostimulation power, we quantified the mean response for single-, double-, and triple-target activation (D1 responses in **Fig. 8b-c;** for D2 and D3 responses, see **Supplementary Fig. 6-7**, respectively). Single-target activation denotes trials in which the dendrite of interest (DOI) was stimulated alone; double-target trials involve any two-dendrite stimulation trials containing the DOI. Triple-target trials consisted of any trial where all three dendrites were simultaneously activated. For most photostimulation powers, there was a positive trend between the number of targets simultaneously activated and the mean response (**Fig. 8c-e,** 1 vs. 2 targets, $p = 9.22 \times 10^{-6}$, 2 vs. 3 targets, $p = 1.43 \times 10^{-22}$, 1 vs. 3 targets, $p = 2.87 \times 10^{-30}$, Wilcoxon rank sum tests).

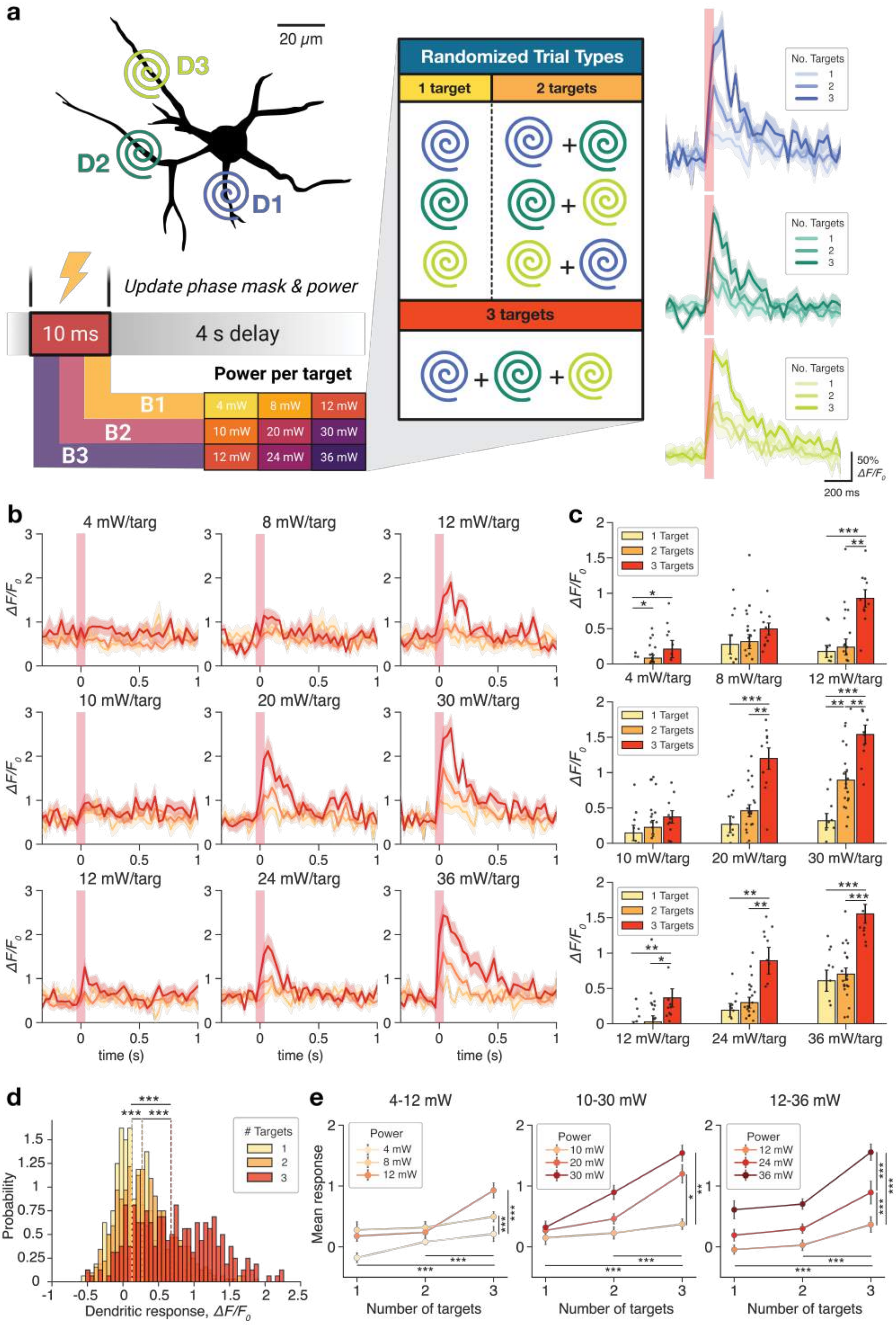
a
20 μm
D3
D2
D1
Randomized Trial Types
1 target
2 targets
3 targets
Update phase mask & power
10 ms
4 s delay
Power per target
B1
B2
B3
4 mW
8 mW
12 mW
10 mW
20 mW
30 mW
12 mW
24 mW
36 mW
No. Targets
1
2
3
50% ΔF/F0
200 ms
b
4 mW/targ
8 mW/targ
12 mW/targ
10 mW/targ
20 mW/targ
30 mW/targ
12 mW/targ
24 mW/targ
36 mW/targ
ΔF/F0
time (s)
0
0.5
1
2
3
c
1 Target
2 Targets
3 Targets
ΔF/F0
0
0.5
1
1.5
2
*
**
***
d
Targets
1
2
3
Probability
Dendritic response, ΔF/F0
-1
-0.5
0
0.5
1
1.5
2
2.5
0.25
0.75
1.25
***
e
4-12 mW
10-30 mW
12-36 mW
Power
4 mW
8 mW
12 mW
10 mW
20 mW
30 mW
12 mW
24 mW
36 mW
Mean response
Number of targets
1
2
3

Figure 8. Multiple-target dendritic activation and simultaneous 2P calcium imaging of response.
a) Schematic of multi-target photostimulation trial structure and sample responses. Before each experiment, three dendritic targets (D1, D2 and D3) were identified on a neuron expressing GCaMP8s and ChRmine. In each block, one of three powers was sampled (lower left) and one of seven combinations targeting 1, 2, or 3 dendrites simultaneously (center) were randomly executed via a 10 ms photostimulation pulse, followed by a 4 s delay. Example responses at 30 mW/target are shown (right) for each dendrite and 1, 2, or 3 target activation.
b) Photostimulation-triggered averages recorded from a single target ROI (D1, n = 1 neuron, 1 mouse) by power and number of targets simultaneously activated. "1 target" refers to individual (D1) activation; "2 targets" refer to any two-target combination that includes D1; "3 targets" refers to all targets being activated simultaneously.
c) Quantification of mean response of the stimulated dendrite (D1) by power and number of targets.
d) Histogram of trial responses of dendritic targets for 1, 2, or 3-dendrite activation (1 vs. 2 targets, $p = 9.22 \times 10^{-6}$, 2 vs. 3 targets, $p = 1.43 \times 10^{-22}$, 1 vs. 3, $p = 2.87 \times 10^{-30}$, Wilcoxon rank sum test). Dashed lines denote median response for the indicated distribution (n = 3 dendrites, 1 neuron, 1 mouse).
e) ChRmine-activated response of a single dendritic ROI at increasing powers and target numbers, disaggregated by blocks. (* $p < 0.05$, ** $p < 0.01$, *** $p < 0.001$. Mean responses are in $\Delta F/F_0$.)

Interestingly, as we stimulated the dendrites with increasingly higher powers, the baseline fluorescence of all recorded dendrites also increased (**Fig. 8b**). For example, delivering 12 mW/target in the first block (lowest powers) evoked a much greater change in dendritic response than when 12 mW/target was delivered in the third block (highest powers). This discrepancy points to a potential caveat in our dendritic photostimulation approach, whereby repeatedly stimulating a dendritic target for extended periods may lead to long-lasting (even permanent) changes in baseline activity—potentially by desensitizing the opsin or by damaging the cell. By dampening the observed change in activity at similar power levels across blocks, this altered baseline fluorescence precludes any comparison of dendritic response across powers from different blocks. Future experiments could control for the changes in dendritic fluorescence by instating "break" periods between experimental blocks or creating a "standard" power level with which the dendrite is stimulated in each block. All recorded responses could then be compared to the "standard activation" of the dendrite and scaled accordingly. Additionally, any further analysis in this thesis will involve a comparison within, rather than between, blocks of different power sets. Quantifying the correlation between the number of targets, power delivered per target, and dendritic response in this way reveals a positive trend between power delivered and mean response at each dendritic ROI (**Fig. 8e;** see also **Supplementary Fig. 6b, Supplementary Fig. 7b**).

Next, we examined the activation of non-stimulated dendrites and the soma during the multi-target stimulation experiments (**Fig. 9a**). Similar to the stimulated dendritic response, we found a significant positive trend between the number of targets simultaneously stimulated and the response recorded in non-stimulated dendrites (**Fig. 9b;** n = 3 dendrites, 1 vs. 2 targets, $p = 1.07 \times 10^{-11}$, 2 vs. 3 targets, $p = 4.30 \times 10^{-26}$, 1 vs. 3 targets, $p = 1.62 \times 10^{-44}$, Wilcoxon rank sum test) and soma (**Fig. 9c;** 1 vs. 2 targets, $p = 8.50 \times 10^{-5}$, 2 vs. 3 targets, $p = 3.01 \times 10^{-11}$, 1 vs. 3 targets, $p = 4.96 \times 10^{-17}$, Wilcoxon rank sum test). Accordingly, within power sets, the responses of non-stimulated dendrites (**Fig. 9d-e**) and soma (**Fig. 9f-g**) were significantly higher when more dendritic targets were simultaneously activated, although the evoked responses in non-stimulated dendrites were much lower compared to both somatic and stimulated dendrite activation at similar powers. Linear regression models relating power per target to response revealed positive trends between stimulation power and measured response at stimulated dendrites (**Fig. 10a**), non-stimulated dendrites (**Fig. 10b**), and soma (**Fig. 10c,** n = 1 neuron).

Part 4. Dendritic Arithmetic

Power-multiplied somatic activation by individual dendrites

We next sought to characterize the “rules” by which dendrites integrate and transmit information arriving at the synapse. First, we investigated how scaling the photostimulation power delivered to dendritic targets affects the somatic response (**Fig. 11a**). Each experimental block was designed such that the second and third powers in each block were double and triple the first power, respectively. We hypothesized that scaling photostimulation powers delivered to the dendritic target would linearly increase the observed somatic response. For each block, we thus computed a “theoretical” somatic response for the doubled and tripled powers by scaling the post-stimulation somatic response of the first, “baseline” power accordingly after correcting for baseline fluorescence for each trace (see **Methods**). For each condition, we then compared the theoretical linear response with the empirically recorded response at the soma (**Fig. 11c,** see also **Supplementary Fig. 8;** n = 10 trials per condition, 1 dendrite) to determine whether scaling the photostimulation power leads to linear scaling of the somatic response. The results showed a supralinear increase in somatic activation when powers were doubled or tripled, indicating a nonlinear relationship between dendritic stimulation power and somatic output (**Fig. 11b, Supplementary Fig. 9**; n = 3 dendrites, 1 neuron, 1 animal, p = 0.0182, Wilcoxon signed-rank test). To determine whether *dendritic* responses scaled linearly with power, we performed

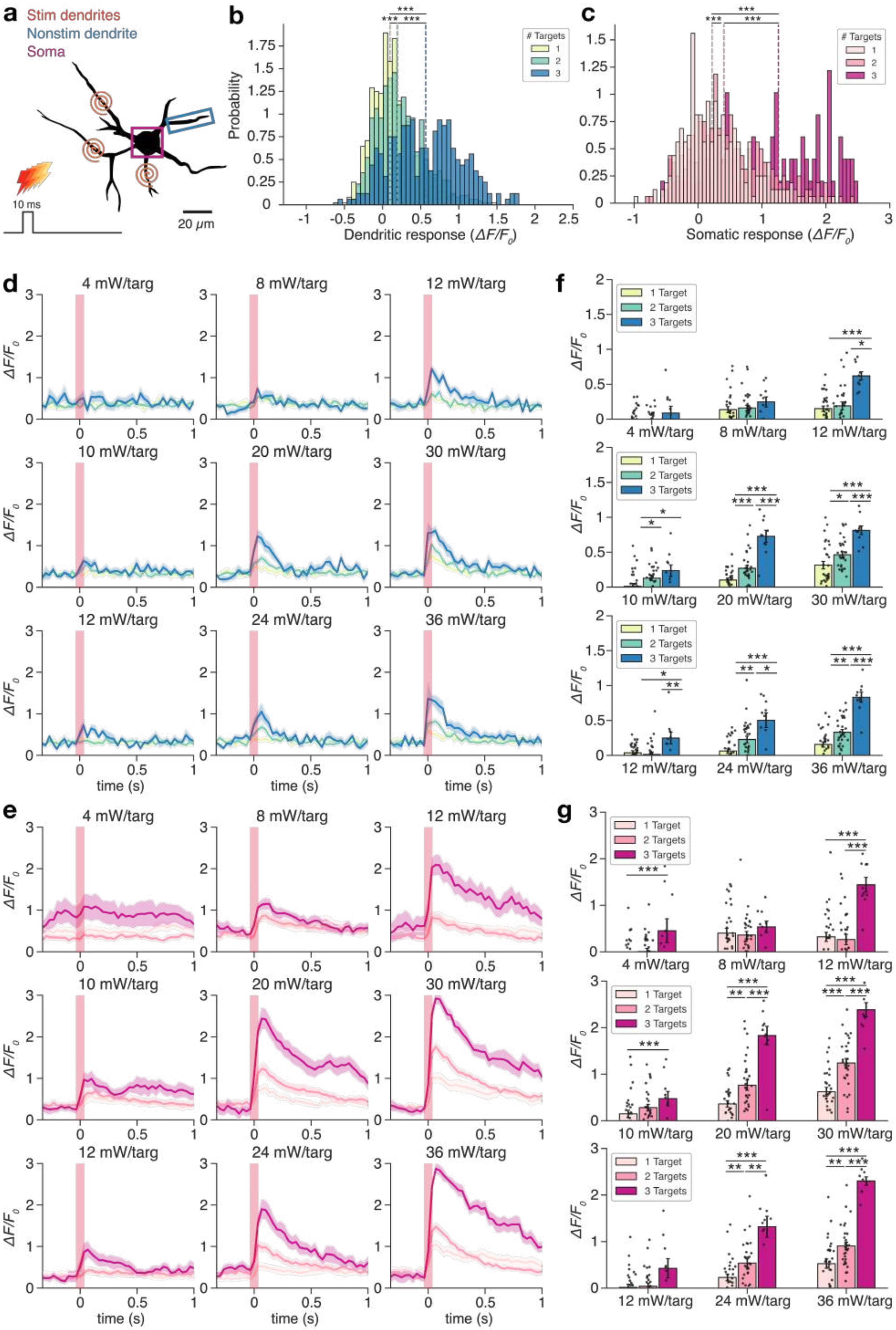
a
Stim dendrites
Nonstim dendrite
Soma
10 ms
20 μm
b
Probability
Dendritic response (ΔF/F0)
Targets
1
2
3
***
*** ***
c
Somatic response (ΔF/F0)
Targets
1
2
3
***
*** ***
d
4 mW/targ
8 mW/targ
12 mW/targ
10 mW/targ
20 mW/targ
30 mW/targ
12 mW/targ
24 mW/targ
36 mW/targ
ΔF/F0
time (s)
e
4 mW/targ
8 mW/targ
12 mW/targ
10 mW/targ
20 mW/targ
30 mW/targ
12 mW/targ
24 mW/targ
36 mW/targ
ΔF/F0
time (s)
f
1 Target
2 Targets
3 Targets
ΔF/F0
4 mW/targ
8 mW/targ
12 mW/targ
10 mW/targ
20 mW/targ
30 mW/targ
12 mW/targ
24 mW/targ
36 mW/targ
g
1 Target
2 Targets
3 Targets
ΔF/F0
4 mW/targ
8 mW/targ
12 mW/targ
10 mW/targ
20 mW/targ
30 mW/targ
12 mW/targ
24 mW/targ
36 mW/targ

Figure 9. Response of non-stimulated dendrites and soma.
a) Schematic of recorded responses from the experiment outlined in **Figure 8a**. Activation of non-stimulated dendrites (blue) and soma (magenta) was measured during and after stimulation of on-target dendrites.
b) Trial responses of non-stimulated dendrites when one, two, or three stimulated dendrites were simultaneously activated (1 vs. 2 targets, $p = 1.07 \times 10^{-11}$, 2 vs. 3 targets, $p = 4.30 \times 10^{-26}$, 1 vs. 3 targets, $p = 1.62 \times 10^{-44}$, Wilcoxon rank sum test). Dashed lines denote median response for the indicated distribution (n = 3 dendrites, 1 neuron).
c) Trial responses of the soma when 1, 2, or 3 dendrites were simultaneously activated (1 vs. 2 targets, $p = 8.50 \times 10^{-5}$, 2 vs. 3 targets, $p = 3.01 \times 10^{-11}$, 1 vs. 3 targets, $p = 4.96 \times 10^{-17}$, Wilcoxon rank sum test). Dashed lines denote median response for the indicated distribution.
d-e) Photostimulation-triggered averages for a non-stimulated dendrite (n = 3 dendrites) (d) or soma (e) at increasing powers and numbers of stimulated dendritic targets.
f-g) Quantification of mean responses of a non-stimulated dendrite (f) or soma (g) by power and number of stimulated dendritic targets. (* $p < 0.05$, ** $p < 0.01$, *** $p < 0.001$. Mean responses are in $\Delta F/F_0$.)

a similar analysis for each stimulated dendritic ROI and also found a significant supralinear scaling of dendritic response (**Fig. 11d,** n = 3 dendrites, 1 neuron, p = 0.000107, Wilcoxon signed-rank test).

Characterization of inter-dendritic summation

Finally, we probed the characteristics of dendritic integration during multiple-target activation (**Fig. 12a**) to determine how these responses summate. For each combination of powers and dendritic targets, the measured somatic response evoked by simultaneous dendritic target photostimulation was compared to the theoretical responses obtained by summing the somatic response to stimulation of each dendrite alone (example in **Fig. 12b;** see also **Methods, Supplementary Fig. 10**). Overall, we found that the response at the soma summed linearly (**Fig. 12c-d,** n = 1 neuron, p = 0.668, Wilcoxon signed-rank test). Interestingly, while we observed similar linear summation in dendritic responses overall (**Fig. 12e-g,** $p > 0.05$, Wilcoxon signed-rank test), we found supralinear summation when all three dendritic targets were simultaneously stimulated (**Fig. 12g,** p = 0.00186, Wilcoxon signed-rank test), compared to sublinear summation of dendritic responses when two dendritic targets were simultaneously stimulated (**Fig. 12g,** p = 0.00364, Wilcoxon signed-rank test).

Together, these results offer a new strategy for studying dendritic integration via *in vivo* dendritic photostimulation. Future experiments may further develop this approach by establishing an appropriate regime for dendritic stimulation and recording of somatic response, where stimulating dendritic targets can reliably drive somatic response without saturating the GCaMP signals.

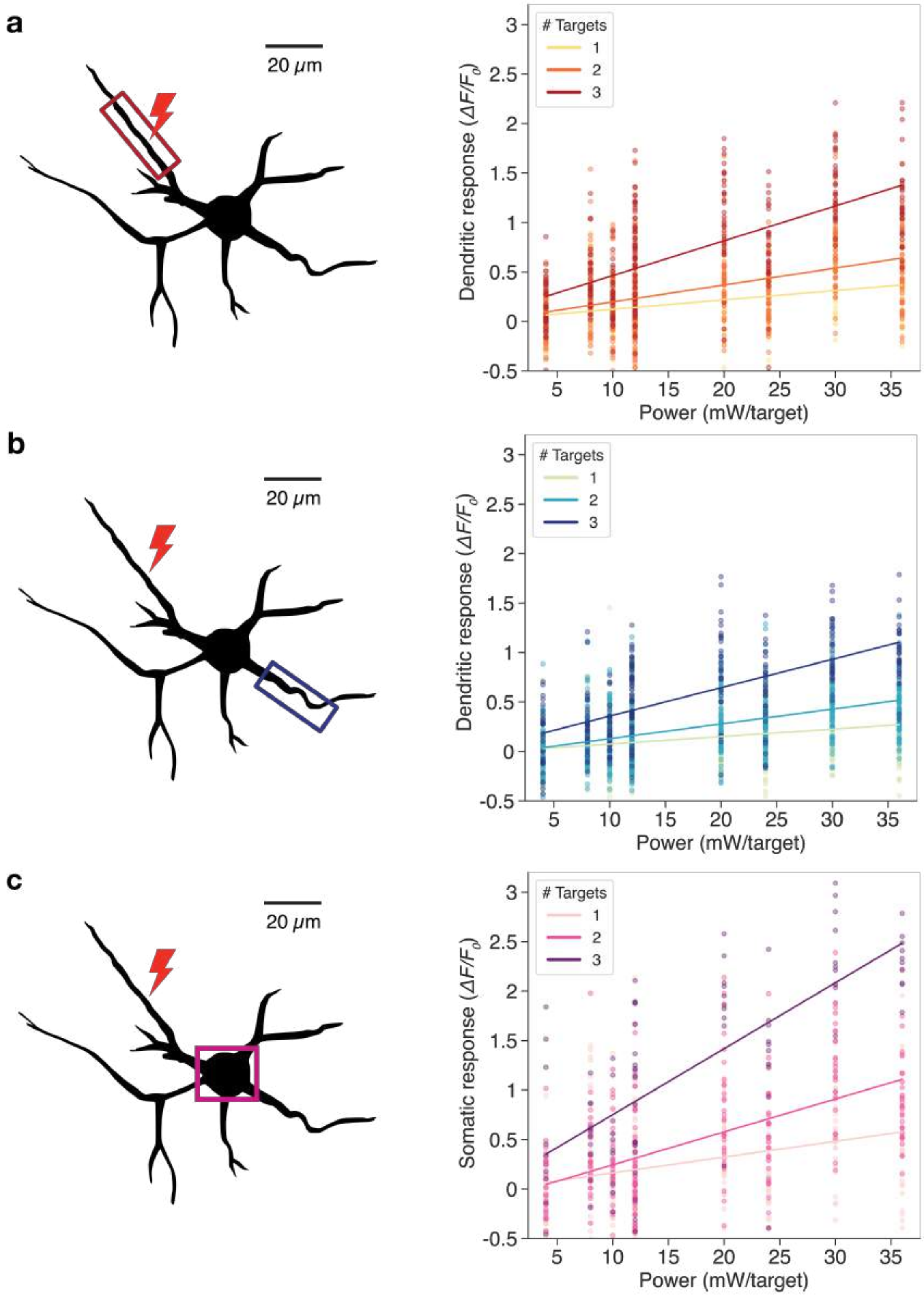

Figure 10. Input-output (IO) curves for targets, non-stimulated dendrites, and soma.

a) Schematic of relative stimulation and recording sites (left) and predicted input-output curve (right) for stimulated dendrites, fitted with simple linear regression using single-trial responses of stimulated dendrites across powers. Colors indicate the number of targets simultaneously activated (n = 3 dendrites).

b) Schematic of relative stimulation and recording sites (left) and predicted input-output curve (right) for non-stimulated dendrites, fitted with simple linear regression using single-trial responses of non-stimulated dendrites across powers. Colors indicate the number of targets simultaneously activated (n = 3 dendrites).

c) Schematic of relative stimulation and recording sites (left) and predicted input-output curve (right) for the soma, fitted with simple linear regression using single-trial somatic responses across powers. Colors indicate the number of targets simultaneously activated (n = 1 neuron).

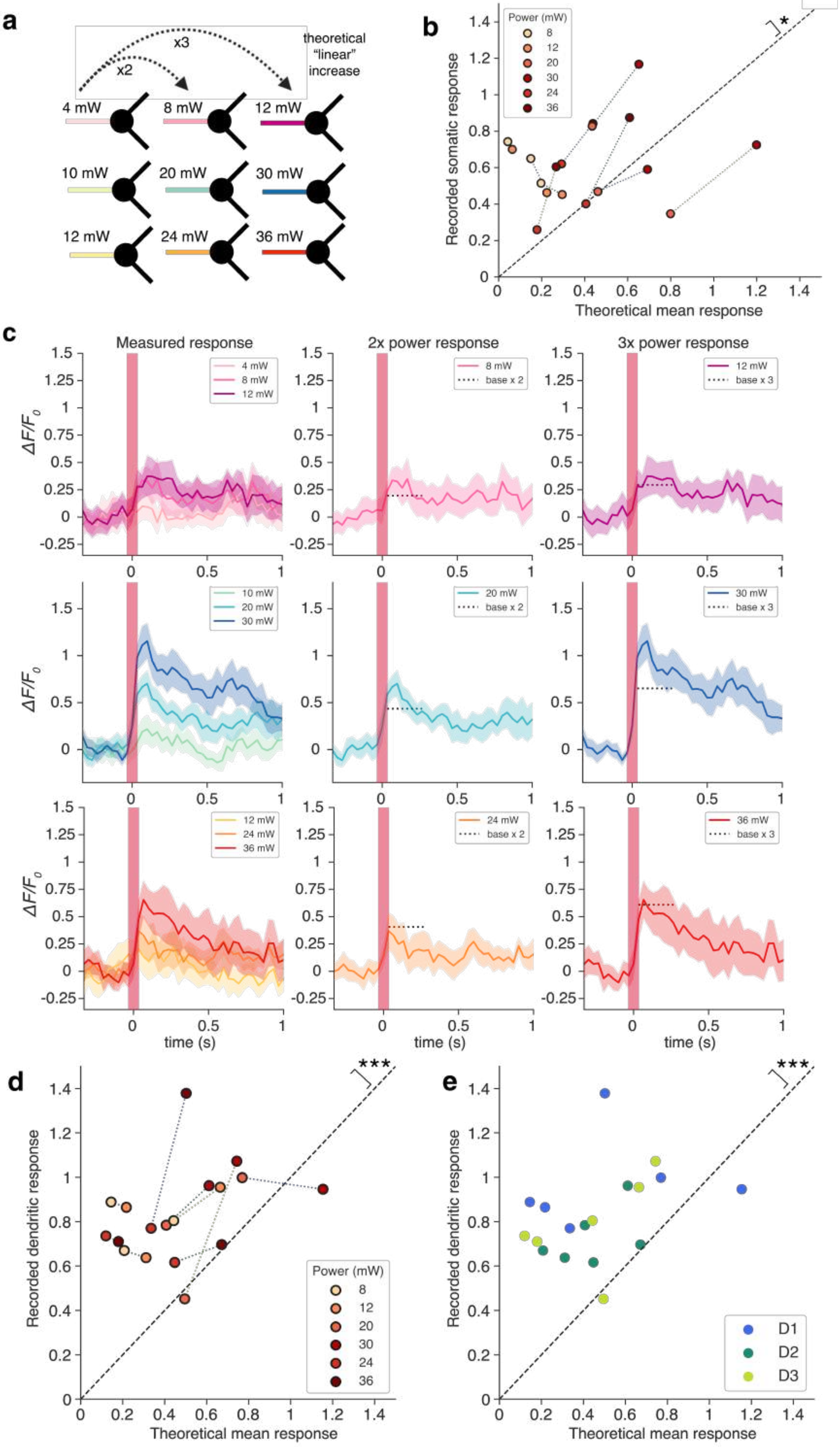
a
x3
x2
theoretical "linear" increase
4 mW
8 mW
12 mW
10 mW
20 mW
30 mW
12 mW
24 mW
36 mW
b
Power (mW)
8
12
20
30
24
36
*
Recorded somatic response
Theoretical mean response
0
0.2
0.4
0.6
0.8
1
1.2
1.4
c
Measured response
2x power response
3x power response
ΔF/F0
4 mW
8 mW
12 mW
base x 2
base x 3
10 mW
20 mW
30 mW
12 mW
24 mW
36 mW
1.5
1.25
1
0.75
0.5
0.25
0
-0.25
time (s)
d
***
Recorded dendritic response
Theoretical mean response
Power (mW)
8
12
20
30
24
36
e
***
Recorded dendritic response
Theoretical mean response
D1
D2
D3

Figure 11. Power-scaled dendritic photostimulation.

a) Schematic of experimental analysis. For each block (row), a "theoretical," linear somatic response for the second and third powers was computed by doubling or tripling the activation measured in the "baseline" first power level. This theoretical response was compared with the measured response recorded when the power was doubled or tripled *in vivo*.

b) Theoretical versus empirical photostimulation-evoked somatic responses (n = 3 dendrites, 1 neuron). Responses were calculated by extracting the peak response within five frames post-stimulation for theoretical or empirical (trial-averaged) baseline-subtracted $\Delta F/F_0$ traces ($p = 0.0182$, Wilcoxon signed-rank test).

c) Example baseline-subtracted traces of theoretical peak activation (dotted line) and measured somatic response (colors indicate power) triggered by a single stimulated dendrite at doubled (middle) or tripled powers (right). Rows denote power blocks: Row 1, 4-12 mW; Row 2, 10-30 mW; Row 3, 12-36 mW.

d) Theoretical versus empirical photostimulation-evoked dendritic responses, colored by power (left) and stimulated dendrite (right). Responses were calculated by extracting the peak response within five frames post-stimulation for the theoretical or empirical (trial-averaged) baseline-subtracted $\Delta F/F_0$ traces ($p = 0.000107$, Wilcoxon signed-rank test). (* $p < 0.05$, ** $p < 0.01$, *** $p < 0.001$) (n = 3 dendrites, 1 neuron).

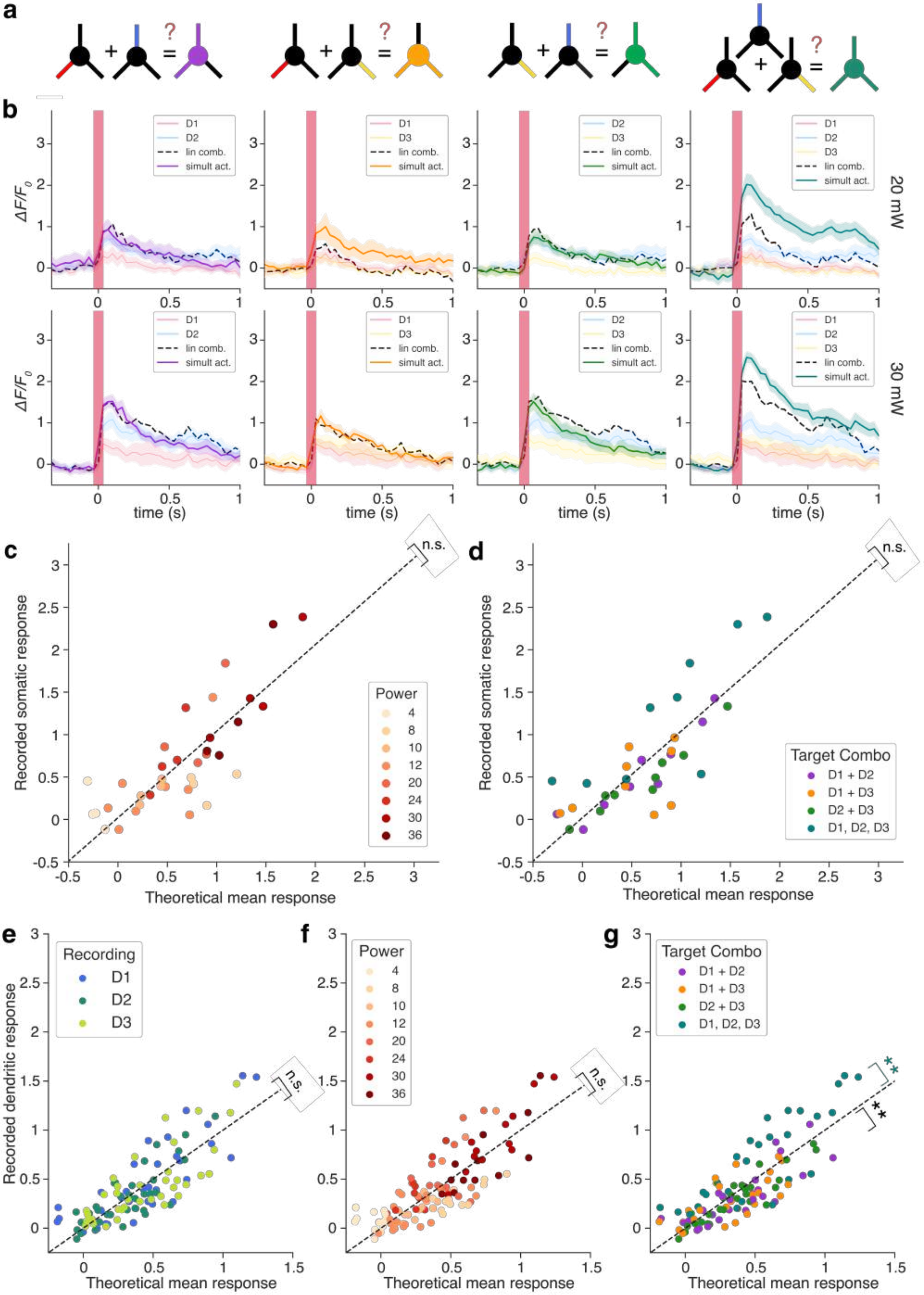
a
+
=
?
b
D1
D2
D3
lin comb.
simult act.
$\Delta F/F_0$
0
1
2
3
0.5
time (s)
20 mW
30 mW
c
Recorded somatic response
Theoretical mean response
Power
4
8
10
12
20
24
30
36
n.s.
d
Target Combo
D1 + D2
D1 + D3
D2 + D3
D1, D2, D3
e
Recording
D1
D2
D3
Recorded dendritic response
f
g
*
*

Figure 12. Characterization of inter-dendritic summation.

a) Schematic of analysis. At each power and for each possible combination of dendritic targets, a “theoretical” linear somatic response was computed by summing the baseline-subtracted somatic responses induced by each individual dendrite stimulation. This hypothetical response was then compared to the baseline-subtracted somatic response during simultaneous activation of multiple dendritic targets.

b) Example somatic $\Delta F/F_0$ traces at 20 mW (top row) and 30 mW (bottom row) for each combination of two or three dendrites. Lin comb., linear combination. simult act., simultaneous activation.

c-d) Comparison between theoretical and empirical somatic responses following dendritic summation, color-coded by power (c) and target combination (d). ($p = 0.668$, Wilcoxon signed-rank test).

e-g) Comparison between theoretical and empirical dendritic responses following dendritic summation, color-coded by recording site (e), power (f), and target combination (g). Note that overall responses were linear; however, two-target combinations summated sub-linearly (g, black significance bar, $p = 0.00364$, Wilcoxon signed rank test), while three-target combinations summated supra-linearly (teal significance bar, $p = 0.00186$, Wilcoxon signed rank test).

(All mean responses are in units of $\Delta F/F_0$, or magnitude of fluorescence change from baseline. n = 3 dendrites, 1 neuron, 1 mouse)

Discussion

In this study, we investigated the dynamics of dendritic computation and information transfer using *in vivo* dendritic optogenetics. We optimized a system for targeted single- and multi-dendritic photostimulation, with simultaneous two-photon calcium imaging at single-cell resolution. Our experiments and subsequent analysis serve as a preliminary proof-of-principle for targeted activation of individual dendrites and separation of local and global neuronal responses. These findings provide insights into the activation and propagation of signals in cortical dendrites, as well as a springboard for probing the link between dendritic integration and behavior in awake, head-fixed mice.

Dissecting components of dendritic activation via single-target photostimulation

Adapting previously described workflows (Russell et al., 2022), we recalibrated an existing all-optical toolbox to perform targeted holographic optogenetics at finer spatial resolutions (calibrated at 385 x 385 µm FOV). Our single-target dendritic photostimulation experiments demonstrated stimulation intensity-dependent calcium signals in the activated dendritic targets. Increasing stimulation intensity resulted in a corresponding increase in the measured response in the stimulated dendrite. We also observed concomitant increases in calcium activity at the soma and in non-stimulated dendrites, suggesting a large role of backpropagating action potentials in mediating global dendritic responses.

Next, we investigated the distribution of dendritic activation along a single dendritic shaft by analyzing the responses along the dendritic ROI before, during, and after photostimulation. Our results revealed a widespread increase in calcium along the dendritic shaft, rather than a gradual spread of localized activation outward from the target center. This finding, along with the strong correlation between responses recorded at stimulated dendrites, non-stimulated dendrites, and the soma, provides further evidence for the predominant contribution of backpropagation to dendritic activation. These findings are consistent with previous studies that have implicated backpropagation in Layer 2/3 dendritic computation in mammalian sensory cortex (Waters et al., 2003; Waters & Helmchen, 2004; Wong-

Campos et al., 2023), serving as a mechanism for integrating feedforward sensory input to basal dendrites and associative input to Layer 1 (Larkum, 2013).

To probe the dynamics of backpropagation-mediated dendritic activation, we examined the relationship between soma-target distance and mean response in stimulated and non-stimulated dendrites. We found a distance-dependent activation of dendritic targets that correlated positively with power intensity and negatively with soma-target distance. This aligns with established findings that backpropagating action potentials traveling further away from the soma experience higher levels of attenuation (Scott et al., 2007; Williams & Stuart, 2000a), as well as previous work showing that spike/plateau amplitudes in the soma of cortical pyramidal neurons decrease significantly from proximal to distal input sites of basal dendrites (Major et al., 2008; Schiller et al., 1997; Stuart et al., 1997; Stuart & Sakmann, 1994; Waters et al., 2005). Accordingly, dendritic ROIs closer to the soma had the largest measured responses, while dendritic ROIs further from the soma displayed smaller responses.

Our results provide further evidence for the dominant contribution of bAP-evoked signals in the calcium dynamics in pyramidal neuron basal dendrites. This is consistent with previous studies that examined the role of bAPs in driving calcium influx in L2/3 pyramidal cells (Landau et al., 2022; Larkum et al., 2007; Waters & Helmchen, 2004), as well as studies that observed that a large component of dendritic calcium signals found in Layer 5 pyramidal neurons are due to bAPs (Beaulieu-Laroche et al., 2019; Francioni et al., 2019). While we did not find obvious local activation at dendritic targets, we found some evidence of local dendritic response when analytically comparing calcium signals across photostimulation trials and targets. To evaluate this further, we developed an analytical approach for estimating the local component of photostimulation-evoked dendritic activation. By matching trials with similar somatic responses across different dendritic targets, we estimated the local component of observed dendritic activation by controlling for the effect of bAPs. This analysis allowed us to gauge the relative proportion of *in vivo* dendritic activation due to local activation versus global backpropagation. Though few experiments have directly quantified the proportions of cortical dendritic activation due to local activation versus backpropagating action potentials, prior studies have conducted similar experiments to disentangle AP-evoked dendritic calcium influx from synaptic activity in apical and dendritic tuft branches in brain slices and *in vivo* (Waters & Helmchen, 2004). While we were able to find a local component of dendritic activation using the matched distribution analysis, future experiments with increased trial numbers should provide a more robust estimation of local dendritic response.

Overall, we found a distance-dependent relationship between dendritic stimulation and somatic (and dendritic) response that was likely mediated by backpropagation of action potentials. The dependence of somatic activation on the distance of dendritic stimulation is consistent with previous studies (Stuart & Sakmann, 1994; Waters et al., 2005). The estimated local component of dendritic calcium influx is likely superimposed on the effects of backpropagation, and future experiments to dissect their respective contributions to observed responses *in vivo* will require carefully controlled conditions. As our stimulation targets across dendrites vary in distance from the soma, we do not have sufficient data to accurately distill the local component of activation while controlling for both dendritic target and soma-target distance. One consideration for future experiments would be to stimulate different points along a single dendritic target or equalize the distance between the stimulated target and the soma for all dendrites.

Another potential drawback in our approach is the inability of GCaMP8s to resolve subthreshold responses within single dendrites. For low stimulation intensities (below 24 mW), we were unable to distinguish between different dendritic responses at varying distances from the soma. At the other extreme, laser powers above 40 mW appeared to irreversibly damage the cell. Furthermore, within the trials used for our distance-dependence analysis (24-40 mW), few dendrites reliably activated the soma, undermining our ability to robustly establish what fraction of the dendritic calcium signal was due to direct local stimulation. Beyond suboptimal expression levels, one explanation for this lies in the GCaMP expression levels and relative fluorescence of the dendrites and soma. At sufficient expression levels to resolve fluctuating dendritic activity at baseline, the somatic response saturates, hindering our ability to resolve healthy somatic responses. In addition to further optimizing the relative levels of calcium indicator and opsin for healthy, ultrasparse expression, future implementations of this technique could include a baseline protocol for characterizing the input-output relationship of single dendrites, as has been done using patch-clamp recordings in slice preparations

(Larkum et al., 2007; Ledergerber & Larkum, 2010; Nevian & Sakmann, 2006; Palmer et al., 2014; Smith et al., 2013). This would involve more finely titrating the power delivered to each dendrite, and cross-validating dendritic activation across different targets. Once established, similar single-target photostimulation experiments would provide a more precise understanding of the relative importance of local and global mechanisms of dendritic activation during *in vivo* signal transmission.

Probing dendritic integration via simultaneous multi-target activation

By randomizing combinations of up to three dendritic targets per neuron, we quantified the mean response for single-, double-, and triple-target activation for increasing photostimulation power sets. We observed a positive trend between the number of targets simultaneously activated and the mean dendritic response for most photostimulation powers. This finding suggests that the activation of multiple dendritic targets can lead to increased overall *dendritic* responses, which may result from increased backpropagation from the soma as a result of multi-target stimulation. This finding is consistent with previous work demonstrating that simultaneous activation of multiple dendrites across different branches of a CA1 pyramidal neuron leads to relatively linear increases in recorded EPSPs (Yang et al., 2014), which may be implicated in the storage of complex features of synaptic input, such as their spatiotemporal correlation. Furthermore, we found a significant positive trend between the number of targets simultaneously activated and the responses recorded in non-stimulated components of the neuron, including non-targeted dendrites and the soma. This lends further support to the potential role of backpropagating action potentials in increased dendritic response during the activation of multiple targets, as these signals spread globally to both stimulated and non-stimulated dendrites.

We also explored how scaling the photostimulation power delivered to each dendritic target affects the somatic response. For single-target trials, we compared the baseline somatic or dendritic activation (i.e., 10 mW photostimulation) with the change in activity at double (20 mW) or triple (30 mW) the baseline power for each experimental block. Our results revealed a supralinear increase in both somatic and dendritic activation when powers were doubled or tripled, indicating a nonlinear relationship between dendritic stimulation power and somatodendritic output *in* *vivo.* This finding implies that the integration and transmission of information in dendrites may be subject to complex nonlinear processes. It is crucial to note, however, that as these are not direct electrophysiological readouts for somatic responses — and rather rely on indirect GCaMP signals that scale nonlinearly with calcium activity (Zhang et al., 2021) — we cannot definitively conclude that the observed supralinear relationship between dendritic input and somatic output at varying powers or multiple target activation is solely due to electrical integrative processes. Future studies could validate these results using more direct measurements of somatic output, such as pairing targeted optical stimulation at the dendrite with *in vivo* patch clamping, or by using genetically-encoded voltage sensor readout at both dendrites and soma (Tao et al., 2015; Wang et al., 2015; Wong-Campos et al., 2023).

Lastly, we sought to characterize the features of dendritic integration during simultaneous activation of multiple targets. Overall, we observed linear summation of dendritic inputs at the soma, which is consistent with seminal studies in brain slices showing that inputs onto separate dendritic branches exhibit roughly linear summation (Polsky et al., 2004; Spruston & Kath, 2004). However, when recording from individual dendrites, we found supralinear summation when three targets were simultaneously activated, compared to sublinear summation when any combination of two targets was simultaneously activated. This could be due to a somatic spiking threshold mechanism activated when all three dendrites were simultaneously targeted.

Technical limitations

The all-optical methodology for single-dendrite activation represents a powerful tool for studying subcellular integration of synaptic input. However, it is worth noting the major caveats of this approach, which also point towards avenues for future improvement. One major limitation of this study lies in the challenge of optimizing the ratio of Cre-dependent opsin (ChRmine) and calcium indicator (GCaMP8s) expression for simultaneous 2P photostimulation and imaging. While the criteria for optimal sparsity were met in terms of the number of cells per ~385 x 385 µm field of view, as well as the avoidance of target dendrite overlap, we were unable to establish an optimal ratio of opsin to indicator. Our ideal working expression levels would exhibit fluctuating GCaMP8s signals at baseline activity levels (920 nm) and sufficient ChRmine expression to drive local dendritic and somatic responses, in addition to the global sparsity levels described above. However, we found that the competition for expression between GCaMP and ChRmine limited the ability to determine an optimal ratio for expression: cells that had sufficient structural ChRmine signal at 765 nm often had dim GCaMP expression; and cells with healthy, non-saturated levels of GCaMP also had very low levels of ChRmine expression. Additionally, the cells in our experimental sample (n = 10 cells in 3 mice) had high GCaMP baseline fluorescence in the soma despite sufficient GCaMP and ChRmine expression in dendritic targets. This compromised the read-write capabilities of our all-optical approach, which represents a fundamental problem for the viral delivery approach for dendritic photoactivation. However, given the large photocurrent and high potency of ChRmine (Chen et al., 2021; Kishi et al., 2022; Marshel et al., 2019), it is possible that dendritic activation can be achieved even with low levels of opsin—negating our inclusion criteria for strong ChRmine-mScarlet signal at 765 nm. Future experiments could also explore alternative methods for viral delivery, such as *in utero* electroporation or single-cell electroporation *in vivo*, to drive expression in specific neuronal populations with higher efficiency and control (Judkewitz et al., 2009; Wong-Campos et al., 2023).

Furthermore, our ability to meaningfully compare power-dependent activation across blocks was limited due to increasing baseline fluorescence levels with increasing power levels. During high-power trial blocks for both single- and multi-target experiments, the dendritic response at identical power levels from earlier blocks decreased, suggesting that the GCaMP brightness prior to stimulation in later blocks was shifted upwards. This change in baseline fluorescence levels could be attributed to several factors, including increased photobleaching or neuronal damage at higher power levels. Previous studies have shown that phenomena such as photobleaching become more pronounced as the photostimulation power increases (Reiff et al., 2005; Zhang et al., 2021) — leading to a subsequent drop in signal-to-noise ratio (SNR), as well as accuracy and reliability of power-dependent activation comparison across blocks. In addition to preventing cross-block comparisons, this effect may undermine the accuracy of our quantified dendritic responses for higher powers: as GCaMP fluorescence saturates, we would observe a plateauing of photostimulation-evoked responses where neuronal or dendritic activity actually continues to increase. This may explain the observed sublinear summation of multiple dendritic inputs at the soma.

To address this limitation, several workarounds could be explored using this all-optical approach without compromising experimental duration. One avenue involves better understanding the temporal dynamics of dendritic GCaMP fluorescence following optical stimulation. In all experiments, we arbitrarily selected an inter-trial interval of 4 s to allow the galvanometer and SLM to update positions, with no extensive wait times between power blocks. Instating longer inter-trial delays or “rest” times between 10-minute recordings would potentially allow neuronal GCaMP expression to return to baseline levels comparable to the first trial block. Furthermore, baseline fluorescence could be examined in real time before each block to scale stimulation-induced responses accordingly. To mitigate the confounding effect of increasing baseline fluorescence, it may also be beneficial to incorporate a systematic variation of power levels both within and across blocks. In other words, rather than successively increasing power levels for each experimental block, randomizing the order of power blocks would mitigate the effects of progressive photodamage or bleaching. Alternatively, both high and low powers could be sampled in each block to account for the dampening of observed response at higher stimulation power levels. This approach would allow for a more comprehensive analysis of power-dependent activation while distinguishing true activation trends from baseline artifacts.

Another component related to baseline fluorescence that affected observed calcium responses was the calculation of ΔF/F. For this dataset, I transformed the raw traces to $(F - F_0)/F_0$, where F_0 was defined as the 10th percentile of a 2 s sliding window. However, due to the high background variability and low SNR of the recordings (cells with lower GCaMP8s expression were selected to balance for sufficient ChRmine expression), the “baseline” fluorescence values were generally positive. In other words, choosing a 10th percentile F_0 did not correspond to the average baseline activity, but rather the *lower* end of these fluctuating baseline fluorescence levels. As a result, the computed ΔF/F at resting (pre-stimulation) periods ranged from 0 to 1, rather than consistently being centered around 0. This likely led to an overestimation of recorded mean calcium responses; therefore, any observed patterns between power or spatiotemporal inputs and somato-dendritic response require a re-evaluation of baseline intensities. In future analyses, greater care will be taken in selecting ΔF/F parameters that accurately reflect how the SNR fluctuates across dendritic recordings. One approach to selecting the F_0 percentile and sliding window length would involve fitting a Gaussian to the overall distribution of raw intensity values per sliding window, and determining whether the fluorescence distribution is skewed in either direction (Peron et al., 2015). This would provide a better estimate of how much the recorded signals deviate from the baseline, thus enabling a more robust selection of F_0.

Moreover, one important consideration is the interpretation of the observed dendritic responses and the role of action potential backpropagation in driving these responses. To adequately study dendritic integration *in vivo*, it is crucial to discern the contribution of local activation to dendritic responses from effects of backpropagation, either by developing a robust method for blocking backpropagating action potentials from the soma, or through analytical methods using controls for dendritic target location and soma-target distance (Kerlin et al., 2019). One experimental approach for isolating local components of dendritic activation could involve the use of more temporally precise voltage indicators paired with rapid scanning microscopes, such as those using acousto-optic deflectors for 2-photon imaging (see ***Future directions***) (Liu et al., 2022; Villette et al., 2019; Wong-Campos et al., 2023).

Lastly, as our approach is not localized to individual synapses but rather segments along a dendritic shaft, our all-optical method may not accurately simulate biological signal input arriving at synaptic spines. We initially opted for the optogenetic approach for studying *in vivo* dendritic integration because it is relatively non-invasive compared to electrophysiological approaches, as well as its ability to finely titrate power levels delivered to the dendritic shaft. However, despite its strengths and ease of access to cortical dendrites, a more “naturalistic” approach would involve direct synaptic activation, such as *in vivo* two-photon glutamate uncaging (Noguchi et al., 2011) or mapping individual connections from presynaptic inputs to drive local dendritic responses (Fişek et al., 2023). It is also worth noting the kinetic differences between synaptically and optogenetically evoked dendritic responses, as the availability of ion channels differs depending on the rate of membrane depolarization. For example, when distributing photostimulation power over a relatively large segment of the dendritic shaft (relatively slow compared to synaptic activation), voltage-gated channels stochastically inactivate over time, rendering the dendrite unavailable for an “active event” (i.e., an action potential or dendritic spikes). Further experiments could explore how optogenetic stimulation parameters (e.g., power, duration, or spatial extent) influence dendritic voltage dynamics and how they differ from the kinetics of synaptically evoked depolarization.

Future directions

In this study, we opened a new frontier in all-optical interrogation and recording *in vivo:* direct manipulation of dendritic activity. To enhance the performance of this technique and extend its applications, several additional areas would be useful to explore. Here I outline two classes of future studies: **(1)** optimization of the dendritic optogenetics workflow, and **(2)** extensions and applications for this tool in studying the link between neural activity and behavior.

Optimization of all-optical dendritic interrogation workflow. To improve the precision and throughput of our all-optical approach, multiple aspects of our all-optical pipeline could be optimized. Firstly, in this study, we were unable to achieve an optimal co-expression ratio between calcium indicator and opsin that maximized the “read-write” capabilities of our tool. To enhance the efficiency of viral transfection while minimizing competition between opsin and indicator, future experiments could screen for viral variants with orthogonal tropism or bicistronic viral constructs expressing both opsins and indicators (Bounds et al., 2022; LaFosse et al., 2023). While bicistronic adeno-associated viruses (AAV) have incorporated jGCaMP8s with ChrimsonR (LaFosse et al., 2023) and GCaMP7s with ChRoME (Bounds et al., 2022), these have only been developed for soma-targeted viral constructs for somatic stimulation. Developing similar constructs for non-soma-targeted opsins with Cre-dependence for ultrasparse expression would ensure co-expression of both indicator and opsin at comparable levels, enabling the readout and write-in of precise dendritic signals during informational processing *in vivo.*

Secondly, optimization of the duration and spatial localization of targeted optical stimulation would dramatically refine the temporal and spatial precision of dendritic activation readout. Our photostimulation duration (10 ms) was selected based on comparable studies employing targeted 2P holographic photostimulation

(Marshel et al., 2019); our inter-trial delay (4 s) was chosen to reasonably maximize the number of trials per experimental block while allowing neuronal activity to return to baseline after stimulation. However, we noticed that with increasing power levels, the baseline fluorescence of dendrites and soma gradually increased, suggesting neuronal damage at higher powers and long stimulation durations. Future experiments could improve the signal-to-noise ratio at higher powers by implementing longer inter-trial delays or intervals between experimental blocks. As increased baseline fluorescence could also signal neuronal damage, lower and more finely titrated power levels could be further investigated. Alternatively, the development of more efficient sensors and opsins would reduce the power levels required to activate and record from dendritic segments, thereby minimizing photodamage to the cell.

Similarly, optimizing the spiral size and shape of photostimulation could improve spatial specificity, minimize off-target activation of neighboring dendrites, and increase the efficiency of power delivery to the cell. While previously described experiments employed an average power of ~6 mW/cell for pyramidal cells in L2/3 of cortex (Russell et al., 2022), our average power delivered per dendritic target ranged from 1 mW to 40 mW, with only the highest powers driving detectable responses in the dendrites and soma. Part of this discrepancy lies in the stimulation pattern: to ensure on-target activation of the dendrite during animal movement, we spiraled over a larger dendritic segment within the 10 ms stimulation interval. In future studies, it would be more efficient to further optimize the shape of the spiral (e.g., elliptically scan over a dendritic segment), examine how spiral duration affects the stimulation efficiency, or identify clusters of synapses before stimulation experiments. Fine-tuning these parameters would enable more precise control over dendritic activation and may bring us closer to mimicking naturalistic inputs to the dendritic arbor.

Lastly, one of the main disadvantages of this technique in its current state is the difficulty of disentangling the effects of backpropagation from local activation components (Kerlin et al., 2019). As described previously, future experimental designs can focus on identifying and accounting for the effects of backpropagation on dendritic activation. In slice recordings, this can be done by carefully assessing the temporal relationship between somatic and dendritic activation: dendritic activity observed before somatic activation represents local activation, while dendritic spikes recorded following somatic activation signify backpropagating action potentials (Williams et al., 2023). As it is difficult to extract temporally precise responses using calcium indicators (which have slow temporal kinetics), one strategy for dissecting backpropagating and local components of dendritic activation *in vivo* would be to implement a faster and more sensitive readout of dendritic activity. For example, the current state-of-the-art chemogenetic voltage indicator Voltron2 has been validated *in vivo* to extract subthreshold ranges of activity in conjunction with Channelrhodopsin-2 (ChR2) stimulation in mouse hippocampus, visual cortex, and motor cortex (Abdelfattah et al., 2023). A recent paper paired Voltron2 with the blue-shifted channelrhodopsin CheRiff to map sub-millisecond voltage dynamics in hippocampal CA1 distal dendrites, successfully characterizing the interplay between backpropagation and dendritic sodium spikes *in vivo* (Wong-Campos et al., 2023). Other recently developed voltage sensors (e.g., JEDI-2P, ASAP3, ASAP4) have been optimized in conjunction with ultrafast local volume excitation (ULoVE) methods for kilohertz-rate two-photon sampling *in vivo* with high stability and sensitivity (Evans et al., 2022; Liu et al., 2022; Villette et al., 2019). JEDI-2P, for example, has been shown to optically record (with 2P microscopy) the voltage dynamics of individual cortical neurons in awake-behaving mice for more than 40 minutes, robustly detecting spikes at brain depths exceeding 400 μm (Liu et al., 2022). Such voltage indicators could also be paired with microscope systems featuring ultra-fast scanning rates, including acousto-optic laser scanning systems for physiologically realistic spatiotemporal patterns of synaptic stimulation and multi-site optical recording of electrical activity at millisecond resolution (Iyer et al., 2006; Liu et al., 2022; Saggau et al., 1998; Salomé et al., 2006).

Potential extensions and applications for this technique

The all-optical approach for *in vivo* dendritic stimulation that I have described in this thesis holds promise for biological applications and extensions beyond the scope of our study. One of the most fundamental and powerful further developments of this technique would be to validate its ability to perform 2P holographic, 3D optogenetic stimulation (or inhibition) of the entire dendritic arbor in conjunction with multiplane imaging at the soma. This advancement would expand our capabilities beyond probing basal dendritic integration to understanding compartmentalized dendritic activity across proximal and distal dendritic arbors. For example, Layer 5 pyramidal neurons in the mouse primary visual cortex are known to receive inputs from higher cortical areas, receiving direct feedback signals and generating local calcium events in their distal apical tuft dendrites to influence somatic activity (Fletcher & Williams, 2019; Williams & Stuart, 2002; Xu et al., 2012). Future experiments may involve characterizing the functional role of dendritic coincidence detection (Larkum, 1999; Stuart & Hausser, 2001) in sensory representation. By pairing apical dendritic tuft photostimulation with somatic activation *in vivo,* such as during an active sensing task (Xu et al., 2012) or visual stimulus presentation (Smith et al., 2013), one could determine whether the specific interaction between dendritic EPSPs and somatic APs influence the tuning strength of neurons to particular sensory stimuli. Being able to perturb (i.e., activate or silence) synapses in apical dendritic tufts and study inter-dendritic summation at proximal sites or the soma during sensory perception would be immensely valuable in understanding how cortico-cortical feedback arriving at distal tufts modulates primary cortical activity and behavior—thus allowing us to unravel the functional properties and computational significance of dendritic compartmentalization (Fişek et al., 2023).

Furthermore, integrating closed-loop feedback systems within the dendritic all-optical system would allow us to manipulate local and global dynamics of dendritic activation, providing insights into their specific role in processing information from higher cortical areas. Previous studies have demonstrated the value of dynamically and precisely controlling neuronal activity patterns in real time to extract causal relationships between neural activity and behavior (Zhang et al., 2018). The ability to simultaneously read out and manipulate activity in neural circuits “on the fly,” guided by online measurements of dendritic activity, would potentially be useful for perturbing precise temporal aspects of dendritic integration and examining their effects on signal processing. Specifically, one exciting avenue for probing sensory integration would be to *inactivate* dendritic signals as they arrive at apical or basal tufts *in vivo*. Optogenetically silencing dendritic inputs during a sensory detection or discrimination task, for example, may offer insights into the causal role of feedforward or feedback dendritic processing on perception and behavior.

Finally, the holy grail of our technique would be to link dendritic integration with functional, network-level activity with animal cognition and behavior—which currently cannot be investigated in *in vitro* slice or *in vivo* electrophysiological recordings. How do variables such as behavioral state (i.e., attention, running, reward) modulate dendritic integration, and subsequently, sensory perception or behavior? Recent papers have characterized the link between sensory-evoked neural responses and behavior at the population level (Russell et al., 2019) or by pairing sensory stimuli with photostimulation of presynaptic neurons (from higher cortical areas) to drive local dendritic activation (Fişek et al., 2023). A logical next step in understanding higher-order feedforward and feedback processing would be to apply all-optical methods to perturb subcellular level signal processing or drive local activations in dendritic tufts during learning and behavior. For example, it has been suggested via computational modeling that figure-ground segregation, the perceptual isolation of objects from their background, occurs through recurrent and feedback connections between primary visual cortex and higher-order visual areas (Poort et al., 2012). To probe the role of cortico-cortical feedback in figure-ground segregation, our technique could be applied with inhibitory opsins to silence apical tufts during a perceptual detection task in which mice are trained to detect figures defined by an orientation that differs from their background at various contrast levels (Schnabel et al., 2018). It would be useful to pair this stimulation with recording of neuronal responses when various features of an image (figure, edge, or background) fall within the receptive field of stimulated neurons, as this would provide additional information about how these feedback inputs modulate the overall activity elicited at the soma. Doing so would bring us substantially closer to understanding the functional significance of dendritic integration in neural perception, particularly regarding interactions between cortical brain regions.

In conclusion, our study provides an important first demonstration of all-optical dendritic interrogation and highlights its potential for understanding the link between dendritic and somatic activity in single neurons *in vivo.* Dendritic integration, as well as the link between cortical processing, perception, and behavior, have all been studied extensively in brain slices and mouse cortex, respectively. However, previous technical limitations have precluded a direct investigation of the link between subcellular dendritic signal integration and perception in awake, behaving mice. Though our approach requires further optimization and appropriate controls for more rigorous and controlled direct dendritic activation *in vivo,* it may serve as an important step toward the goal of unifying our understanding of neural computation across multiple scales.

Bibliography

Abdelfattah, A. S., Zheng, J., Singh, A., Huang, Y.-C., Reep, D., Tsegaye, G., Tsang, A., Arthur, B. J., Rehorova, M., Olson, C. V. L., Shuai, Y., Zhang, L., Fu, T.-M., Milkie, D. E., Moya, M. V., Weber, T. D., Lemire, A. L., Baker, C. A., Falco, N., … Kolb, I. (2023). Sensitivity optimization of a rhodopsin-based fluorescent voltage indicator. *Neuron*, *111*(10), 1547-1563.e9. https://doi.org/10.1016/j.neuron.2023.03.009

Adesnik, H., & Abdeladim, L. (2021). Probing neural codes with two-photon holographic optogenetics. *Nature Neuroscience*, *24*(10), Article 10. https://doi.org/10.1038/s41593-021-00902-9

Ahrens, M. B., Orger, M. B., Robson, D. N., Li, J. M., & Keller, P. J. (2013). Whole-brain functional imaging at cellular resolution using light-sheet microscopy. *Nature Methods*, *10*(5), Article 5. https://doi.org/10.1038/nmeth.2434

Amitai, Y., Friedman, A., Connors, B. W., & Gutnick, M. J. (1993). Regenerative activity in apical dendrites of pyramidal cells in neocortex. *Cerebral Cortex (New York, N.Y.: 1991)*, *3*(1), 26–38. https://doi.org/10.1093/cercor/3.1.26

Ariav, G., Polsky, A., & Schiller, J. (2003). Submillisecond Precision of the Input-Output Transformation Function Mediated by Fast Sodium Dendritic Spikes in Basal Dendrites of CA1 Pyramidal Neurons. *Journal of Neuroscience*, *23*(21), 7750–7758. https://doi.org/10.1523/JNEUROSCI.23-21-07750.2003

Armbruster, B. N., Li, X., Pausch, M. H., Herlitze, S., & Roth, B. L. (2007). Evolving the lock to fit the key to create a family of G protein-coupled receptors potently activated by an inert ligand. *Proceedings of the National Academy of Sciences of the United States of America*, *104*(12), 5163–5168. https://doi.org/10.1073/pnas.0700293104

Ashley, C. C., & Ridgway, E. B. (1968). Simultaneous Recording of Membrane Potential, Calcium Transient and Tension in Single Muscle Fibres. *Nature*, *219*(5159), Article 5159. https://doi.org/10.1038/2191168a0

Baker, P. F., Meves, H., & Ridgway, E. B. (1971). Phasic entry of calcium in response to depolarization of giant axons of Loligo forbesi. *The Journal of Physiology*, *216*(2), 70P-71P.

Beaulieu-Laroche, L., Toloza, E. H. S., Brown, N. J., & Harnett, M. T. (2019). Widespread and Highly Correlated Somato-dendritic Activity in Cortical Layer 5 Neurons. *Neuron*, *103*(2), 235-241.e4. https://doi.org/10.1016/j.neuron.2019.05.014

Beaulieu-Laroche, L., Toloza, E. H. S., Goes, M.-S. van der, Lafourcade, M., Barnagian, D., Williams, Z. M., Eskandar, E. N., Frosch, M. P., Cash, S. S., & Harnett, M. T. (2018). Enhanced Dendritic Compartmentalization in Human Cortical Neurons. *Cell*, *175*(3), 643-651.e14. https://doi.org/10.1016/j.cell.2018.08.045

Bloss, E. B., Cembrowski, M. S., Karsh, B., Colonell, J., Fetter, R. D., & Spruston, N. (2016). Structured Dendritic Inhibition Supports Branch-Selective

Integration in CA1 Pyramidal Cells. *Neuron*, *89*(5), 1016–1030. https://doi.org/10.1016/j.neuron.2016.01.029

Boahen, K. (2022). Dendrocentric learning for synthetic intelligence. *Nature*, *612*(7938), Article 7938. https://doi.org/10.1038/s41586-022-05340-6

Borden, P. M., Zhang, P., Shivange, A. V., Marvin, J. S., Cichon, J., Dan, C., Podgorski, K., Figueiredo, A., Novak, O., Tanimoto, M., Shigetomi, E., Lobas, M. A., Kim, H., Zhu, P. K., Zhang, Y., Zheng, W. S., Fan, C., Wang, G., Xiang, B., … Looger, L. L. (2020). *A fast genetically encoded fluorescent sensor for faithful in vivo acetylcholine detection in mice, fish, worms and flies* (p. 2020.02.07.939504). bioRxiv. https://doi.org/10.1101/2020.02.07.939504

Bounds, H. A., Sadahiro, M., Hendricks, W. D., Gajowa, M., Gopakumar, K., Quintana, D., Tasic, B., Daigle, T. L., Zeng, H., Oldenburg, I. A., & Adesnik, H. (2022). *Ultra-precise all-optical manipulation of neural circuits with multifunctional Cre-dependent transgenic mice* (p. 2021.10.05.463223). bioRxiv. https://doi.org/10.1101/2021.10.05.463223

Boyden, E. S., Zhang, F., Bamberg, E., Nagel, G., & Deisseroth, K. (2005). Millisecond-timescale, genetically targeted optical control of neural activity. *Nature Neuroscience*, *8*(9), Article 9. https://doi.org/10.1038/nn1525

Branco, T., Clark, B. A., & Häusser, M. (2010). Dendritic Discrimination of Temporal Input Sequences in Cortical Neurons. *Science*, *329*(5999), 1671–1675. https://doi.org/10.1126/science.1189664

Branco, T., & Häusser, M. (2010). The single dendritic branch as a fundamental functional unit in the nervous system. *Current Opinion in Neurobiology*, *20*(4), 494–502. https://doi.org/10.1016/j.conb.2010.07.009

Brinks, D., Klein, A. J., & Cohen, A. E. (2015). Two-Photon Lifetime Imaging of Voltage Indicating Proteins as a Probe of Absolute Membrane Voltage. *Biophysical Journal*, *109*(5), 914–921. https://doi.org/10.1016/j.bpj.2015.07.038

Broussard, G. J., Liang, Y., Fridman, M., Unger, E. K., Meng, G., Xiao, X., Ji, N., Petreanu, L., & Tian, L. (2018). In vivo measurement of afferent activity with axon-specific calcium imaging. *Nature Neuroscience*, *21*(9), 1272–1280. https://doi.org/10.1038/s41593-018-0211-4

Campbell, E. J., & Marchant, N. J. (2018). The use of chemogenetics in behavioural neuroscience: Receptor variants, targeting approaches and caveats. *British Journal of Pharmacology*, *175*(7), 994–1003. https://doi.org/10.1111/bph.14146

Carrillo-Reid, L., Yang, W., Bando, Y., Peterka, D. S., & Yuste, R. (2016). Imprinting and recalling cortical ensembles. *Science*, *353*(6300), 691–694. https://doi.org/10.1126/science.aaf7560

Chemla, S., & Chavane, F. (2010). Voltage-sensitive dye imaging: Technique review and models. *Journal of Physiology-Paris*, *104*(1), 40–50. https://doi.org/10.1016/j.jphysparis.2009.11.009

Chen, R., Gore, F., Nguyen, Q.-A., Ramakrishnan, C., Patel, S., Kim, S. H., Raffiee, M., Kim, Y. S., Hsueh, B., Krook-Magnusson, E., Soltesz, I., & Deisseroth,

K. (2021). Deep brain optogenetics without intracranial surgery. *Nature Biotechnology*, *39*(2), Article 2. https://doi.org/10.1038/s41587-020-0679-9

Chen, T.-W., Wardill, T. J., Sun, Y., Pulver, S. R., Renninger, S. L., Baohan, A., Schreiter, E. R., Kerr, R. A., Orger, M. B., Jayaraman, V., Looger, L. L., Svoboda, K., & Kim, D. S. (2013). Ultrasensitive fluorescent proteins for imaging neuronal activity. *Nature*, *499*(7458), Article 7458. https://doi.org/10.1038/nature12354

Chen, X., Leischner, U., Rochefort, N. L., Nelken, I., & Konnerth, A. (2011). Functional mapping of single spines in cortical neurons in vivo. *Nature*, *475*(7357), 501–505. https://doi.org/10.1038/nature10193

Chettih, S. N., & Harvey, C. D. (2019). Single-neuron perturbations reveal feature-specific competition in V1. *Nature*, *567*(7748), Article 7748. https://doi.org/10.1038/s41586-019-0997-6

Chow, B. Y., Han, X., Dobry, A. S., Qian, X., Chuong, A. S., Li, M., Henninger, M. A., Belfort, G. M., Lin, Y., Monahan, P. E., & Boyden, E. S. (2010). High-Performance Genetically Targetable Optical Neural Silencing via Light-Driven Proton Pumps. *Nature*, *463*(7277), 98–102. https://doi.org/10.1038/nature08652

Chuong, A. S., Miri, M. L., Busskamp, V., Matthews, G. A. C., Acker, L. C., Sørensen, A. T., Young, A., Klapoetke, N. C., Henninger, M. A., Kodandaramaiah, S. B., Ogawa, M., Ramanlal, S. B., Bandler, R. C., Allen, B. D., Forest, C. R., Chow, B. Y., Han, X., Lin, Y., Tye, K. M., … Boyden, E. S. (2014). Noninvasive optical inhibition with a red-shifted microbial rhodopsin. *Nature Neuroscience*, *17*(8), 1123–1129. https://doi.org/10.1038/nn.3752

Dana, H., Mohar, B., Sun, Y., Narayan, S., Gordus, A., Hasseman, J. P., Tsegaye, G., Holt, G. T., Hu, A., Walpita, D., Patel, R., Macklin, J. J., Bargmann, C. I., Ahrens, M. B., Schreiter, E. R., Jayaraman, V., Looger, L. L., Svoboda, K., & Kim, D. S. (2016). Sensitive red protein calcium indicators for imaging neural activity. *ELife*, *5*, e12727. https://doi.org/10.7554/eLife.12727

Davie, J. T., Kole, M. H. P., Letzkus, J. J., Rancz, E. A., Spruston, N., Stuart, G. J., & Häusser, M. (2006). Dendritic patch-clamp recording. *Nature Protocols*, *1*(3), Article 3. https://doi.org/10.1038/nprot.2006.164

Deisseroth, K. (2015). Optogenetics: 10 years of microbial opsins in neuroscience. *Nature Neuroscience*, *18*(9), Article 9. https://doi.org/10.1038/nn.4091

Diamond, J. S. (2005). Deriving the glutamate clearance time course from transporter currents in CA1 hippocampal astrocytes: Transmitter uptake gets faster during development. *The Journal of Neuroscience: The Official Journal of the Society for Neuroscience*, *25*(11), 2906–2916. https://doi.org/10.1523/JNEUROSCI.5125-04.2005

Doron, G., Shin, J. N., Takahashi, N., Drüke, M., Bocklisch, C., Skenderi, S., de Mont, L., Toumazou, M., Ledderose, J., Brecht, M., Naud, R., & Larkum, M. E. (2020). Perirhinal input to neocortical layer 1 controls learning. *Science*, *370*(6523), eaaz3136. https://doi.org/10.1126/science.aaz3136

Emiliani, V., Cohen, A. E., Deisseroth, K., & Häusser, M. (2015). All-Optical Interrogation of Neural Circuits. *Journal of Neuroscience*, *35*(41), 13917–13926. https://doi.org/10.1523/JNEUROSCI.2916-15.2015

Euler, T., Detwiler, P. B., & Denk, W. (2002). Directionally selective calcium signals in dendrites of starburst amacrine cells. *Nature*, *418*(6900), Article 6900. https://doi.org/10.1038/nature00931

Evans, S. W., Shi, D., Chavarha, M., Plitt, M. H., Taxidis, J., Madruga, B., Keulen, S. C. van, Pang, M. M., Su, S., Hwang, F.-J., Zhang, G., Reese, A., Pradhan, L., Fan, J. L., Lee, S., Liu, Y., Suomivuori, C.-M., Jiang, D., Negrean, A., … Lin, M. Z. (2022). *A positively Tuned Voltage Indicator Reveals Electrical Correlates of Calcium Activity in the Brain* (p. 2021.10.21.465345). bioRxiv. https://doi.org/10.1101/2021.10.21.465345

Fişek, M., Herrmann, D., Egea-Weiss, A., Cloves, M., Bauer, L., Lee, T.-Y., Russell, L. E., & Häusser, M. (2023). Cortico-cortical feedback engages active dendrites in visual cortex. *Nature*, 1–8. https://doi.org/10.1038/s41586-023-06007-6

Fishell, G., & Rudy, B. (2011). Mechanisms of inhibition within the telencephalon: “where the wild things are.” *Annual Review of Neuroscience*, *34*, 535–567. https://doi.org/10.1146/annurev-neuro-061010-113717

Fletcher, L. N., & Williams, S. R. (2019). Neocortical Topology Governs the Dendritic Integrative Capacity of Layer 5 Pyramidal Neurons. *Neuron*, *101*(1), 76-90.e4. https://doi.org/10.1016/j.neuron.2018.10.048

Forli, A., Vecchia, D., Binini, N., Succol, F., Bovetti, S., Moretti, C., Nespoli, F., Mahn, M., Baker, C. A., Bolton, M. M., Yizhar, O., & Fellin, T. (2018). Two-Photon Bidirectional Control and Imaging of Neuronal Excitability with High Spatial Resolution In Vivo. *Cell Reports*, *22*(11), 3087–3098. https://doi.org/10.1016/j.celrep.2018.02.063

Francioni, V., Padamsey, Z., & Rochefort, N. L. (2019). High and asymmetric somato-dendritic coupling of V1 layer 5 neurons independent of visual stimulation and locomotion. *ELife*, *8*, e49145. https://doi.org/10.7554/eLife.49145

Gillon, C. J., Lecoq, J. A., Pina, J. E., Ahmed, R., Billeh, Y. N., Caldejon, S., Groblewski, P., Henley, T. M., Kato, I., Lee, E., Luviano, J., Mace, K., Nayan, C., Nguyen, T. V., North, K., Perkins, J., Seid, S., Valley, M. T., Williford, A., … Richards, B. A. (2023). Responses of pyramidal cell somata and apical dendrites in mouse visual cortex over multiple days. *Scientific Data*, *10*(1), Article 1. https://doi.org/10.1038/s41597-023-02214-y

Goetz, L., Roth, A., & Häusser, M. (2021). Active dendrites enable strong but sparse inputs to determine orientation selectivity. *Proceedings of the National Academy of Sciences*, *118*(30), e2017339118. https://doi.org/10.1073/pnas.2017339118

Goldey, G. J., Roumis, D. K., Glickfeld, L. L., Kerlin, A. M., Reid, R. C., Bonin, V., Schafer, D. P., & Andermann, M. L. (2014). Removable cranial windows for long-term imaging in awake mice. *Nature Protocols*, *9*(11), Article 11. https://doi.org/10.1038/nprot.2014.165

Gong, Y., Huang, C., Li, J. Z., Grewe, B. F., Zhang, Y., Eismann, S., & Schnitzer, M. J. (2015). High-speed recording of neural spikes in awake mice and flies with a fluorescent voltage sensor. *Science*, *350*(6266), 1361–1366. https://doi.org/10.1126/science.aab0810

Gradinaru, V., Zhang, F., Ramakrishnan, C., Mattis, J., Prakash, R., Diester, I., Goshen, I., Thompson, K. R., & Deisseroth, K. (2010). Molecular and cellular approaches for diversifying and extending optogenetics. *Cell*, *141*(1), 154–165. https://doi.org/10.1016/j.cell.2010.02.037

Grienberger, C., Chen, X., & Konnerth, A. (2014). NMDA receptor-dependent multidendrite Ca(2+) spikes required for hippocampal burst firing in vivo. *Neuron*, *81*(6), 1274–1281. https://doi.org/10.1016/j.neuron.2014.01.014

Grienberger, C., Chen, X., & Konnerth, A. (2015). Dendritic function in vivo. *Trends in Neurosciences*, *38*(1), 45–54. https://doi.org/10.1016/j.tins.2014.11.002

Grienberger, C., & Konnerth, A. (2012). Imaging Calcium in Neurons. *Neuron*, *73*(5), 862–885. https://doi.org/10.1016/j.neuron.2012.02.011

Grynkiewicz, G., Poenie, M., & Tsien, R. Y. (1985). A new generation of Ca2+ indicators with greatly improved fluorescence properties. *The Journal of Biological Chemistry*, *260*(6), 3440–3450.

Guerguiev, J., Lillicrap, T. P., & Richards, B. A. (2017). Towards deep learning with segregated dendrites. *ELife*, *6*, e22901. https://doi.org/10.7554/eLife.22901

Hagner, M. (2012). The electrical excitability of the brain: Toward the emergence of an experiment. *Journal of the History of the Neurosciences*, *21*(3), 237–249. https://doi.org/10.1080/0964704X.2011.595634

Häusser, M. (2021). Optogenetics—The Might of Light. *New England Journal of Medicine*, *385*(17), 1623–1626. https://doi.org/10.1056/NEJMcibr2111915

Häusser, M., Spruston, N., & Stuart, G. J. (2000). Diversity and Dynamics of Dendritic Signaling. *Science*, *290*(5492), 739–744. https://doi.org/10.1126/science.290.5492.739

Higley, M. J., & Sabatini, B. L. (2008). Calcium signaling in dendrites and spines: Practical and functional considerations. *Neuron*, *59*(6), 902–913. https://doi.org/10.1016/j.neuron.2008.08.020

Hill, D. N., Varga, Z., Jia, H., Sakmann, B., & Konnerth, A. (2013). Multibranch activity in basal and tuft dendrites during firing of layer 5 cortical neurons in vivo. *Proceedings of the National Academy of Sciences*, *110*(33), 13618–13623. https://doi.org/10.1073/pnas.1312599110

Hochbaum, D. R., Zhao, Y., Farhi, S. L., Klapoetke, N., Werley, C. A., Kapoor, V., Zou, P., Kralj, J. M., Maclaurin, D., Smedemark-Margulies, N., Saulnier, J. L., Boulting, G. L., Straub, C., Cho, Y. K., Melkonian, M., Wong, G. K.-S., Harrison, D. J., Murthy, V. N., Sabatini, B. L., … Cohen, A. E. (2014). All-optical electrophysiology in mammalian neurons using engineered microbial rhodopsins. *Nature Methods*, *11*(8), Article 8. https://doi.org/10.1038/nmeth.3000

Hodgkin, A. L., & Huxley, A. F. (1939). Action Potentials Recorded from Inside a Nerve Fibre. *Nature*, *144*(3651), Article 3651. https://doi.org/10.1038/144710a0

Holler, S., Köstinger, G., Martin, K. A. C., Schuhknecht, G. F. P., & Stratford, K. J. (2021). Structure and function of a neocortical synapse. *Nature*, *591*(7848), Article 7848. https://doi.org/10.1038/s41586-020-03134-2

Holtmaat, A. J. G. D., Trachtenberg, J. T., Wilbrecht, L., Shepherd, G. M., Zhang, X., Knott, G. W., & Svoboda, K. (2005). Transient and Persistent Dendritic Spines in the Neocortex In Vivo. *Neuron*, *45*(2), 279–291. https://doi.org/10.1016/j.neuron.2005.01.003

Hsueh, B., Chen, R., Jo, Y., Tang, D., Raffiee, M., Kim, Y. S., Inoue, M., Randles, S., Ramakrishnan, C., Patel, S., Kim, D. K., Liu, T. X., Kim, S. H., Tan, L., Mortazavi, L., Cordero, A., Shi, J., Zhao, M., Ho, T. T., … Deisseroth, K. (2023). Cardiogenic control of affective behavioural state. *Nature*, *615*(7951), Article 7951. https://doi.org/10.1038/s41586-023-05748-8

Hubel, D. H., & Wiesel, T. N. (1959). Receptive fields of single neurones in the cat’s striate cortex. *The Journal of Physiology*, *148*(3), 574–591. https://doi.org/10.1113/jphysiol.1959.sp006308

Huber, D., Gutnisky, D. A., Peron, S., O’Connor, D. H., Wiegert, J. S., Tian, L., Oertner, T. G., Looger, L. L., & Svoboda, K. (2012). Multiple dynamic representations in the motor cortex during sensorimotor learning. *Nature*, *484*(7395), Article 7395. https://doi.org/10.1038/nature11039

Iascone, D. M., Li, Y., Sümbül, U., Doron, M., Chen, H., Andreu, V., Goudy, F., Blockus, H., Abbott, L. F., Segev, I., Peng, H., & Polleux, F. (2020). Whole-Neuron Synaptic Mapping Reveals Spatially Precise Excitatory/Inhibitory Balance Limiting Dendritic and Somatic Spiking. *Neuron*, *106*(4), 566-578.e8. https://doi.org/10.1016/j.neuron.2020.02.015

Inoue, M., Takeuchi, A., Manita, S., Horigane, S., Sakamoto, M., Kawakami, R., Yamaguchi, K., Otomo, K., Yokoyama, H., Kim, R., Yokoyama, T., Takemoto-Kimura, S., Abe, M., Okamura, M., Kondo, Y., Quirin, S., Ramakrishnan, C., Imamura, T., Sakimura, K., … Bito, H. (2019). Rational Engineering of XCaMPs, a Multicolor GECI Suite for In Vivo Imaging of Complex Brain Circuit Dynamics. *Cell*, *177*(5), 1346-1360.e24. https://doi.org/10.1016/j.cell.2019.04.007

Iyer, V., Hoogland, T. M., & Saggau, P. (2006). Fast Functional Imaging of Single Neurons Using Random-Access Multiphoton (RAMP) Microscopy. *Journal of Neurophysiology*, *95*(1), 535–545. https://doi.org/10.1152/jn.00865.2005

Jia, H., Rochefort, N. L., Chen, X., & Konnerth, A. (2010). Dendritic organization of sensory input to cortical neurons in vivo. *Nature*, *464*(7293), Article 7293. https://doi.org/10.1038/nature08947

Jia, H., Rochefort, N. L., Chen, X., & Konnerth, A. (2011). In vivo two-photon imaging of sensory-evoked dendritic calcium signals in cortical neurons. *Nature Protocols*, *6*(1), Article 1. https://doi.org/10.1038/nprot.2010.169

Judkewitz, B., Rizzi, M., Kitamura, K., & Häusser, M. (2009). Targeted single-cell electroporation of mammalian neurons in vivo. *Nature Protocols*, *4*(6), Article 6. https://doi.org/10.1038/nprot.2009.56

Kavalali, E. T. (2015). The mechanisms and functions of spontaneous neurotransmitter release. *Nature Reviews. Neuroscience*, *16*(1), 5–16. https://doi.org/10.1038/nrn3875

Kerlin, A., Mohar, B., Flickinger, D., MacLennan, B. J., Dean, M. B., Davis, C., Spruston, N., & Svoboda, K. (2019). Functional clustering of dendritic activity during decision-making. *ELife*, *8*, e46966. https://doi.org/10.7554/eLife.46966

Kishi, K. E., Kim, Y. S., Fukuda, M., Inoue, M., Kusakizako, T., Wang, P. Y., Ramakrishnan, C., Byrne, E. F. X., Thadhani, E., Paggi, J. M., Matsui, T. E., Yamashita, K., Nagata, T., Konno, M., Quirin, S., Lo, M., Benster, T., Uemura, T., Liu, K., … Kato, H. E. (2022). Structural basis for channel conduction in the pump-like channelrhodopsin ChRmine. *Cell*, *185*(4), 672-689.e23. https://doi.org/10.1016/j.cell.2022.01.007

Kralj, J. M., Douglass, A. D., Hochbaum, D. R., Maclaurin, D., & Cohen, A. E. (2011). Optical recording of action potentials in mammalian neurons using a microbial rhodopsin. *Nature Methods*, *9*(1), 90–95. https://doi.org/10.1038/nmeth.1782

LaFosse, P. K., Zhou, Z., Friedman, N. G., Deng, Y., Li, A. J., Akitake, B., & Histed, M. H. (2023). Bicistronic Expression of a High-Performance Calcium Indicator and Opsin for All-Optical Stimulation and Imaging at Cellular Resolution. *ENeuro*, *10*(3), ENEURO.0378-22.2023. https://doi.org/10.1523/ENEURO.0378-22.2023

Landau, A. T., Park, P., Wong-Campos, J. D., Tian, H., Cohen, A. E., & Sabatini, B. L. (2022). Dendritic branch structure compartmentalizes voltage-dependent calcium influx in cortical layer 2/3 pyramidal cells. *ELife*, *11*, e76993. https://doi.org/10.7554/eLife.76993

Larkman, A. U. (1991). Dendritic morphology of pyramidal neurones of the visual cortex of the rat: III. Spine distributions. *The Journal of Comparative Neurology*, *306*(2), 332–343. https://doi.org/10.1002/cne.903060209

Larkum, M. (2013). A cellular mechanism for cortical associations: An organizing principle for the cerebral cortex. *Trends in Neurosciences*, *36*(3), 141–151. https://doi.org/10.1016/j.tins.2012.11.006

Larkum, M., Waters, J., Sakmann, B., & Helmchen, F. (2007). Dendritic Spikes in Apical Dendrites of Neocortical Layer 2/3 Pyramidal Neurons. *Journal of Neuroscience*, *27*(34), 8999–9008. https://doi.org/10.1523/JNEUROSCI.1717-07.2007

Larkum, M., Zhu, J. J., & Sakmann, B. (1999). A new cellular mechanism for coupling inputs arriving at different cortical layers. *Nature*, *398*(6725), Article 6725. https://doi.org/10.1038/18686

Lavzin, M., Rapoport, S., Polsky, A., Garion, L., & Schiller, J. (2012). Nonlinear dendritic processing determines angular tuning of barrel cortex neurons in vivo. *Nature*, *490*(7420), Article 7420. https://doi.org/10.1038/nature11451

Ledergerber, D., & Larkum, M. E. (2010). Properties of layer 6 pyramidal neuron apical dendrites. *The Journal of Neuroscience: The Official Journal of the*

Society for Neuroscience, *30*(39), 13031–13044. https://doi.org/10.1523/JNEUROSCI.2254-10.2010

Liang, R., Broussard, G. J., & Tian, L. (2015). Imaging Chemical Neurotransmission with Genetically Encoded Fluorescent Sensors. *ACS Chemical Neuroscience*, *6*(1), 84–93. https://doi.org/10.1021/cn500280k

Lima, S. Q., & Miesenböck, G. (2005). Remote Control of Behavior through Genetically Targeted Photostimulation of Neurons. *Cell*, *121*(1), 141–152. https://doi.org/10.1016/j.cell.2005.02.004

Lin, M. Z., & Schnitzer, M. J. (2016). Genetically encoded indicators of neuronal activity. *Nature Neuroscience*, *19*(9), Article 9. https://doi.org/10.1038/nn.4359

Liu, Z., Lu, X., Villette, V., Gou, Y., Colbert, K. L., Lai, S., Guan, S., Land, M. A., Lee, J., Assefa, T., Zollinger, D. R., Korympidou, M. M., Vlasits, A. L., Pang, M. M., Su, S., Cai, C., Froudarakis, E., Zhou, N., Patel, S. S., … St-Pierre, F. (2022). Sustained deep-tissue voltage recording using a fast indicator evolved for two-photon microscopy. *Cell*, *185*(18), 3408-3425.e29. https://doi.org/10.1016/j.cell.2022.07.013

London, M., & Häusser, M. (2005). Dendritic Computation. *Annual Review of Neuroscience*, *28*(1), 503–532. https://doi.org/10.1146/annurev.neuro.28.061604.135703

Magee, J. C., & Johnston, D. (1997). A synaptically controlled, associative signal for Hebbian plasticity in hippocampal neurons. *Science (New York, N.Y.)*, *275*(5297), 209–213. https://doi.org/10.1126/science.275.5297.209

Major, G., Larkum, M. E., & Schiller, J. (2013). Active Properties of Neocortical Pyramidal Neuron Dendrites. *Annual Review of Neuroscience*, *36*(1), 1–24. https://doi.org/10.1146/annurev-neuro-062111-150343

Major, G., Polsky, A., Denk, W., Schiller, J., & Tank, D. W. (2008). Spatiotemporally Graded NMDA Spike/Plateau Potentials in Basal Dendrites of Neocortical Pyramidal Neurons. *Journal of Neurophysiology*, *99*(5), 2584–2601. https://doi.org/10.1152/jn.00011.2008

Manita, S., Suzuki, T., Homma, C., Matsumoto, T., Odagawa, M., Yamada, K., Ota, K., Matsubara, C., Inutsuka, A., Sato, M., Ohkura, M., Yamanaka, A., Yanagawa, Y., Nakai, J., Hayashi, Y., Larkum, M. E., & Murayama, M. (2015). A Top-Down Cortical Circuit for Accurate Sensory Perception. *Neuron*, *86*(5), 1304–1316. https://doi.org/10.1016/j.neuron.2015.05.006

Mao, T., O’Connor, D. H., Scheuss, V., Nakai, J., & Svoboda, K. (2008). Characterization and Subcellular Targeting of GCaMP-Type Genetically-Encoded Calcium Indicators. *PLoS ONE*, *3*(3), e1796. https://doi.org/10.1371/journal.pone.0001796

Marblestone, A., Zamft, B., Maguire, Y., Shapiro, M., Cybulski, T., Glaser, J., Amodei, D., Stranges, P. B., Kalhor, R., Dalrymple, D., Seo, D., Alon, E., Maharbiz, M., Carmena, J., Rabaey, J., Boyden**, E., Church**, G., & Kording**, K. (2013). Physical principles for scalable neural recording. *Frontiers in Computational Neuroscience*, *7*. https://www.frontiersin.org/articles/10.3389/fncom.2013.00137

Mardinly, A. R., Oldenburg, I. A., Pégard, N. C., Sridharan, S., Lyall, E. H., Chesnov, K., Brohawn, S. G., Waller, L., & Adesnik, H. (2018). Precise multimodal optical control of neural ensemble activity. *Nature Neuroscience*, *21*(6), Article 6. https://doi.org/10.1038/s41593-018-0139-8

Marshel, J. H., Kim, Y. S., Machado, T. A., Quirin, S., Benson, B., Kadmon, J., Raja, C., Chibukhchyan, A., Ramakrishnan, C., Inoue, M., Shane, J. C., McKnight, D. J., Yoshizawa, S., Kato, H. E., Ganguli, S., & Deisseroth, K. (2019). Cortical layer–specific critical dynamics triggering perception. *Science*, *365*(6453), eaaw5202. https://doi.org/10.1126/science.aaw5202

Marvin, J. S., Borghuis, B. G., Tian, L., Cichon, J., Harnett, M. T., Akerboom, J., Gordus, A., Renninger, S. L., Chen, T.-W., Bargmann, C. I., Orger, M. B., Schreiter, E. R., Demb, J. B., Gan, W.-B., Hires, S. A., & Looger, L. L. (2013). An optimized fluorescent probe for visualizing glutamate neurotransmission. *Nature Methods*, *10*(2), Article 2. https://doi.org/10.1038/nmeth.2333

Marvin, J. S., Scholl, B., Wilson, D. E., Podgorski, K., Kazemipour, A., Müller, J. A., Schoch, S., Quiroz, F. J. U., Rebola, N., Bao, H., Little, J. P., Tkachuk, A. N., Cai, E., Hantman, A. W., Wang, S. S.-H., DePiero, V. J., Borghuis, B. G., Chapman, E. R., Dietrich, D., … Looger, L. L. (2018). Stability, affinity, and chromatic variants of the glutamate sensor iGluSnFR. *Nature Methods*, *15*(11), Article 11. https://doi.org/10.1038/s41592-018-0171-3

Marvin, J. S., Shimoda, Y., Magloire, V., Leite, M., Kawashima, T., Jensen, T. P., Kolb, I., Knott, E. L., Novak, O., Podgorski, K., Leidenheimer, N. J., Rusakov, D. A., Ahrens, M. B., Kullmann, D. M., & Looger, L. L. (2019). A genetically encoded fluorescent sensor for in vivo imaging of GABA. *Nature Methods*, *16*(8), Article 8. https://doi.org/10.1038/s41592-019-0471-2

Matsuno-Yagi, A., & Mukohata, Y. (1977). Two possible roles of bacteriorhodopsin; a comparative study of strains of Halobacterium halobium differing in pigmentation. *Biochemical and Biophysical Research Communications*, *78*(1), 237–243. https://doi.org/10.1016/0006-291x(77)91245-1

Mattis, J., Tye, K. M., Ferenczi, E. A., Ramakrishnan, C., O'Shea, D. J., Prakash, R., Gunaydin, L. A., Hyun, M., Fenno, L. E., Gradinaru, V., Yizhar, O., & Deisseroth, K. (2011). Principles for applying optogenetic tools derived from direct comparative analysis of microbial opsins. *Nature Methods*, *9*(2), 159–172. https://doi.org/10.1038/nmeth.1808

Miyawaki, A., Llopis, J., Heim, R., McCaffery, J. M., Adams, J. A., Ikura, M., & Tsien, R. Y. (1997). Fluorescent indicators for Ca2+based on green fluorescent proteins and calmodulin. *Nature*, *388*(6645), Article 6645. https://doi.org/10.1038/42264

Moore, J. J., Ravassard, P. M., Ho, D., Acharya, L., Kees, A. L., Vuong, C., & Mehta, M. R. (2017). Dynamics of cortical dendritic membrane potential and spikes in freely behaving rats. *Science (New York, N.Y.)*, *355*(6331), eaaj1497. https://doi.org/10.1126/science.aaj1497

Nevian, T., & Sakmann, B. (2006). Spine Ca2+ Signaling in Spike-Timing-Dependent Plasticity. *Journal of Neuroscience*, *26*(43), 11001–11013. https://doi.org/10.1523/JNEUROSCI.1749-06.2006

Noguchi, J., Nagaoka, A., Watanabe, S., Ellis-Davies, G. C. R., Kitamura, K., Kano, M., Matsuzaki, M., & Kasai, H. (2011). In vivo two-photon uncaging of glutamate revealing the structure–function relationships of dendritic spines in the neocortex of adult mice. *The Journal of Physiology*, *589*(10), 2447–2457. https://doi.org/10.1113/jphysiol.2011.207100

Norman, S. L., Maresca, D., Christopoulos, V. N., Griggs, W. S., Demene, C., Tanter, M., Shapiro, M. G., & Andersen, R. A. (2021). Single-trial decoding of movement intentions using functional ultrasound neuroimaging. *Neuron*, *109*(9), 1554-1566.e4. https://doi.org/10.1016/j.neuron.2021.03.003

Oswald, A.-M. M., Chacron, M. J., Doiron, B., Bastian, J., & Maler, L. (2004). Parallel Processing of Sensory Input by Bursts and Isolated Spikes. *The Journal of Neuroscience*, *24*(18), 4351–4362. https://doi.org/10.1523/JNEUROSCI.0459-04.2004

Packer, A., Peterka, D. S., Hirtz, J. J., Prakash, R., Deisseroth, K., & Yuste, R. (2012). Two-photon optogenetics of dendritic spines and neural circuits. *Nature Methods*, *9*(12), Article 12. https://doi.org/10.1038/nmeth.2249

Packer, A., Roska, B., & Häusser, M. (2013). Targeting neurons and photons for optogenetics. *Nature Neuroscience*, *16*(7), Article 7. https://doi.org/10.1038/nn.3427

Packer, A., Russell, L. E., Dalgleish, H. W. P., & Häusser, M. (2015). Simultaneous all-optical manipulation and recording of neural circuit activity with cellular resolution in vivo. *Nature Methods*, *12*(2), Article 2. https://doi.org/10.1038/nmeth.3217

Palmer, L. M., Shai, A. S., Reeve, J. E., Anderson, H. L., Paulsen, O., & Larkum, M. E. (2014). NMDA spikes enhance action potential generation during sensory input. *Nature Neuroscience*, *17*(3), Article 3. https://doi.org/10.1038/nn.3646

Papagiakoumou, E., Ronzitti, E., Chen, I.-W., Gajowa, M., Picot, A., & Emiliani, V. (2018). Two-Photon Optogenetics by Computer-Generated Holography. In A. Stroh (Ed.), *Optogenetics: A Roadmap* (pp. 175–197). Springer. https://doi.org/10.1007/978-1-4939-7417-7_10

Papaioannou, S., & Medini, P. (2022). Advantages, Pitfalls, and Developments of All Optical Interrogation Strategies of Microcircuits in vivo. *Frontiers in Neuroscience*, *16*. https://www.frontiersin.org/articles/10.3389/fnins.2022.859803

Paredes, R. M., Etzler, J. C., Watts, L. T., Zheng, W., & Lechleiter, J. D. (2008). Chemical calcium indicators. *Methods (San Diego, Calif.)*, *46*(3), 143–151. https://doi.org/10.1016/j.ymeth.2008.09.025

Patriarchi, T., Mohebi, A., Sun, J., Marley, A., Liang, R., Dong, C., Puhger, K., Mizuno, G. O., Davis, C. M., Wiltgen, B., von Zastrow, M., Berke, J. D., & Tian, L. (2020). An expanded palette of dopamine sensors for multiplex imaging in vivo. *Nature Methods*, *17*(11), Article 11. https://doi.org/10.1038/s41592-020-0936-3

Payeur, A., Guerguiev, J., Zenke, F., Richards, B. A., & Naud, R. (2021). Burst-dependent synaptic plasticity can coordinate learning in hierarchical circuits. *Nature Neuroscience*, *24*(7), Article 7. https://doi.org/10.1038/s41593-021-00857-x

Peron, S. P., Freeman, J., Iyer, V., Guo, C., & Svoboda, K. (2015). A Cellular Resolution Map of Barrel Cortex Activity during Tactile Behavior. *Neuron*, *86*(3), 783–799. https://doi.org/10.1016/j.neuron.2015.03.027

Peron, S., & Svoboda, K. (2011). From cudgel to scalpel: Toward precise neural control with optogenetics. *Nature Methods*, *8*(1), 30–34. https://doi.org/10.1038/nmeth.f.325

Piccolino, M. (2006). Luigi Galvani's path to animal electricity. *Comptes Rendus Biologies*, *329*(5), 303–318. https://doi.org/10.1016/j.crvi.2006.03.002

Poirazi, P., Brannon, T., & Mel, B. W. (2003). Pyramidal Neuron as Two-Layer Neural Network. *Neuron*, *37*(6), 989–999. https://doi.org/10.1016/S0896-6273(03)00149-1

Polsky, A., Mel, B. W., & Schiller, J. (2004). Computational subunits in thin dendrites of pyramidal cells. *Nature Neuroscience*, *7*(6), Article 6. https://doi.org/10.1038/nn1253

Poort, J., Raudies, F., Wannig, A., Lamme, V. A. F., Neumann, H., & Roelfsema, P. R. (2012). The role of attention in figure-ground segregation in areas V1 and V4 of the visual cortex. *Neuron*, *75*(1), 143–156. https://doi.org/10.1016/j.neuron.2012.04.032

Prakash, R., Yizhar, O., Grewe, B., Ramakrishnan, C., Wang, N., Goshen, I., Packer, A. M., Peterka, D. S., Yuste, R., Schnitzer, M. J., & Deisseroth, K. (2012). Two-photon optogenetic toolbox for fast inhibition, excitation and bistable modulation. *Nature Methods*, *9*(12), Article 12. https://doi.org/10.1038/nmeth.2215

Rall, W. (1994). *Theoretical Significance of Dendritic Trees for Neuronal Input-Output Relations (1964)*. https://doi.org/10.7551/mitpress/6743.003.0015

Reifenrath, M., & Boles, E. (2018). A superfolder variant of pH-sensitive pHluorin for in vivo pH measurements in the endoplasmic reticulum. *Scientific Reports*, *8*(1), Article 1. https://doi.org/10.1038/s41598-018-30367-z

Reiff, D. F., Ihring, A., Guerrero, G., Isacoff, E. Y., Joesch, M., Nakai, J., & Borst, A. (2005). In Vivo Performance of Genetically Encoded Indicators of Neural Activity in Flies. *The Journal of Neuroscience*, *25*(19), 4766–4778. https://doi.org/10.1523/JNEUROSCI.4900-04.2005

Rickgauer, J. P., Deisseroth, K., & Tank, D. W. (2014). Simultaneous cellular-resolution optical perturbation and imaging of place cell firing fields. *Nature Neuroscience*, *17*(12), Article 12. https://doi.org/10.1038/nn.3866

Rickgauer, J. P., & Tank, D. W. (2009). Two-photon excitation of channelrhodopsin-2 at saturation. *Proceedings of the National Academy of Sciences of the United States of America*, *106*(35), 15025–15030. https://doi.org/10.1073/pnas.0907084106

Ronzitti, E., Conti, R., Zampini, V., Tanese, D., Foust, A. J., Klapoetke, N., Boyden, E. S., Papagiakoumou, E., & Emiliani, V. (2017). Submillisecond Optogenetic Control of Neuronal Firing with Two-Photon Holographic Photoactivation of Chronos. *The Journal of Neuroscience: The Official Journal of the Society for Neuroscience*, *37*(44), 10679–10689. https://doi.org/10.1523/JNEUROSCI.1246-17.2017

Russell, J. (2011). Imaging calcium signals in vivo: A powerful tool in physiology and pharmacology. *British Journal of Pharmacology*, *163*(8), 1605–1625. https://doi.org/10.1111/j.1476-5381.2010.00988.x

Russell, L., Dalgleish, H. W. P., Nutbrown, R., Gauld, O. M., Herrmann, D., Fişek, M., Packer, A. M., & Häusser, M. (2022). All-optical interrogation of neural circuits in behaving mice. *Nature Protocols*, *17*(7), Article 7. https://doi.org/10.1038/s41596-022-00691-w

Russell, L., Yang, Z., Tan, P. L., Fişek, M., Packer, A. M., Dalgleish, H. W. P., Chettih, S., Harvey, C. D., & Häusser, M. (2019). *The influence of visual cortex on perception is modulated by behavioural state* (p. 706010). bioRxiv. https://doi.org/10.1101/706010

Sacramento, J., Ponte Costa, R., Bengio, Y., & Senn, W. (2018). Dendritic cortical microcircuits approximate the backpropagation algorithm. *Advances in Neural Information Processing Systems*, *31*. https://proceedings.neurips.cc/paper/2018/hash/1dc3a89d0d440ba31729b0ba74b93a33-Abstract.html

Saggau, P., Bullen, A., & Patel, S. S. (1998). Acousto-optic random-access laser scanning microscopy: Fundamentals and applications to optical recording of neuronal activity. *Cellular and Molecular Biology (Noisy-Le-Grand, France)*, *44*(5), 827–846.

Salomé, R., Kremer, Y., Dieudonné, S., Léger, J.-F., Krichevsky, O., Wyart, C., Chatenay, D., & Bourdieu, L. (2006). Ultrafast random-access scanning in two-photon microscopy using acousto-optic deflectors. *Journal of Neuroscience Methods*, *154*(1), 161–174. https://doi.org/10.1016/j.jneumeth.2005.12.010

Sankaranarayanan, S., De Angelis, D., Rothman, J. E., & Ryan, T. A. (2000). The Use of pHluorins for Optical Measurements of Presynaptic Activity. *Biophysical Journal*, *79*(4), 2199–2208. https://doi.org/10.1016/S0006-3495(00)76468-X

Scanziani, M., & Häusser, M. (2009). Electrophysiology in the age of light. *Nature*, *461*(7266), Article 7266. https://doi.org/10.1038/nature08540

Schiller, J., Major, G., Koester, H. J., & Schiller, Y. (2000). NMDA spikes in basal dendrites of cortical pyramidal neurons. *Nature*, *404*(6775), Article 6775. https://doi.org/10.1038/35005094

Schiller, J., Schiller, Y., Stuart, G., & Sakmann, B. (1997). Calcium action potentials restricted to distal apical dendrites of rat neocortical pyramidal neurons. *The Journal of Physiology*, *505*(3), 605–616. https://doi.org/10.1111/j.1469-7793.1997.605ba.x

Schnabel, U. H., Bossens, C., Lorteije, J. A. M., Self, M. W., Op de Beeck, H., & Roelfsema, P. R. (2018). Figure-ground perception in the awake mouse and neuronal activity elicited by figure-ground stimuli in primary visual cortex. *Scientific Reports*, *8*(1), Article 1. https://doi.org/10.1038/s41598-018-36087-8

Schoenfeld, G., Kollmorgen, S., Lewis, C., Bethge, P., Reuss, A. M., Aguzzi, A., Mante, V., & Helmchen, F. (2021). *Dendritic integration of sensory and reward information facilitates learning* (p. 2021.12.28.474360). bioRxiv. https://doi.org/10.1101/2021.12.28.474360

Schuetze, S. M. (1983). The discovery of the action potential. *Trends in Neurosciences*, *6*, 164–168. https://doi.org/10.1016/0166-2236(83)90078-4

Scott, L. L., Hage, T. A., & Golding, N. L. (2007). Weak action potential backpropagation is associated with high-frequency axonal firing capability in principal neurons of the gerbil medial superior olive. *The Journal of Physiology*, *583*(Pt 2), 647–661. https://doi.org/10.1113/jphysiol.2007.136366

Shemesh, O. A., Linghu, C., Piatkevich, K. D., Goodwin, D., Celiker, O. T., Gritton, H. J., Romano, M. F., Gao, R., Yu, C.-C. (Jay), Tseng, H.-A., Bensussen, S., Narayan, S., Yang, C.-T., Freifeld, L., Siciliano, C. A., Gupta, I., Wang, J., Pak, N., Yoon, Y.-G., … Boyden, E. S. (2020). Precision Calcium Imaging of Dense Neural Populations via a Cell-Body-Targeted Calcium Indicator. *Neuron*, *107*(3), 470-486.e11. https://doi.org/10.1016/j.neuron.2020.05.029

Shimomura, O., Johnson, F. H., & Saiga, Y. (1962). Extraction, Purification and Properties of Aequorin, a Bioluminescent Protein from the Luminous Hydromedusan, Aequorea. *Journal of Cellular and Comparative Physiology*, *59*(3), 223–239. https://doi.org/10.1002/jcp.1030590302

Sjöström, P. J., & Häusser, M. (2006). A Cooperative Switch Determines the Sign of Synaptic Plasticity in Distal Dendrites of Neocortical Pyramidal Neurons. *Neuron*, *51*(2), 227–238. https://doi.org/10.1016/j.neuron.2006.06.017

Sjöström, P. J., & Nelson, S. B. (2002). Spike timing, calcium signals and synaptic plasticity. *Current Opinion in Neurobiology*, *12*(3), 305–314. https://doi.org/10.1016/s0959-4388(02)00325-2

Smith, S. L., Smith, I. T., Branco, T., & Häusser, M. (2013). Dendritic spikes enhance stimulus selectivity in cortical neurons in vivo. *Nature*, *503*(7474), Article 7474. https://doi.org/10.1038/nature12600

Somogyi, P., Cowey, A., Halász, N., & Freund, T. F. (1981). Vertical organization of neurones accumulating 3H-GABA in visual cortex of rhesus monkey. *Nature*, *294*(5843), Article 5843. https://doi.org/10.1038/294761a0

Spruston, N. (2008). Pyramidal neurons: Dendritic structure and synaptic integration. *Nature Reviews Neuroscience*, *9*(3), Article 3. https://doi.org/10.1038/nrn2286

Spruston, N., & Kath, W. L. (2004). Dendritic arithmetic. *Nature Neuroscience*, *7*(6), Article 6. https://doi.org/10.1038/nn0604-567

Sridharan, S., Gajowa, M. A., Ogando, M. B., Jagadisan, U. K., Abdeladim, L., Sadahiro, M., Bounds, H. A., Hendricks, W. D., Turney, T. S., Tayler, I., Gopakumar, K., Oldenburg, I. A., Brohawn, S. G., & Adesnik, H. (2022). High-performance microbial opsins for spatially and temporally precise perturbations of large neuronal networks. *Neuron*, *110*(7), 1139-1155.e6. https://doi.org/10.1016/j.neuron.2022.01.008

Sternson, S. M., & Roth, B. L. (2014). Chemogenetic Tools to Interrogate Brain Functions. *Annual Review of Neuroscience*, *37*(1), 387–407. https://doi.org/10.1146/annurev-neuro-071013-014048

Stevenson, I. H., & Kording, K. P. (2011). How advances in neural recording affect data analysis. *Nature Neuroscience*, *14*(2), Article 2. https://doi.org/10.1038/nn.2731

Stirman, J. N., Smith, I. T., Kudenov, M. W., & Smith, S. L. (2016). Wide field-of-view, multi-region, two-photon imaging of neuronal activity in the mammalian brain. *Nature Biotechnology*, *34*(8), Article 8. https://doi.org/10.1038/nbt.3594

St-Pierre, F., Marshall, J. D., Yang, Y., Gong, Y., Schnitzer, M. J., & Lin, M. Z. (2014). High-fidelity optical reporting of neuronal electrical activity with an ultrafast fluorescent voltage sensor. *Nature Neuroscience*, *17*(6), Article 6. https://doi.org/10.1038/nn.3709

Stuart, G., & Häusser, M. (2001). Dendritic coincidence detection of EPSPs and action potentials. *Nature Neuroscience*, *4*(1), Article 1. https://doi.org/10.1038/82910

Stuart, G., & Sakmann, B. (1994). Active propagation of somatic action potentials into neocortical pyramidal cell dendrites. *Nature*, *367*(6458), Article 6458. https://doi.org/10.1038/367069a0

Stuart, G., Spruston, N., Sakmann, B., & Häusser, M. (1997). Action potential initiation and backpropagation in neurons of the mammalian CNS. *Trends in Neurosciences*, *20*(3), 125–131. https://doi.org/10.1016/s0166-2236(96)10075-8

Sun, F., Zeng, J., Jing, M., Zhou, J., Feng, J., Owen, S. F., Luo, Y., Li, F., Wang, H., Yamaguchi, T., Yong, Z., Gao, Y., Peng, W., Wang, L., Zhang, S., Du, J., Lin, D., Xu, M., Kreitzer, A. C., … Li, Y. (2018). A Genetically Encoded Fluorescent Sensor Enables Rapid and Specific Detection of Dopamine in Flies, Fish, and Mice. *Cell*, *174*(2), 481-496.e19. https://doi.org/10.1016/j.cell.2018.06.042

Svoboda, K., Helmchen, F., Denk, W., & Tank, D. W. (1999). Spread of dendritic excitation in layer 2/3 pyramidal neurons in rat barrel cortex in vivo. *Nature Neuroscience*, *2*(1), Article 1. https://doi.org/10.1038/4569

Takahashi, N., Oertner, T. G., Hegemann, P., & Larkum, M. E. (2016). Active cortical dendrites modulate perception. *Science*, *354*(6319), 1587–1590. https://doi.org/10.1126/science.aah6066

Tao, C., Zhang, G., Xiong, Y., & Zhou, Y. (2015). Functional dissection of synaptic circuits: In vivo patch-clamp recording in neuroscience. *Frontiers in Neural Circuits*, *9*, 23. https://doi.org/10.3389/fncir.2015.00023

Tsien, R. Y. (1980). New calcium indicators and buffers with high selectivity against magnesium and protons: Design, synthesis, and properties of prototype structures. *Biochemistry*, *19*(11), 2396–2404. https://doi.org/10.1021/bi00552a018

Unger, E. K., Keller, J. P., Altermatt, M., Liang, R., Matsui, A., Dong, C., Hon, O. J., Yao, Z., Sun, J., Banala, S., Flanigan, M. E., Jaffe, D. A., Hartanto, S., Carlen, J., Mizuno, G. O., Borden, P. M., Shivange, A. V., Cameron, L. P., Sinning, S., … Tian, L. (2020). Directed Evolution of a Selective and Sensitive Serotonin Sensor via Machine Learning. *Cell*, *183*(7), 1986-2002.e26. https://doi.org/10.1016/j.cell.2020.11.040

Varga, Z., Jia, H., Sakmann, B., & Konnerth, A. (2011). Dendritic coding of multiple sensory inputs in single cortical neurons in vivo. *Proceedings of the National Academy of Sciences*, *108*(37), 15420–15425. https://doi.org/10.1073/pnas.1112355108

Villette, V., Chavarha, M., Dimov, I. K., Bradley, J., Pradhan, L., Mathieu, B., Evans, S. W., Chamberland, S., Shi, D., Yang, R., Kim, B. B., Ayon, A., Jalil, A., St-Pierre, F., Schnitzer, M. J., Bi, G., Toth, K., Ding, J., Dieudonné, S., & Lin, M. Z. (2019). Ultrafast Two-Photon Imaging of a High-Gain Voltage Indicator in Awake Behaving Mice. *Cell*, *179*(7), 1590-1608.e23. https://doi.org/10.1016/j.cell.2019.11.004

Vlasov, K., Van Dort, C. J., & Solt, K. (2018). Optogenetics and Chemogenetics. *Methods in Enzymology*, *603*, 181–196. https://doi.org/10.1016/bs.mie.2018.01.022

von Gersdorff, H., Sakaba, T., Berglund, K., & Tachibana, M. (1998). Submillisecond kinetics of glutamate release from a sensory synapse. *Neuron*, *21*(5), 1177–1188. https://doi.org/10.1016/s0896-6273(00)80634-0

Wang, G., Wyskiel, D. R., Yang, W., Wang, Y., Milbern, L. C., Lalanne, T., Jiang, X., Shen, Y., Sun, Q.-Q., & Zhu, J. J. (2015). An optogenetics- and imaging-assisted simultaneous multiple patch-clamp recording system for decoding complex neural circuits. *Nature Protocols*, *10*(3), 397–412. https://doi.org/10.1038/nprot.2015.019

Waters, J., & Helmchen, F. (2004). Boosting of Action Potential Backpropagation by Neocortical Network Activity In Vivo. *Journal of Neuroscience*, *24*(49), 11127–11136. https://doi.org/10.1523/JNEUROSCI.2933-04.2004

Waters, J., Larkum, M., Sakmann, B., & Helmchen, F. (2003). Supralinear Ca2+ Influx into Dendritic Tufts of Layer 2/3 Neocortical Pyramidal Neurons In Vitro and In Vivo. *Journal of Neuroscience*, *23*(24), 8558–8567. https://doi.org/10.1523/JNEUROSCI.23-24-08558.2003

Waters, J., Schaefer, A., & Sakmann, B. (2005). Backpropagating action potentials in neurones: Measurement, mechanisms and potential functions. *Progress in Biophysics and Molecular Biology*, *87*(1), 145–170. https://doi.org/10.1016/j.pbiomolbio.2004.06.009

Watson, B. O., Yuste, R., & Packer, A. M. (2016). *PackIO and EphysViewer: Software tools for acquisition and analysis of neuroscience data* (p. 054080). bioRxiv. https://doi.org/10.1101/054080

Whalley, K. (2020). Surgery-free optogenetics. *Nature Reviews Neuroscience*, *21*(12), Article 12. https://doi.org/10.1038/s41583-020-00400-0

Williams, S. R., & Stuart, G. J. (2000a). Action Potential Backpropagation and Somato-dendritic Distribution of Ion Channels in Thalamocortical Neurons. *Journal of Neuroscience*, *20*(4), 1307–1317. https://doi.org/10.1523/JNEUROSCI.20-04-01307.2000

Williams, S. R., & Stuart, G. J. (2000b). Backpropagation of Physiological Spike Trains in Neocortical Pyramidal Neurons: Implications for Temporal Coding in Dendrites. *Journal of Neuroscience*, *20*(22), 8238–8246. https://doi.org/10.1523/JNEUROSCI.20-22-08238.2000

Williams, S. R., & Stuart, G. J. (2002). Dependence of EPSP Efficacy on Synapse Location in Neocortical Pyramidal Neurons. *Science*, *295*(5561), 1907–1910. https://doi.org/10.1126/science.1067903

Williams, S. R., Zhou, X., & Fletcher, L. N. (2023). Compartment-specific dendritic information processing in striatal cholinergic interneurons is reconfigured by peptide neuromodulation. *Neuron*, *0*(0). https://doi.org/10.1016/j.neuron.2023.03.038

Wong, R. K., Prince, D. A., & Basbaum, A. I. (1979). Intradendritic recordings from hippocampal neurons. *Proceedings of the National Academy of Sciences of the United States of America*, *76*(2), 986–990. https://doi.org/10.1073/pnas.76.2.986

Wong-Campos, J. D., Park, P., Davis, H., Qi, Y., Tian, H., Itkis, D. G., Kim, D., Grimm, J. B., Plutkis, S. E., Lavis, L., & Cohen, A. E. (2023). *Voltage dynamics of dendritic integration and back-propagation in vivo* (p. 2023.05.25.542363). bioRxiv. https://doi.org/10.1101/2023.05.25.542363

Xu, N., Harnett, M. T., Williams, S. R., Huber, D., O'Connor, D. H., Svoboda, K., & Magee, J. C. (2012). Nonlinear dendritic integration of sensory and motor input during an active sensing task. *Nature*, *492*(7428), Article 7428. https://doi.org/10.1038/nature11601

Yang, G., Pan, F., & Gan, W.-B. (2009). Stably maintained dendritic spines are associated with lifelong memories. *Nature*, *462*(7275), Article 7275. https://doi.org/10.1038/nature08577

Yang, H. H., & St-Pierre, F. (2016). Genetically Encoded Voltage Indicators: Opportunities and Challenges. *The Journal of Neuroscience*, *36*(39), 9977–9989. https://doi.org/10.1523/JNEUROSCI.1095-16.2016

Yang, S., Emiliani, V., & Tang, C.-M. (2014). The kinetics of multibranch integration on the dendritic arbor of CA1 pyramidal neurons. *Frontiers in Cellular Neuroscience*, *8*. https://www.frontiersin.org/articles/10.3389/fncel.2014.00127

Yang, W., Carrillo-Reid, L., Bando, Y., Peterka, D. S., & Yuste, R. (2018). Simultaneous two-photon imaging and two-photon optogenetics of cortical circuits in three dimensions. *ELife*, *7*, e32671. https://doi.org/10.7554/eLife.32671

Yuste, R., & Denk, W. (1995). Dendritic spines as basic functional units of neuronal integration. *Nature*, *375*(6533), Article 6533. https://doi.org/10.1038/375682a0

Zeng, H., & Madisen, L. (2012). Mouse transgenic approaches in optogenetics. *Progress in Brain Research*, *196*, 193–213. https://doi.org/10.1016/B978-0-444-59426-6.00010-0

Zhang, F., Wang, L.-P., Brauner, M., Liewald, J. F., Kay, K., Watzke, N., Wood, P. G., Bamberg, E., Nagel, G., Gottschalk, A., & Deisseroth, K. (2007). Multimodal fast optical interrogation of neural circuitry. *Nature*, *446*(7136), Article 7136. https://doi.org/10.1038/nature05744

Zhang, W. H., Herde, M. K., Mitchell, J. A., Whitfield, J. H., Wulff, A. B., Vongsouthi, V., Sanchez-Romero, I., Gulakova, P. E., Minge, D., Breithausen, B., Schoch, S., Janovjak, H., Jackson, C. J., & Henneberger, C. (2018). Monitoring hippocampal glycine with the computationally designed optical sensor GlyFS. *Nature Chemical Biology*, *14*(9), 861–869. https://doi.org/10.1038/s41589-018-0108-2

Zhang, Y., Rózsa, M., Liang, Y., Bushey, D., Wei, Z., Zheng, J., Reep, D., Broussard, G. J., Tsang, A., Tsegaye, G., Narayan, S., Obara, C. J., Lim, J.-X., Patel, R., Zhang, R., Ahrens, M. B., Turner, G. C., Wang, S. S.-H., Korff, W. L., … Looger, L. L. (2021). *Fast and sensitive GCaMP calcium indicators for imaging neural populations* (p. 2021.11.08.467793). bioRxiv. https://doi.org/10.1101/2021.11.08.467793

Zhang, Z., Russell, L. E., Packer, A. M., Gauld, O. M., & Häusser, M. (2018). Closed-loop all-optical interrogation of neural circuits in vivo. *Nature Methods*, *15*(12), Article 12. https://doi.org/10.1038/s41592-018-0183-z

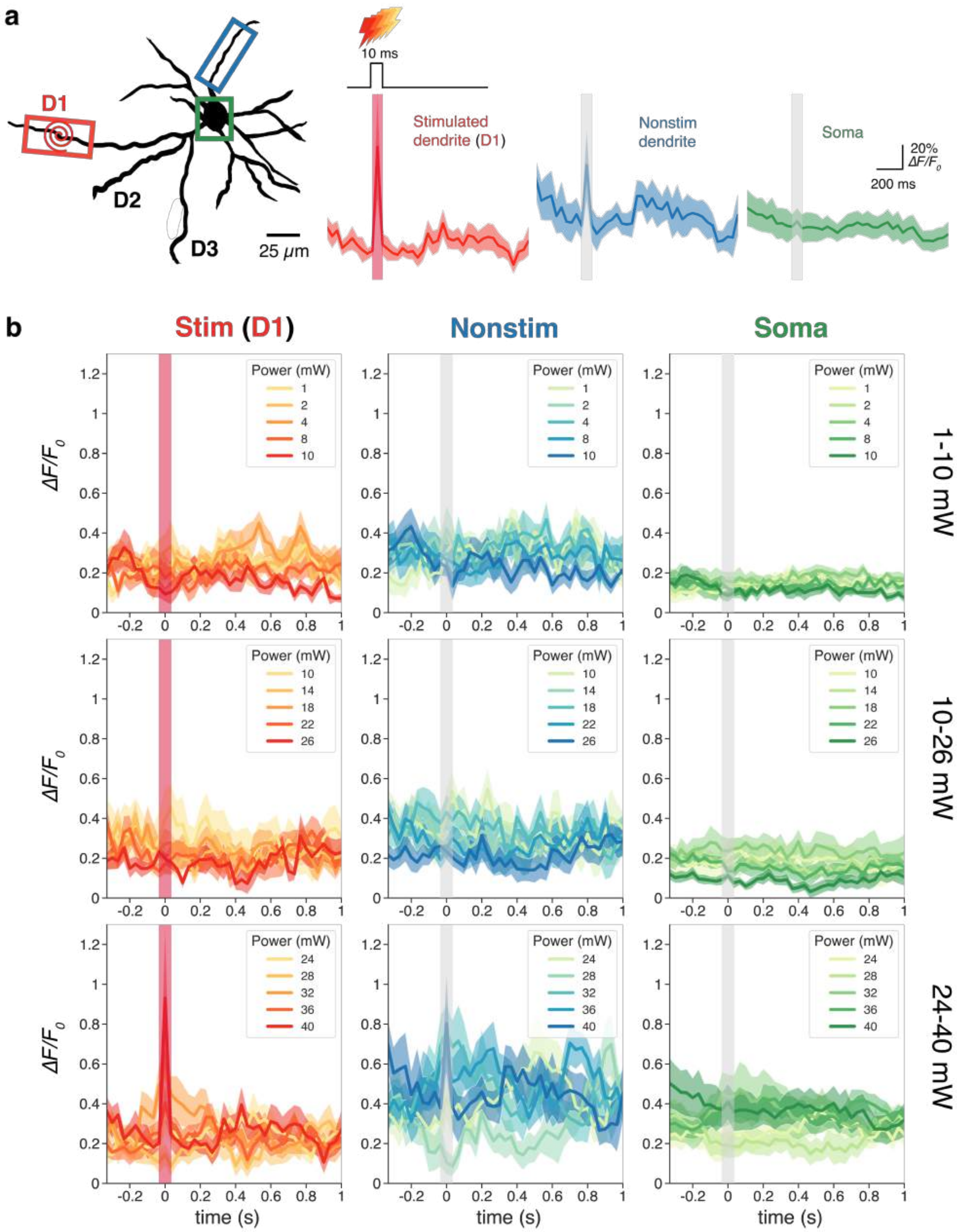

Supplementary Figure 1. Single-target photostimulation responses, dendrite 1 (D1).
a) Trial structure and example spike-triggered average response. In each trial, shown here, a randomized target and power is directed to the cell using the uncaging galvanometers. Responses were measured from the stimulated dendrite (D1, red) and compared to responses at non-stimulated dendrites (blue) and soma (green).
b) Average photostimulation-triggered responses at varying power levels (one block per row) for stimulated dendrite, non-stimulated dendrite, and somatic responses (n = 10 trials/power, 1 dendrite).

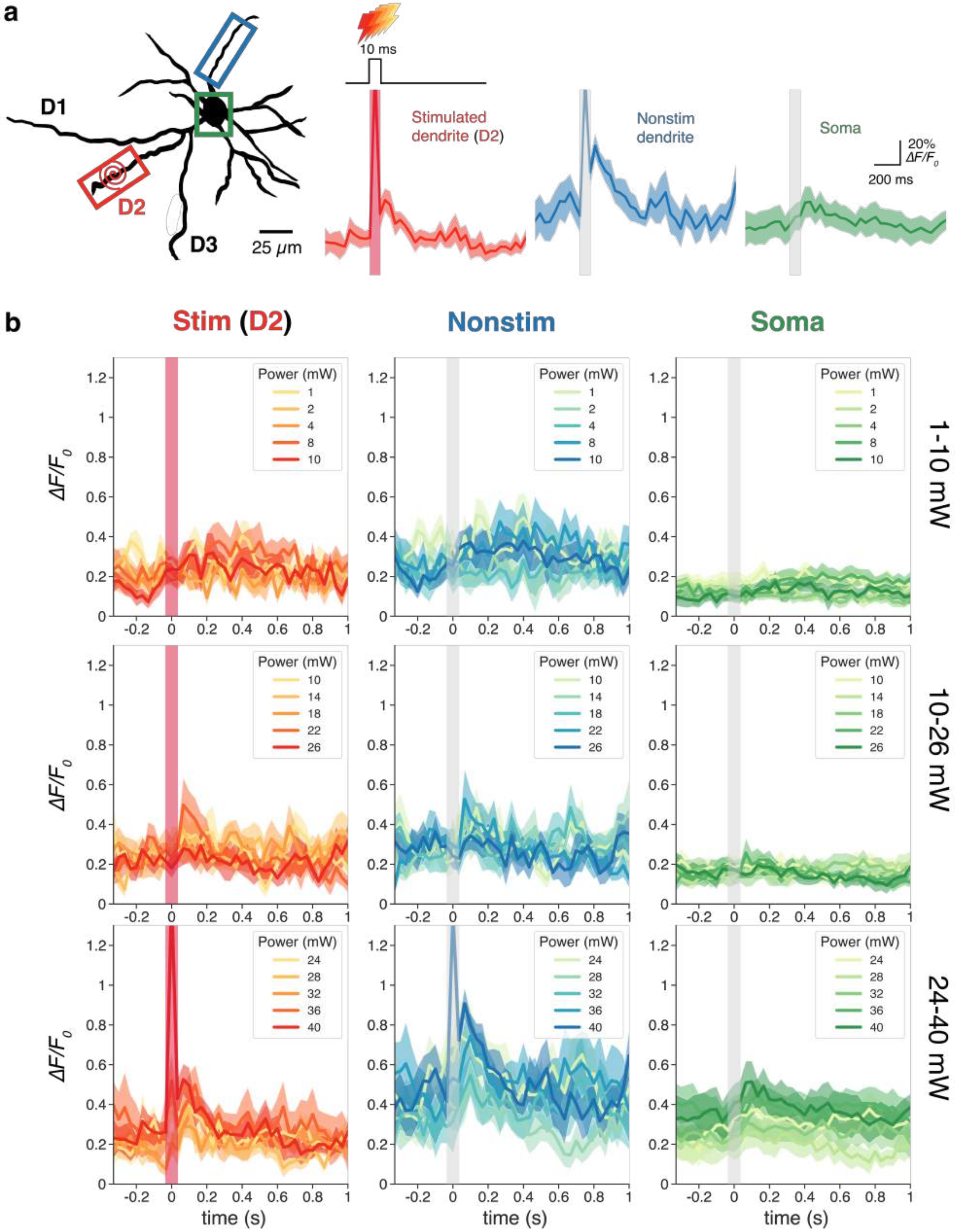

Supplementary Figure 2. Single-target photostimulation responses, dendrite 2 (D2).
a) Trial structure and example spike-triggered average response. In each trial, shown here, a randomized target and power is directed to the cell using the uncaging galvanometers. Responses were measured from the stimulated dendrite (D2, red) and compared to responses at non-stimulated dendrites (blue) and soma (green). **b)** Average photostimulation-triggered responses at varying power levels (one block per row) for stimulated dendrite, non-stimulated dendrite, and somatic responses (n = 10 trials/power, 1 dendrite).

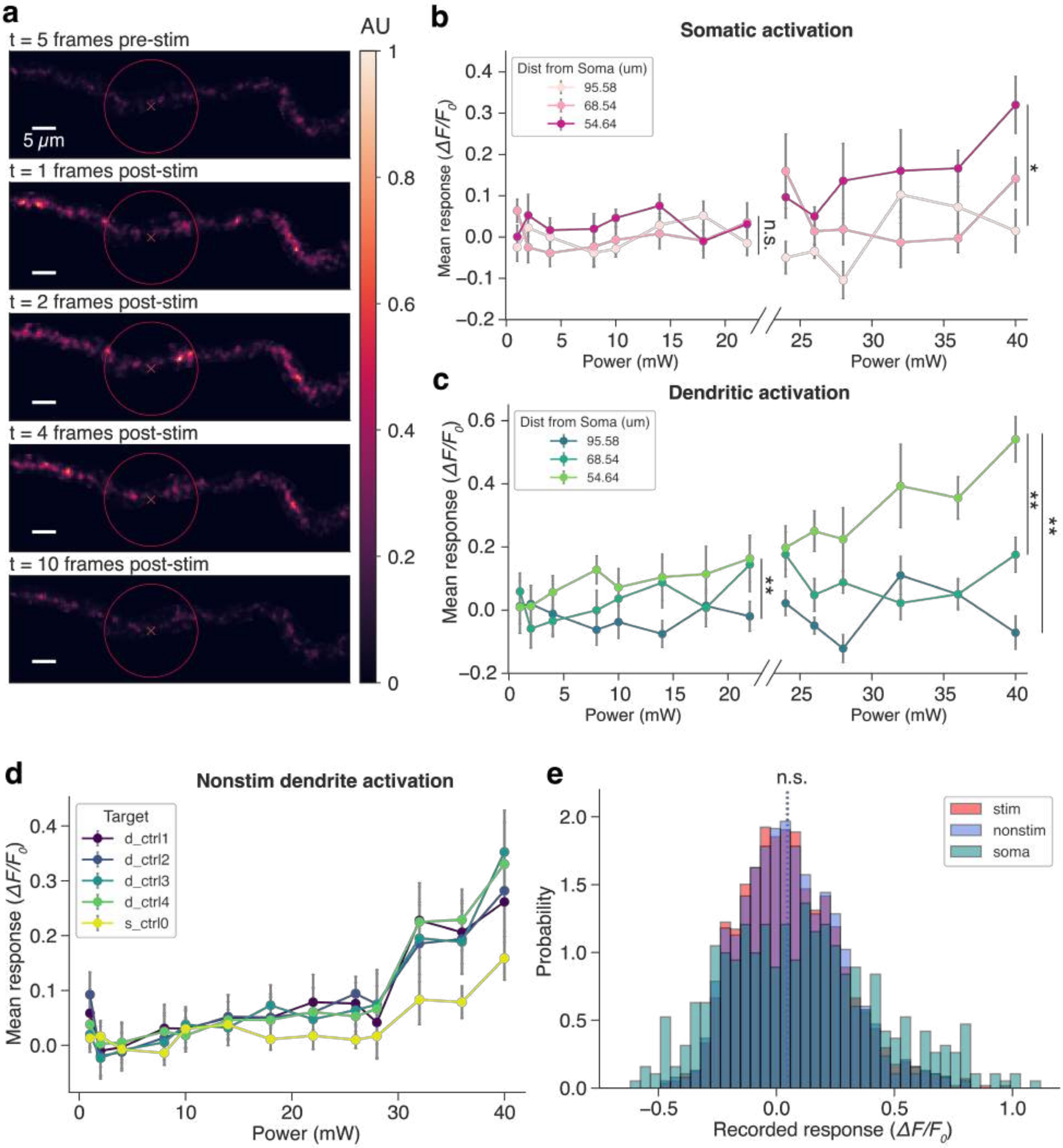

Supplementary Figure 3. Single-dendrite photostimulation dynamics.
a) Heatmap of single dendritic activation 5 frames (0.16 s) before, immediately after (0.013 - 0.133 s), and 0.33 s after stimulation. Red circles indicate stimulation area; red x's indicate centroid of stimulation spiral.
b-c) Somatic (b) and dendritic (n = 3) (c) activation by dendritic photostimulation at varying powers. Mean responses were compared for different dendritic targets at low powers (< 24 mW) and high powers (≥ 24 mW).
d) Mean response by power for non-stimulated dendrites (n = 4 dendrites, 1 neuron). Note that as the power increases, the response recorded in non-stimulated dendrites also increases.
e) Histogram of trial responses for somatic activation (teal), non-stimulated dendritic activation (blue), and stimulated dendritic activation (red). (n = 3 stimulated dendrites, 4 nonstimulated dendrites, 1 neuron, $p > 0.05$, Wilcoxon rank sum test).

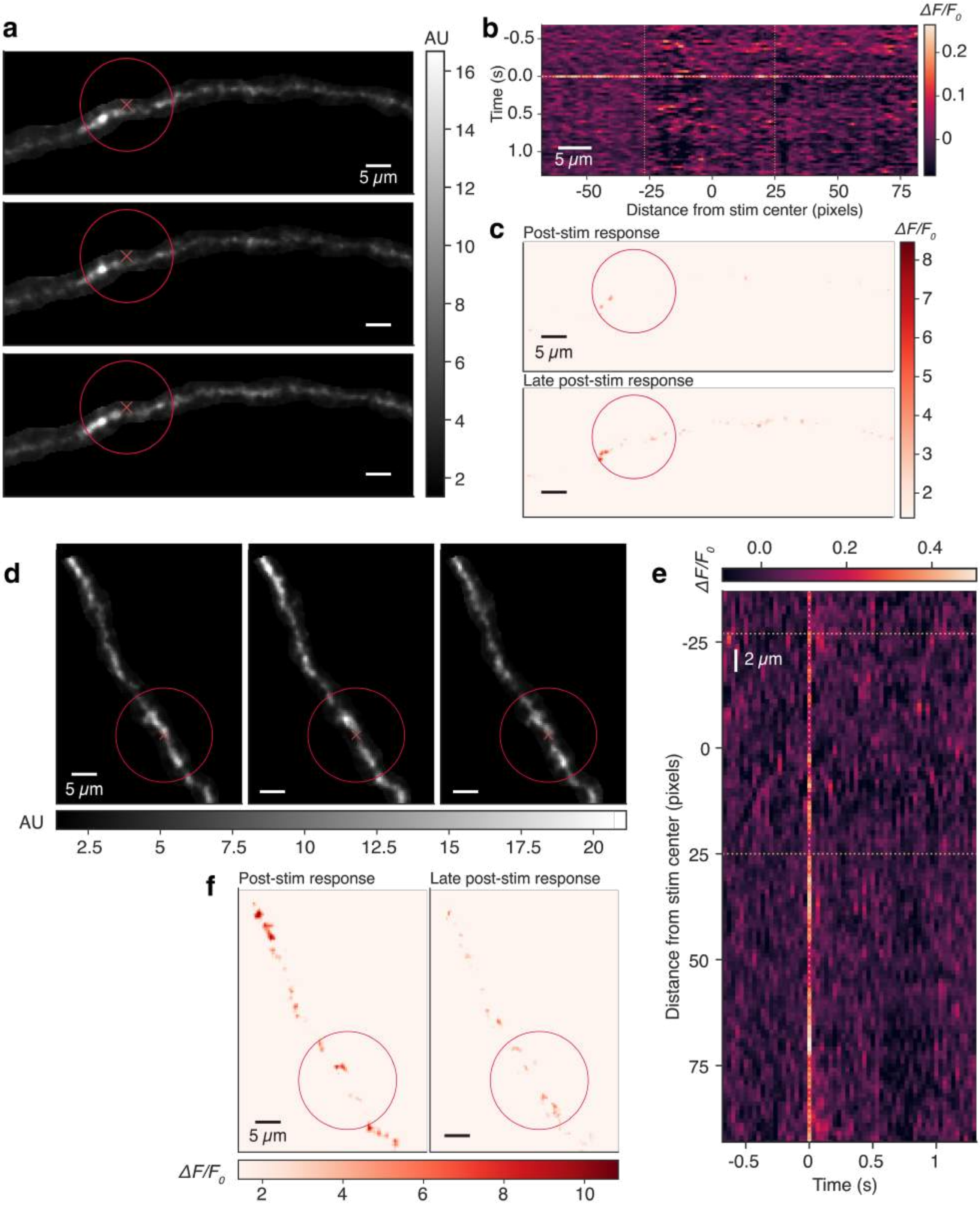

Supplementary Figure 4. Spatial characteristics of dendritic activation (D1 & D2).

a) Example FOV of D1 activation at 40 mW averaging 5 frames pre-stimulation (top), 5 frames immediately post-stimulation (center), and 5 frames during the "late" post-stimulation period (0.33-0.5 s post-stim) at 40 mW. Red x's indicate photostimulation spiral centroid. Red circle indicates spiral extent. AU, arbitrary units.

b) Heat map showing spatial spread of D1 activation across time (rows) and distance from the photostimulation spiral center (columns). Horizontal dotted line (t = 0) indicates time at which the target dendrite was stimulated. Vertical dotted lines indicate spatial extent of the photostimulation spiral. Intensity values are baseline-subtracted.

c) Baseline-normalized response of target dendrite during the immediate post-stimulation period (top) and the late post-stimulation period (bottom).

d-f) Same analyses from a-c, but for D2 activation evoked by photostimulation at 40 mW.

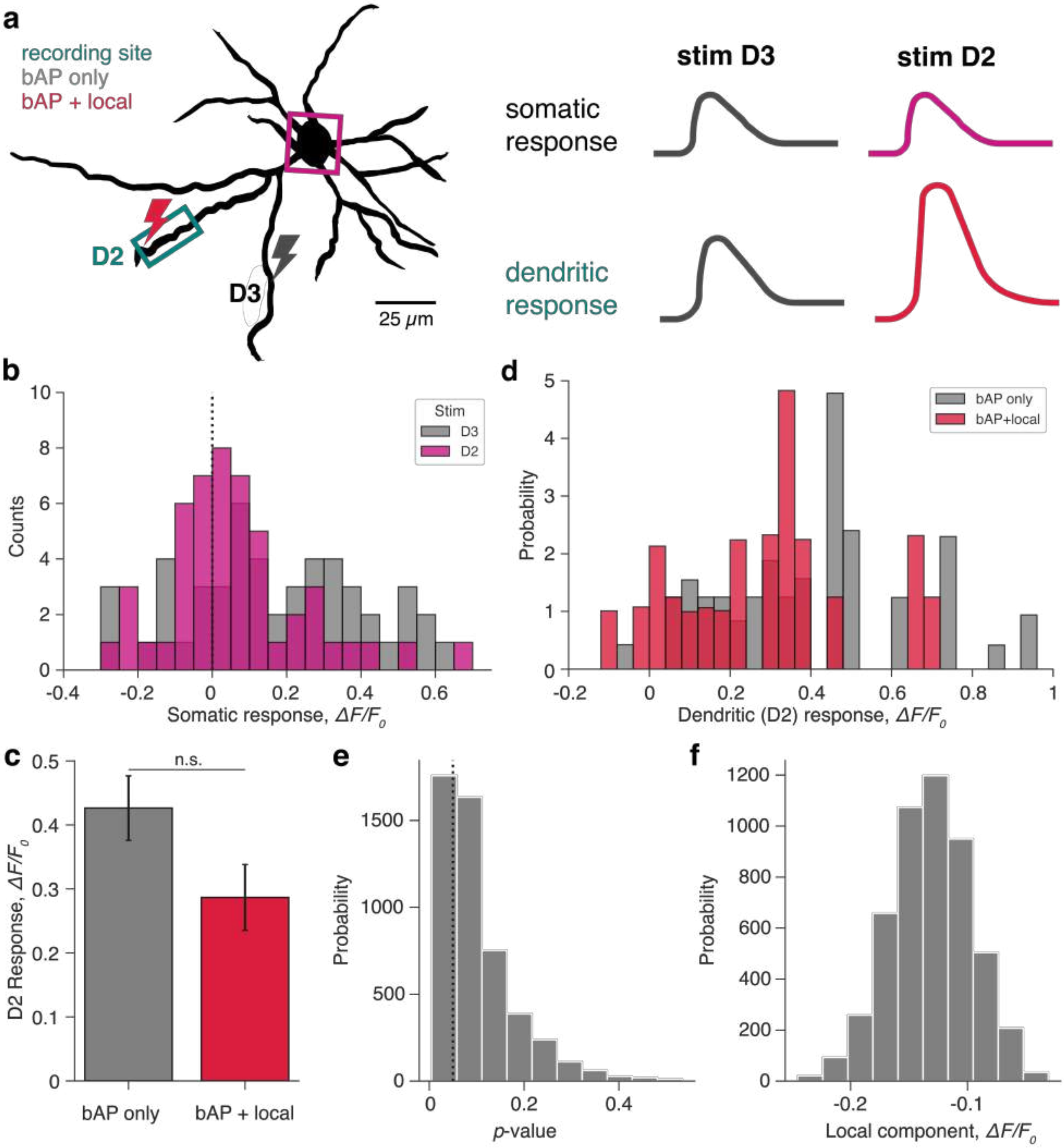

Supplementary Figure 5. Isolation of local and bAP components for D2.

a) Schematic of experiment and data analysis for isolating the local component of dendritic activation in dendrite 2 (D2). Trials in which D2 or D3 were stimulated were matched for somatic activation (top traces). Of these somatic response-matched trials, those in which D3 was stimulated ("bAP only") were compared to those in which D2 was stimulated ("bAP + local").

b) Histogram of somatic activation induced by stimulating either D2 (magenta) or D3 (grey). Trials in which non-negative somatic responses overlapped were sampled. Bootstrapping was achieved by resampling from shared bins 1,000 times (n = 100 trials, 1 neuron).

c) Example outcome from a single repetition of matched distribution sampling (n = 48 samples, 24 samples per condition). Of the sampled somatic response-matched trials, the "bAP only" condition was compared to the "bAP + local" condition as recorded from D2 activation ($p = 0.0661$, Wilcoxon rank sum test).

d) Histogram of recorded D2 trial responses due to D3 (grey, bAP only) or D2 (red, bAP + local) activation, over 1,000 rounds of resampling from the somatic response-matched trials in (b).

e) Histogram of p-values obtained from the 1,000 resamples. *P*-values were computed using the Wilcoxon rank sum test for each comparison of "bAP only" and "bAP + local" conditions. Dotted line, $p = 0.05$

f) Histogram of estimated local component in $\Delta F/F_0$, computed by subtracting "bAP only" activation of D2 from the "bAP + local" activation for each round of resampling.

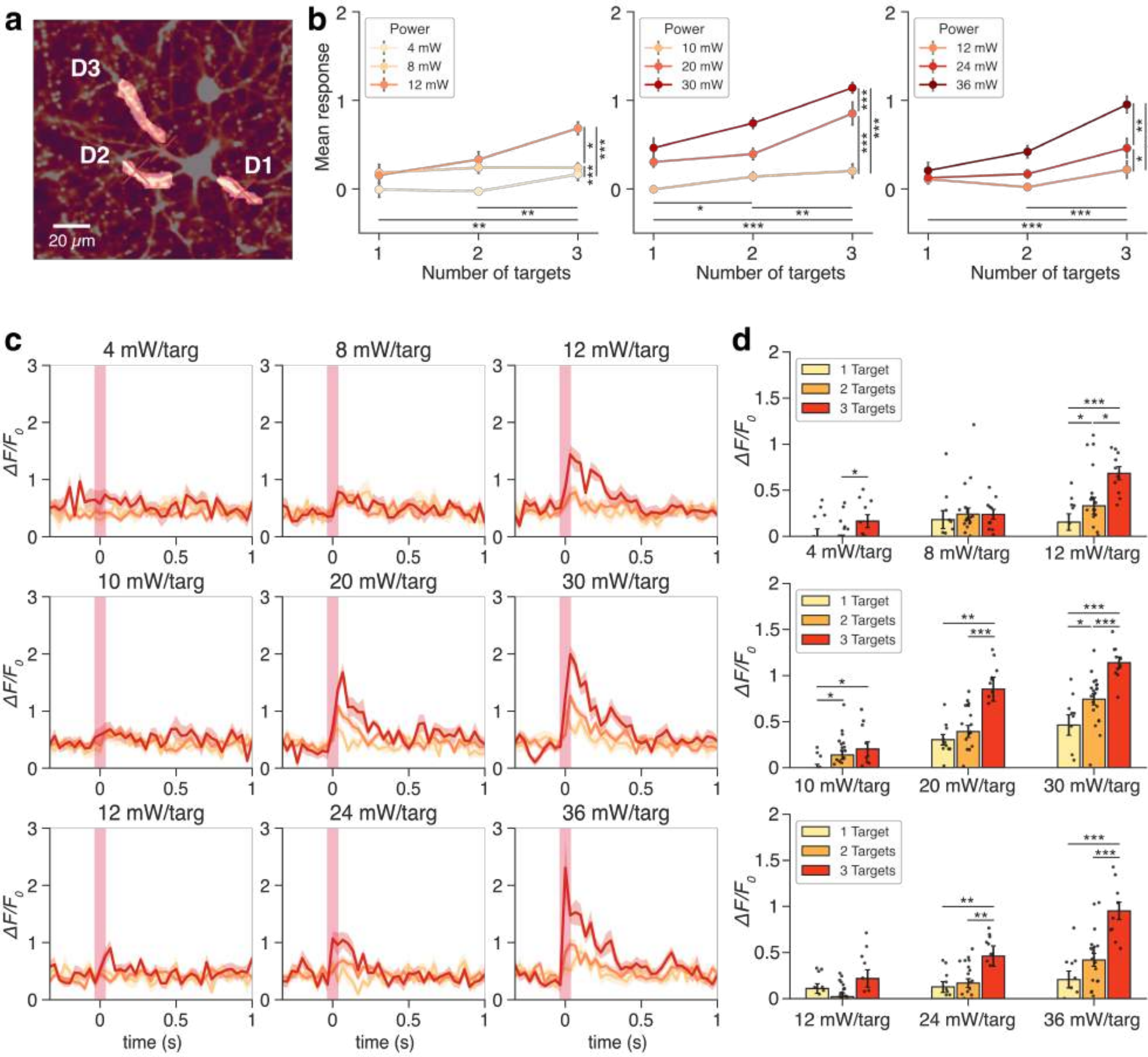

Supplementary Figure 6. Multi-target photostimulation responses, D2.

a) L2/3 neuron in visual cortex, with labeled dendritic targets for multi-target photostimulation. Before each experiment, three dendritic targets were identified on a neuron expressing GCaMP8s and ChRmine. In each block, one of three powers was sampled (lower left) and one of seven combinations targeting 1, 2, or 3 dendrites simultaneously (center) were randomly executed via a 10 ms photostimulation pulse, followed by a 4 s delay (see **Fig. 8a**).

b) ChRmine-activated response of a single dendritic ROI (D2) at increasing powers and target numbers, disaggregated by blocks. (* $p < 0.05$, ** $p < 0.01$, *** $p < 0.001$)

c) Photostimulation-triggered averages for D2 at increasing powers and numbers of targets.

d) Quantification of mean responses of D2 by power and number of targets.

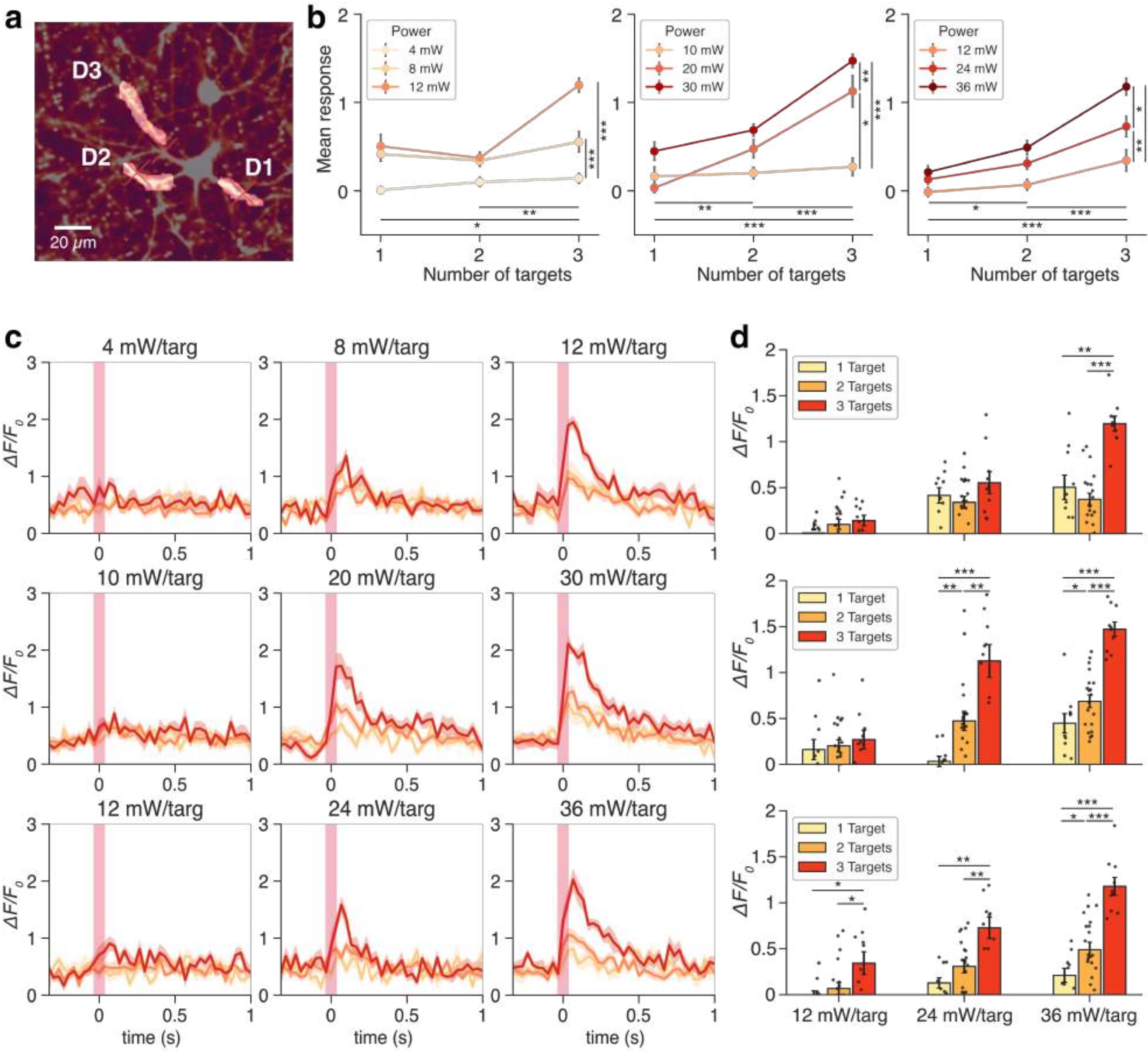

Supplementary Figure 7. Multi-target photostimulation responses, D3.

a) L2/3 neuron in visual cortex, with labeled dendritic targets for multi-target photostimulation. Before each experiment, three dendritic targets were identified on a neuron expressing GCaMP8s and ChRmine. In each block, one of three powers was sampled (lower left) and one of seven combinations targeting 1, 2, or 3 dendrites simultaneously (center) were randomly executed via a 10 ms photostimulation pulse, followed by a 4 s delay (see **Fig. 8a**).

b) ChRmine-activated response of a single dendritic ROI (D3) at increasing powers and target numbers, disaggregated by blocks. (* $p < 0.05$, ** $p < 0.01$, *** $p < 0.001$)

c) Photostimulation-triggered averages for D3 at increasing powers and numbers of targets.

d) Quantification of mean responses of D3 by power and number of targets.

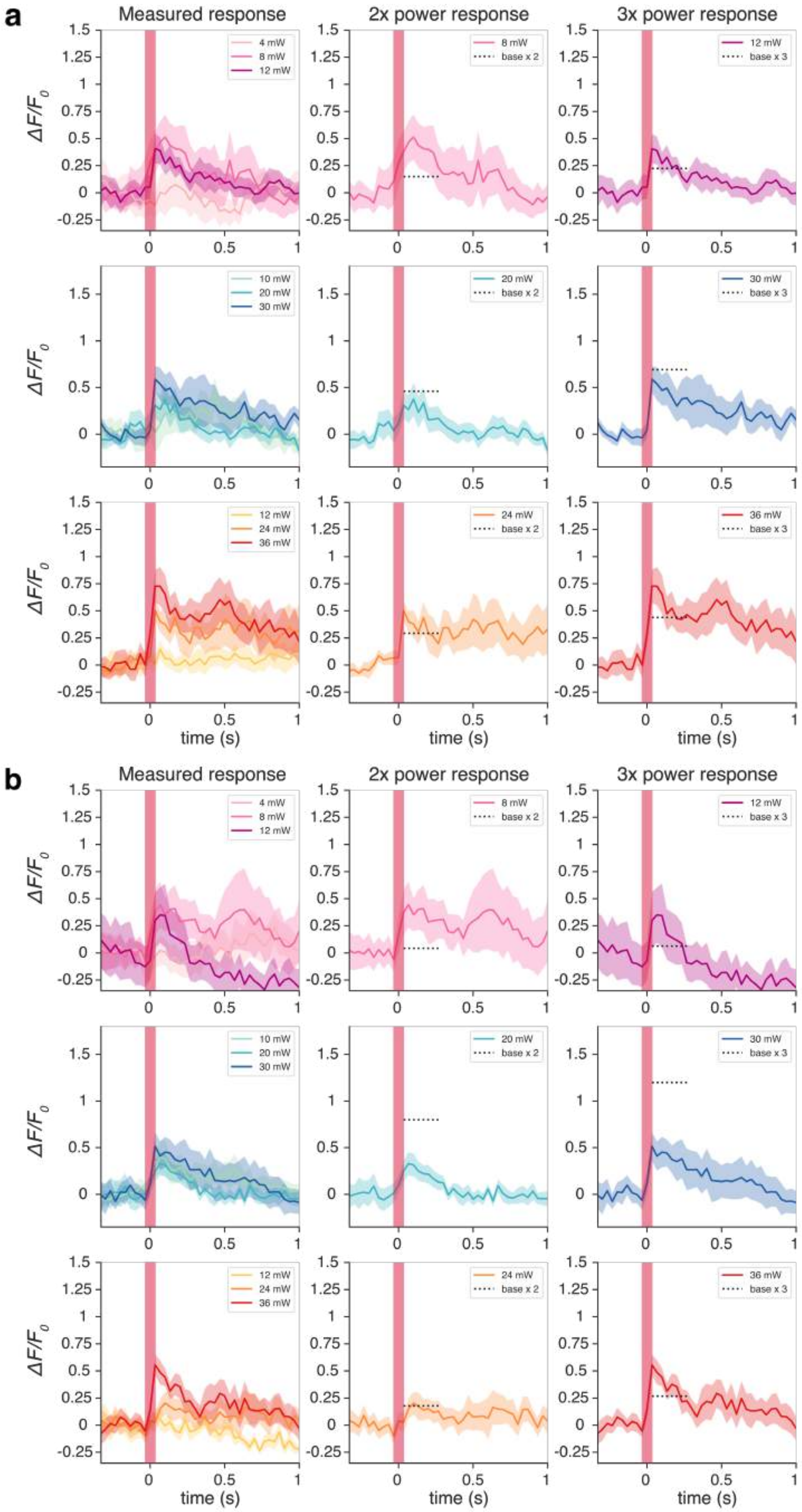

Supplementary Figure 8. Power-scaled dendritic photostimulation, D1 and D3.
a-b) Somatic traces of theoretical and measured somatic activation by D1 (a) or D3 (b) stimulation at doubled (center) or tripled powers (right). Rows denote experimental blocks: Row 1, 4-12 mW. Row 2, 10-30 mW. Row 3, 12-36 mW (n = 10 trials/power, 1 neuron). For experimental setup, see **Figure 11a**.

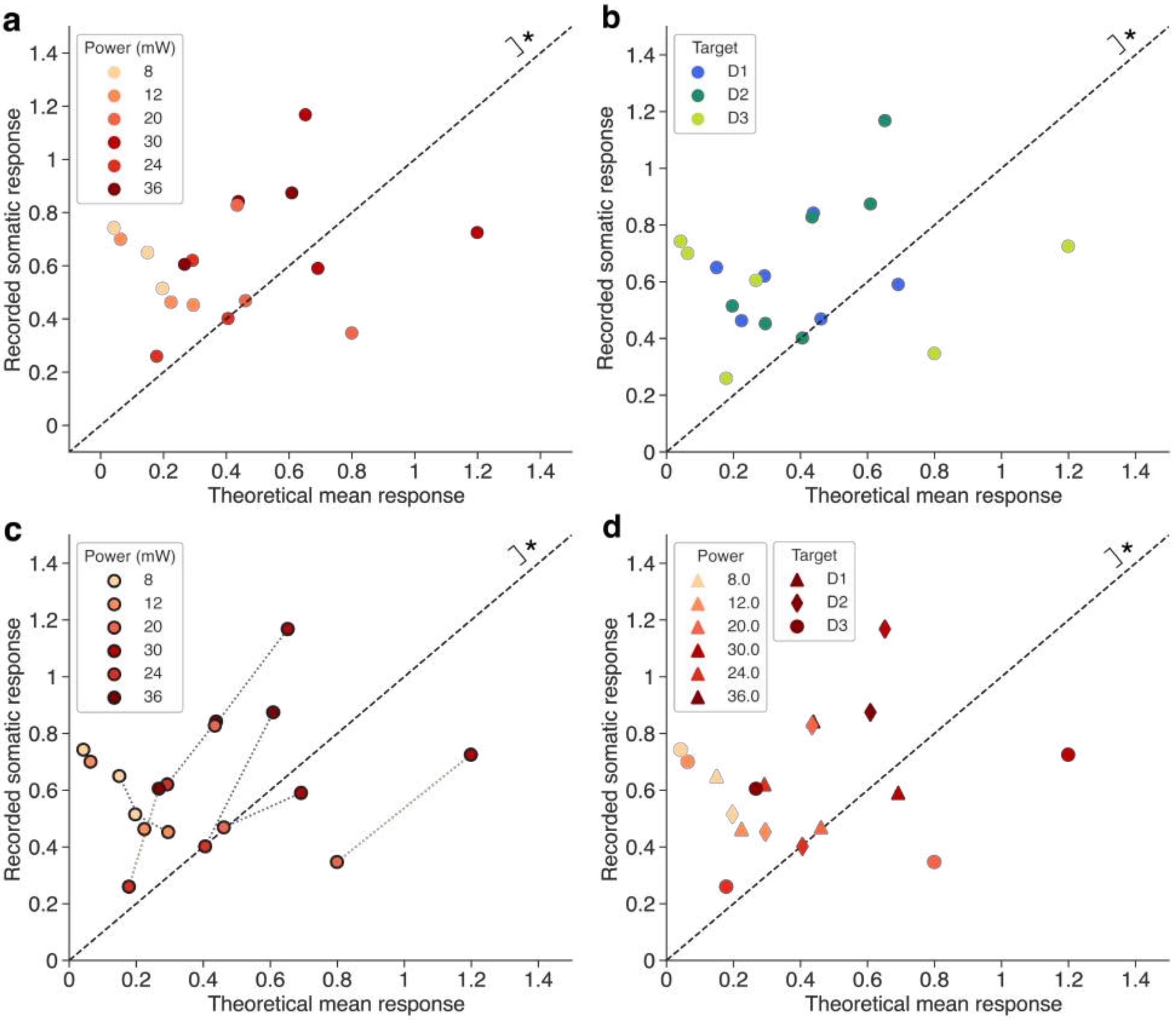

Supplementary Figure 9. Power-scaled dendritic photostimulation, summary plots.
a-b) Theoretical versus empirical photostimulation-evoked somatic responses from the experiment described in **Figure 11a**, labeled by power (a) and stimulated dendrite (b) (n = 3 dendrites, 1 neuron, 1 mouse; p = 0.0182, Wilcoxon signed-rank test).
c) Theoretical versus measured somatic responses, colored by power directed to stimulated dendrite. Dotted lines connect trial pairs; color of dotted lines indicates stimulated dendrite from (b).
d) Theoretical versus empirical photostimulation-evoked somatic responses, labeled by power (marker color) and dendritic target (marker shape).

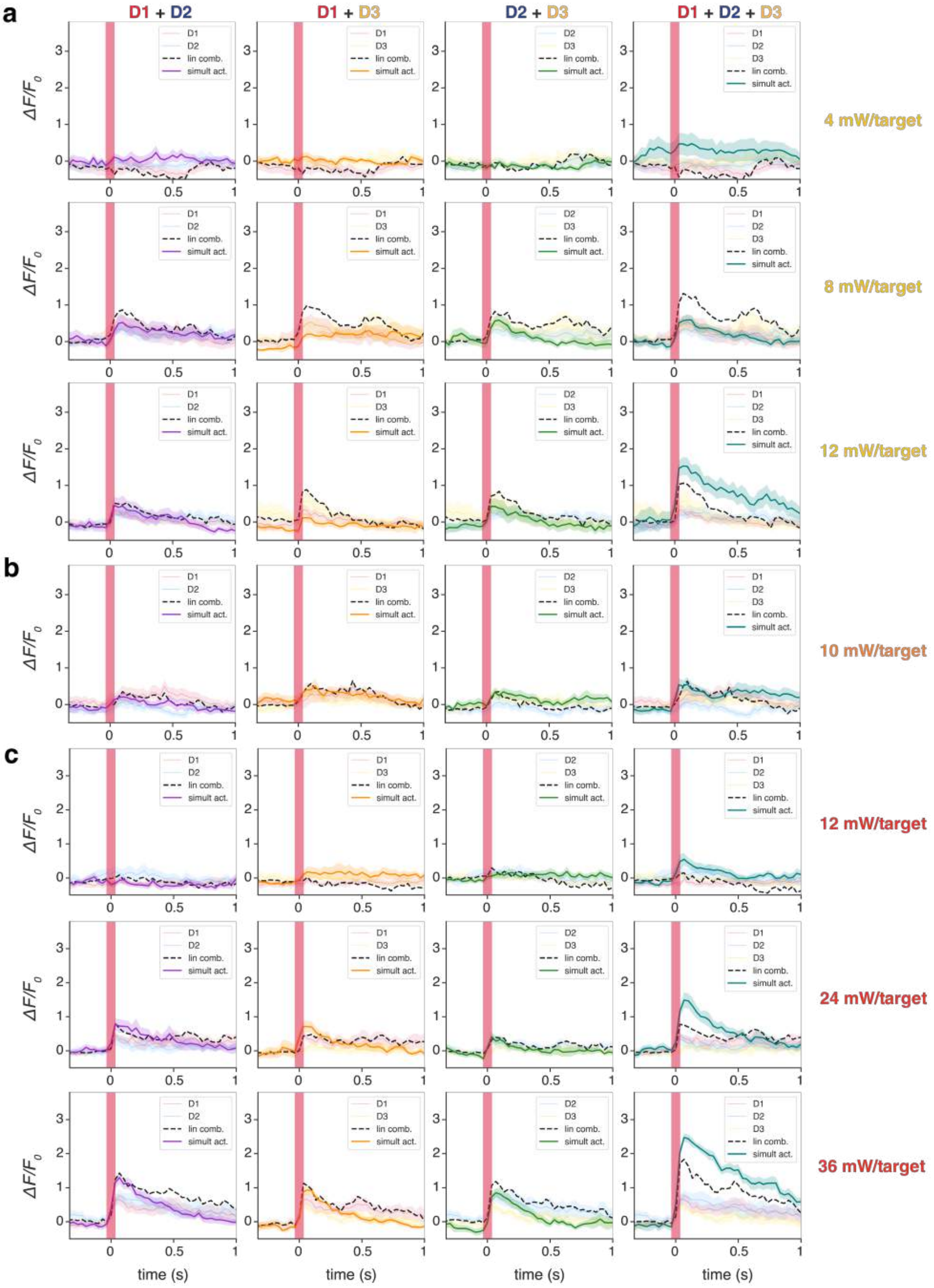

Supplementary Figure 10. Inter-dendritic summation, other powers.
a-c) Theoretical (dotted lines) and experimentally recorded somatic $\Delta F/F_0$ traces for each combination of two or three dendrites (see **Fig. 12a** for experimental setup). Rows denote power delivered to each individual target (a, Block 1; b, Block 2; c, Block 3). Lin comb., linear combination. simult act., simultaneous activation.